TURUN
YLIOPISTO
UNIVERSITY
OF TURKU

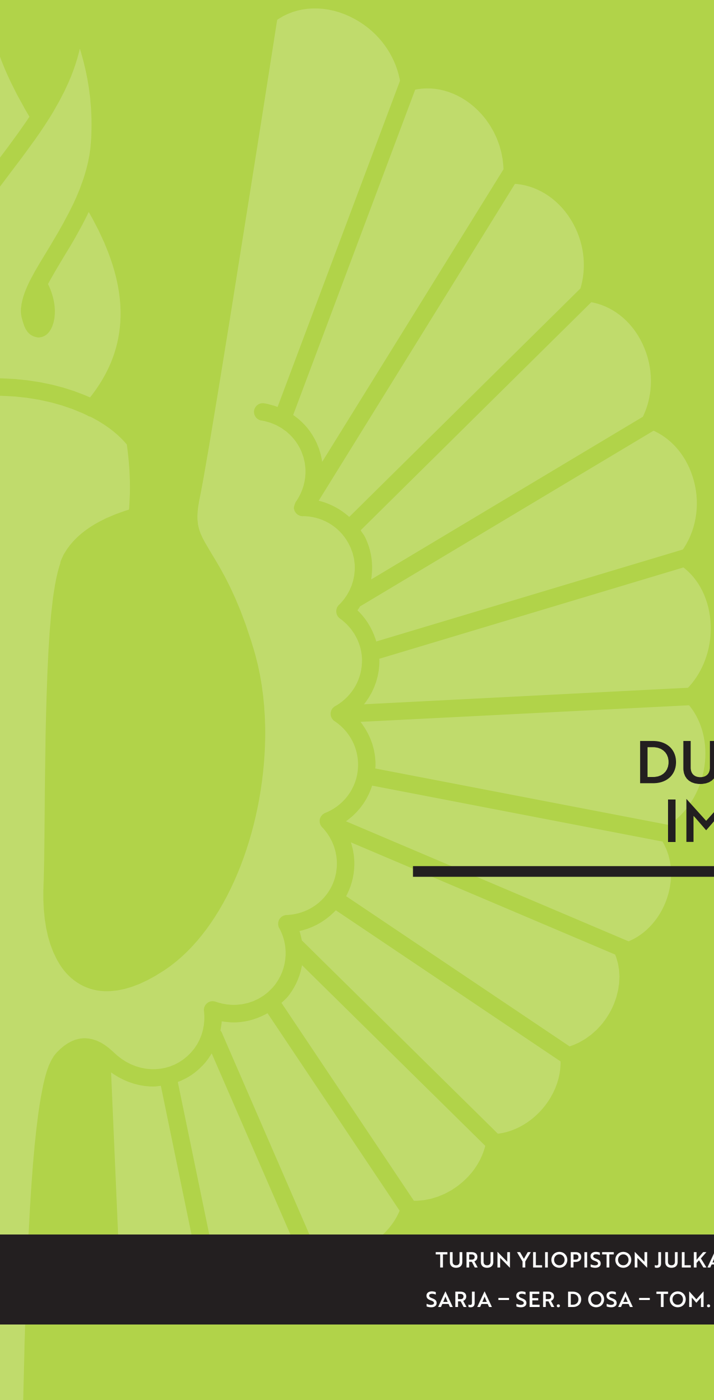

DUAL GATED PET/CT IMAGING OF HEART

Tommi Kokki

TURUN YLIOPISTON JULKAISUJA – ANNALES UNIVERSITATIS TURKUENSIS
SARJA – SER. D OSA – TOM. 1586 | MEDICA – ODONTOLOGICA | TURKU 2021

TURUN
YLIOPISTO
UNIVERSITY
OF TURKU

DUAL GATED PET/CT IMAGING OF HEART

Tommi Kokki

TURUN YLIOPISTON JULKAISUJA – ANNALES UNIVERSITATIS TURKUENSIS
SARJA – SER. D OSA – TOM. 1586 | MEDICA – ODONTOLOGICA | TURKU 2021

University of Turku

Faculty of Medicine
Clinical Physiology and Nuclear Medicine
Doctoral Programme in Clinical Research

Supervised by

Professor, Juhani Knuuti
Turku PET Centre, University of Turku
and Turku University Hospital
Turku, Finland

Professor, Mika Teräs
Medical Physics
University of Turku
Turku, Finland

Reviewed by

Adjunct professor, Antti Sohlberg
Päijät-Häme Central Hospital
Lahti, Finland

Adjunct professor, Mikko Hakulinen
Kuopio University Hospital
Kuopio, Finland

Opponent

Adjunct professor, Kirsi L. Timonen
Central Finland Health Care District
Hospital Nova of Central Finland
Jyväskylä, Finland

ISBN 978-951-29-8628-6 (PRINT)
ISBN 978-951-29-8629-3 (PDF)
ISSN 0355-9483 (Print)
ISSN 2343-3213 (Online)
Painosalama, Turku, Finland 2021

Chasing Cars, Snow Patrol

We'll do it all
Everything
On our own

I don't quite know
How to say
How I feel

I need your grace
To remind me
To find my own

Forget what we're told
Before we get too old
Show me a garden that's bursting into life

To Laura

UNIVERSITY OF TURKU
Faculty of Medicine
Clinical Physiology and Nuclear Medicine
TOMMI KOKKI: Dual Gated PET/CT Imaging of Heart
Doctoral Dissertation, 183 pp.
Doctoral Programme in Clinical Research
September 2021

ABSTRACT

Coronary artery disease (CAD) resulting from atherosclerotic arterial changes, plaques, is a progressive process, which can be asymptomatic for many years. Asymptomatic CAD can cause a heart attack that leads to sudden death if the vulnerable coronary plaque ruptures and causes artery occlusion. The plaque inflammation plays an important role in the rupture susceptibility. Reliable anticipation of rupture is still clinically impossible for a single patient. Detection of the vulnerable coronary plaques before clinical signs remains a significant scientific challenge where positron emission tomography (PET) can play an important role.

The aim of this dissertation was to find out whether a small, coronary plaque size, heart structures could be detected by a clinically available positron emission tomography and computed tomography (PET/CT) hybrid camera in realistically moving cardiac phantoms, a minipig model, and patients with CAD. Due to cardiac motions accurate detection of small heart structures are known to be problematic in PET imaging. Due to absence of commercial application at the beginning of the study, new dual gating method for cardiac PET imaging was developed and programmed that takes into account both contraction and respiratory induced cardiac motions.

Cardiac phantom PET studies showed that small, active and moving plaques can be distinguished from myocardium activity and the gating methods improved the detection sensitivity and resolution of the plaques. In minipig and CAD patient cardiac PET studies small structures of myocardium and coronary arteries was detected more sensitive and accurately when using dual gating method than manufacturer gating methods. In cardiac patient PET study respiratory induced cardiac motions were shown to be linearly dependent with spirometry-measured respiratory volumes. Standard 3-lead electrocardiogram (ECG) measurement can be filtered by anesthesia monitor to detect lung impedance signal. In cardiac patient PET study this lung impedance signal were applied for respiratory gating. In this study was observed that the 3-lead ECG derived impedance signal gating method detects respiratory induced cardiac motion in PET as well as other externally used respiratory gating methods.

In summary, the dual gated cardiac PET method is more sensitive and accurate to detect small cardiac structures, as coronary vessel wall pathology, than the commercial methods used in the study.

KEYWORDS: Cardiac PET, respiratory gating, cardiac gating, coronary plaque

TURUN YLIOPISTO
Lääketieteellinen tiedekunta
Kliininen fysiologia ja isotooppilääketiede
TOMMI KOKKI: Sydämen kaksoisliiketahdistettu PET/CT kuvantaminen
Väitöskirja, 183 s.
Turun kliininen tohtoriohjelma
Syyskuu 2021

TIIVISTELMÄ

Ateroskleroottisten valtimomuutosten, plakkien, seurauksena asteittain kehittyvä sepelvaltimotauti voi olla vuosia oireeton. Oireeton sepelvaltimotauti voi aiheuttaa äkkikuolemaan johtavan sydäninfarktin, mikäli sepelvaltimon seinämäplakin repeytymisestä aiheutuu verisuonen tukkiva hyytymä. Tutkimuksissa on osoitettu, että plakin tulehduksella on merkittävä rooli repeytymisalttiudelle. Repeytymisen luotettava ennakointi on yksittäisen potilaan kohdalla edelleen kliinisesti mahdotonta. Tulehtuneiden ja repeytymisalttiiden sepelvaltimoplakkien toteaminen ennen kliinisiä oireita on edelleen merkittävä tieteellinen haaste, missä positroniemissiotomografia (PET) kuvantamisella voi olla merkittävä rooli.

Väitöskirjan tavoitteena oli selvittää, voidaanko kliinisessä käytössä olevalla positroniemissiotomografia ja tietokonetomografia (PET/TT) yhdistelmäkameralla havaita pieniä, sepelvaltimoplakkien kokoisia, sydämen rakenteita koneellisesti toimivissa todenmukaisissa sydänmalleissa, eläinmallissa ja sepelvaltimotautia sairastavilla potilailla. Sydämen pienten rakenteiden tarkka havaitseminen PET/TT-kameroilla on haasteellista sydämen liikkumisen vuoksi. Tutkimuksessa kehitettiin ja ohjelmoitiin uusi sydämen PET-kuvantamisen liiketahdistusmenetelmä, joka ottaa huomioon sekä sydämen supistusliikkeen että hengitysliikkeen vaikutuksen sydämen PET kuvantamissa.

Koneellisilla sydänmalleilla osoitettiin, että PET on riittävän herkkä havaitsemaan pieniä ja liikkuvia radioaktiivisia ”sepelvaltimoplakkeja”, ja että liiketahdistusmenetelmät parantavat plakkien havaitsemisherkkyyttä ja tarkkuutta. Eläinmallissa ja sepelvaltimotautipotilailla kaksoisliiketahdistusmenetelmän herkkyys ja tarkkuus havaita pieniä sydänlihaksen ja sepelvaltimoiden rakenteita todettiin kaupallisia tahdistusmenetelmiä paremmaksi. Potilastutkimuksissa todettiin hengityksen aiheuttama sydämen liike PET-kuvissa lineaarisesti riippuvaiseksi spirometrialla mitattujen hengitystilavuuksien kanssa. Tavallisesta 3-johtoisesta sydänsähkökäyrästä voidaan anestesiamonitorin avulla suodattaa keuhkojen impedanssisignaalia. Hengitysliikkeen aiheuttama potilaiden sydämen liike PET-kuvissa havaittiin yhtä hyvin käyttämällä tätä keuhkojen impedanssisignaalia kuin muita yleisesti käytettäviä ulkoisia hengitystahdistussignaaleja.

Todetaan, että kaksoisliiketahdistettu sydämen PET-kuvantamismenetelmä on tutkimuksessa käytettyjä kaupallisia menetelmiä herkempi ja tarkempi havaitsemaan sydämen pieniä rakenteita sekä sepelvaltimon seinämän tulehdusplakkeja.

AVAINSANAT: Sydämen PET, sydämen kaksoisliiketahdistus, sepelvaltimoplakki

Table of Contents

Abbreviations

18F-FDG	[18F]Fluoro-2-deoxy-2-D-glucose
18F-NaF	[18F]Sodium-fluoride
AC	Attenuation correction
ACS	Acute coronary syndrome
BGO	Bishmuth Germanate Oxide
BSO	Bishmuth Silicon Oxide
BH	Breath-hold
b-FFE	balanced fast field echo
CAD	Coronary artery disease
CC	Correlation coefficient
CMA	Center of myocardium 18F-FDG activity
CMR	Cardiac magnetic resonance
CNR	Contrast to noise ratio
CT	Computed tomography
CTA	Computed tomography angiography
CTAC	Computed tomography attenuation correction
DG	Dual gating
ECG	Electrocardiogram
FBP	Filtered backprojection
FOV	Field of view
FWHM	Full-width half maximum
GPM	Gross patient motion
HU	Houndsfield unit
LAD	Left anterior descenting artery
LCX	Left circumflex artery
LCA	Left coronary artery
LM	List mode
LOR	Line of Response
LSO	Lutetium Oxyorthosilicate
LYSO	Lutetium-Yttrium Oxyorthosilicate
MRI	Magnetic resonance imaging

NEMA	National Electrical Manufacturers Association
OSEM	Ordered subset expectation maximization
PET	Positron emission tomography
PMT	Photomultiplier tube
PSF	Point-spread function
PVC	Partial volume correction
PVE	Partial volume effect
RC	Recovery coefficient
RC%	Percent recovery coefficient
RCA	Right coronary artery
RDF	Raw data file
RF	Radiofrequency
ROI	Region of interest
RPM	Real-Time Position Management
SC	Sinus coronary
SD	Standard deviation
SiPM	Silicon digital photomultiplier
SNR	Signal to noise ratio
SUV	Standardized uptake value
TBR	Target to background ratio
TE	Time of echo
ToF	Time-of-Flight
TR	Time of repetition
VHFLCPP	Very high-fat, low-carbohydrate, protein-permitted
VOI	Volume of interest

List of Original Publications

This dissertation is based on the following original publications, which are referred to in the text by their Roman numerals:

I **Kokki T**, Sipilä HT, Teräs M, Noponen T, Durand-Schaefer N, Klén R, Knuuti J. Dual gated PET/CT imaging of small targets of the heart: method description and testing with a dynamic heart phantom. J Nucl Cardiol. 2010 Jan-Feb; 17(1):71–84.

II **Teräs M, Kokki T**, Durand-Schaefer N, Noponen T, Pietilä M, Kiss J, Hoppela E, Sipilä HT, Knuuti J. Dual gated cardiac PET-clinical feasibility study. Eur J Nucl Med Mol Imaging. 2010 Mar; 37(3):505–16.

III **Kokki T**, Klén R, Noponen T, Pärkkä J, Saunavaara V, Hoppela E, Teräs M, Knuuti J. Linear relation between spirometric volume and the motion of cardiac structures: MRI and clinical PET study. J Nucl Cardiol 2016 Jun; 23(3):475–85.

IV **Kokki T**, Noponen T, Klén R, Teräs M, Knuuti J. Thoracic impedance based respiratory gating method for detection of cardiac motion in PET using standard 3-lead ECG configuration. Manuscript for publication.

The original publications have been reproduced with the permission of the copyright holders.

1 Introduction

Atherosclerosis is a slowly evolving vascular inflammatory disease and is characterized by accumulation of lipids into arterial wall and progression of lesions, also called plaques. Atherosclerosis is the primary cause of coronary artery disease (CAD) and the coronary plaque rupture is considered an important determinant of the outcome of CAD. Identifying vulnerable coronary plaques that are prone to rupture are thus a great clinical interest.

Electrocardiogram (ECG), blood tests, exercise testing and cardiac imaging are used to confirm the diagnosis of CAD, to document ischaemia in patients with stable symptoms, to risk stratify patients with stable angina and acute coronary syndrome (ACS). In elective cases, the pre-test likelihood of CAD is calculated based on symptoms, sex and risk factors derived from epidemiological studies as Framingham (Anderson et al., 1991) and PROCAM (Assmann et al., 2002). This traditional risk assessment of CAD has been shown to predict long-term outcome in large populations. To provide better clinical route to identify, treat, and prevent near future victims of ACS it is proposed to focus on "cardiovascular vulnerable patient", meaning the characterisation of the vulnerable plaque, vulnerable blood and the vulnerable myocardium (Naghavi et al., 2003a, 2003b).

Imaging tools are needed for the plaque characterisation. In invasive angiography is often possible to identify the culprit, thrombotic lesion after ACS (Wijns et al., 2010). Angiography together with intravascular ultrasound (IVUS) (Rioufol et al., 2004) or optical coherence tomography (OCT) (Brezinski et al., 1996) makes it possible to get more detailed information of the nature of coronary plaques. However these methods are invasive and there are complication risks, and thus are not well suited to risk assessment. Magnetic resonance imaging (MRI) and multidetector computed tomography (MDCT) are suitable methods for non-invasive coronary angiography to detect atherosclerotic coronary plaques but these methods are insensitive to identify the vulnerable plaques from the stable plaques.

Positron emission tomography (PET) has potential to target metabolism, inflammation, apoptosis, angiogenesis and extracellular matrix degradation which all are related to vulnerable plaque formation and rupture (Naghavi et al., 2003a). With histopatologic examination it has been identified that inside the vulnerable plaque the concentration of active macrophages has increased (Narula et al., 2008). Clinically widely available glucose analogue, [18F]Fluoro-2-deoxy-2-D-glucose (18F-FDG), is promising radiotracer for vulnerable plaque PET imaging, because 18F-FDG is taken up by active macrophages in vulnerable plaques (Rudd et al., 2002; Tawakol et al., 2005). However, the small size of the plaques and the constant motion of heart makes the vulnerable coronary plaque imaging challenging. Dimensions of vulnerable coronary plaque are reported to be on average a few millimeters (Narula et al., 2008; Strauss & Narula, 2007). The motion of heart due to respiration and cardiac contraction are reported to be around 10 mm for both distortions. As the spatial resolution of PET imaging is around 5 to 6 mm (Germano et al., 2016; Teräs et al., 2007) for non-moving organs, the both of the motion distortions needs to be taken into account when sub-voxel size targets as vulnerable coronary plaques are imaged with PET. Currently, cardiac PET data can be routinely acquired in either cardiac (Freiberg et al., 2004) or in respiratory gated (Dawood et al., 2007) mode where the gating can improve the detected spatial resolution of moving targets. This study proposes a self-reconstructed dual gated cardiac PET method, that takes into account both contraction and respiration motions at the same time, and evaluates the method’s capability to detect small realistically moving cardiac structures, as vulnerable coronary plaques, with clinically available PET/CT device.

2 Review of the Literature

2.1 PET imaging

PET is a functional imaging modality that provides dynamic or steady state information from administered radioactive tracer distribution inside the body. Distribution of the tracer is determined by physiologic and metabolic interactions between tracer and tissues. Each radioactive tracer is a production of radiopharmaceutical chemistry and is usually a molecular size compound that is labelled with unstable radionuclide that has relative short half-life. The idea of PET imaging is that radioactive tracers maintain similar structure and interaction properties than unlabelled molecules with known biological properties. Thus physiological and metabolic interactions of the tracers give information of the behaviour of the biochemical process of interest such as glucose metabolism in case of fluorine labelled 18F-FDG. Radionuclides that are used in nuclear medicine are productions of cyclotrons, nuclear reactors, or radionuclide generators. In addition to this, radionuclide production and tracer labelling requires a high-level local radiopharmaceutical chemistry laboratory near by the nuclear imaging center, in which the chemical stability and purity of tracer are guaranteed.

2.1.1 Radioactive decay and annihilation process

Radionuclides that undergo positron emission decay are mostly produced in cyclotrons. In positron emission decay a proton in the nucleus of the atom is converted into a neutron and simultaneously emitted a positron and neutrino. The emitted positron has very short lifetime in a tissue and when the most of the positron's kinetic energy is dissipated it will form a positronium state with a nearby electron that is in rest. The positronium undergo annihilation process under one nanosecond where the mass of the positron and the electron is converted into electromagnetic energy according to Einstein's mass-energy equivalence. Due to law of conservation of the total momentum the annihilation process has to produce at least two photons that are emitted simultaneuosly. These two photons are emitted in almost opposite, 180 degree apart, directions with almost equal kinetic energy of 511 keV to satisfy the conversation laws. High-energy 511 keV photons interact with tissue as well as with scintillator materials through photoelectric effect or Compton scattering. The 511 keV photons interact mainly due to Compton scattering in tissue and small-angle forward scatter is most likely to be happened.

In PET imaging the purpose is to detect and localize two simultaneously emitted and opposite propagating 511 keV photons that are products of annihilation process using opposite positioning detector pairs. This phenomena is called a coincidence event. Due to the nature of annihilation process the position of annihilation process can be localized only if the both annihilation photons can be detected and localized. Then the line between the locations of the detected photons has to pass through the point of annihilation process and is referred as electronic collimation or Line of Response (LOR) (Figure 1).

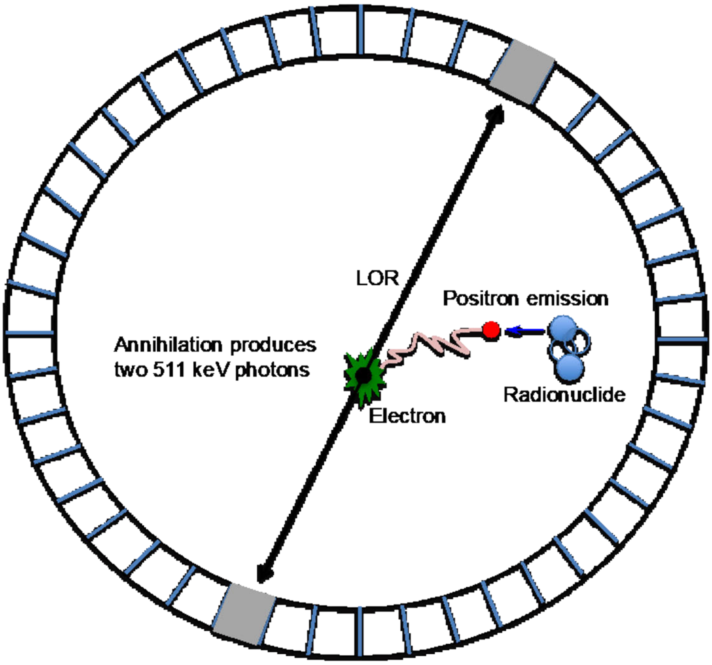

Figure 1. Positron emission, annihilation and coincidence event detection. LOR = Line of Response.

2.1.2 PET scanner hardware configuration

In PET imaging hardware configuration consists of pairs of scintillation detectors with associated electronics, as amplifiers and pulse height analyzers, and a coincidence circuit. Most of PET scanners consist of a large number of block detectors placed in adjacent stacked ring geometry. In conventional block detector design the scintillator material is segmented into an array of smaller detector elements, which are coupled to few single-channel photon multiplier tubes (PMTs) to which the scintillation light is shared (Figure 2). In this block design 511 keV photon interaction in each scintillator array element produces a unique distribution of scintillation light between the coupled PMTs leading to unique signals on these PMTs. According to the unique electrical current signals between the coupled PMTs the position of interaction within the block of scintillator array elements can be calculated for each 511 keV photon. Block design with smaller detector elements than PMTs leads also to better spatial resolution of 511 keV photon interaction with detector. Thus the spatial resolution is strongly related to the width of the detector elements that are commonly around 4 mm in current generation block detectors in clinical PET scanners (Germano et al., 2016).

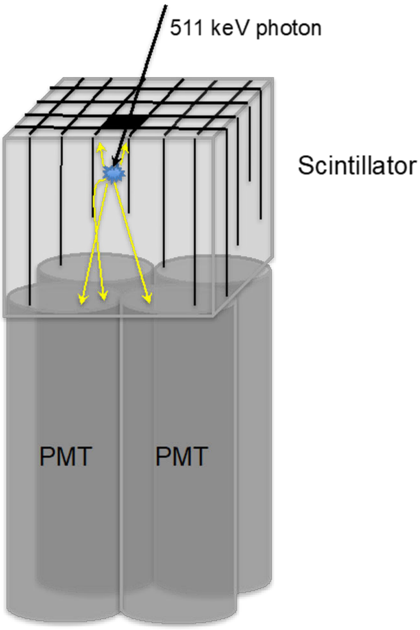

Figure 2. PET block detector design. PMT = photomultiplier tube.

In recent PET design large analogic PMTs are replaced by small silicon digital photomultipliers (SiPMs). In this design 1-to-1 correspondence between photomultipliers and detectors is applied. SiPM have shorter time resolution than analogic PMT design, and thus SiPM detectors gain more benefit if Time-of-Flight (ToF) acquisition is applied. SiPM detector design together with ToF-image acquisition allows simultaneous improvements in sensitivity, image resolution and maximum count rate when compared to traditional PET detector design (Germano et al., 2016).

2.1.3 PET event detection

Time and energy resolution of detectors determines accuracy that a coincidence event can be detected. The coincidence time window is time period that ensures that annihilation photon pair is not accidentally rejected. For the current PET scanners that have scintillation materials as Lutetium Oxyorthosilicate (LSO) and Lutetium-Yttrium Oxyorthosilicate (LYSO) coincidence time windows are from 4.1 to 4.9 nanoseconds (Germano et al., 2016). Coincidence time window together with dead time of detectors impose limitations to sensitivity of the scanner and upper limit for injected doses. The ability of the detector to determine the energy of the photon is known as the energy resolution. Energy resolution is scintillator dependent and for LYSO crystals common energy window is between 425 keV to 650 keV (Teräs et al., 2007). This means that only low energy and large angle scatter events are efficiently rejected due to energy windowing if common 3D acquisition mode is used. Annihilation photons that are detected within a coincidence time and energy windows of the detector pair are accepted as a true coincidence event.

Total number of events detected by the PET scanner coincidence circuit is referred to as prompt coincidences. Due to limitations of detectors and electrical design of PET scanner detected coincidences contains undesired events such as random, scattered and multiple coincidences that degrade the distribution of true radioactivity concentration and thus needs to be corrected (Figure 3). Because the detectors have finite time resolution the events that happen inside certain predefined timing window are accepted for coincidence event. The scattered and random coincidences need to be corrected by subtracting them from the prompts to yield the net true coincidence rate for each measured LOR. Single events form the basis for random and multiple coincidence events. Also single events need to be processed by the electronics and this processing time is primary reason for degrading true coincidence detection sensitivity when high radioactive doses are used. This is due to dead time of the detectors. Dead time is defined as the time period when detector cannot record other events. Decay time constant for LSO and Bishmuth Germanate Oxide (BGO) -crystals are 40 ns and 300 ns, respectively (Germano et al., 2016). Dead time is typically 3 to 4 times the decay time constant.

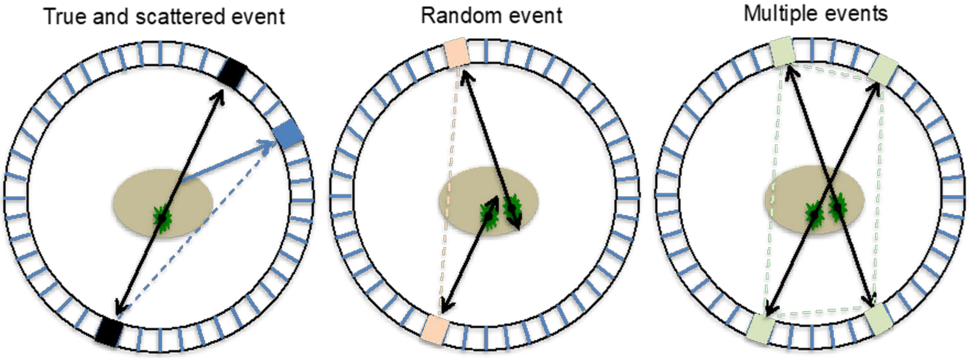

Figure 3. Coincidence event types in PET imaging.

2.1.4 PET data structure

Coincidence events that satisfy both energy and time window resolution are written in raw data file by sorting hardware. In list mode (LM) acquisition each coincidence event is individually written to a file with information of the two detectors and time at which the event was detected. In addition if ECG and/or respiratory signals are simultaneously acquired the synchronization information between the emission data and the signals can be stored in the LM data structure as separate time event. In modern advanced PET scanners, that have ability for ToF imaging mode (Germano et al., 2016), also time difference between detection times of coincidence photon pair is included in the LM file. As LM data contains time information of each event the data can be post-processed and sorted into time bins after the study that is beneficial in dynamic or gated PET studies. In gated PET studies arbitrary retrospective definition of gating parameters are commonly derived from the additionally acquired gating signals as ECG. In addition, LM acquisition is especially important for hybrid PET/CT imaging with spatial and temporal realignment of the PET emission data with the CT data (Klaus P Schäfers & Stegger, 2008). Another, more robust and efficient way, to store the data is a histogram mode where a memory location is assigned to each possible LOR so that each time when coincidence event is detected that LORs memory location is increased by 1. However, in histogram mode events are integrated over a predefined acquisition time that rule out the possibility to post-process the acquired data. The acquired raw PET data that contains the coincidence events are histogrammed in a 2D matrix that is referred as a sinogram where each element in the matrix represents the number of events detected by a particular pair of detectors along a specific LOR.

2.1.5 PET data corrections

Due to nature of interaction of annihilation photons, PET scanner design and geometry a number of corrections are applied as a series of multiplicative factors to the acquired raw sinogram data before image reconstruction. The volumetric correction, called normalization, is applied to correct each individual LOR using a multiplication factor that compensates nonuniformities in PET scanner design and geometry. Scatter and attenuation are basically one and the same phenomenon. First is applied scatter correction and then attenuation correction (AC). AC factors for the LORs joining the detector pairs are independent of the location of the activity source and depends only the total thickness and attenuation coefficients of the object along the LOR. Principle for computed tomography attenuation correction (CTAC) is that first CT scan is resampled to the same size as the PET data, then CT data is suitably blurred, and finally scaled so as to convert the pixel values from Hounsfield units (HU) to the attenuation coefficients, which would be obtained at 511 keV photons (Kinahan et al., 2003).

Random events result in additional false events in LORs and without correction lead to a loss in image contrast, impair quantification, and can lead to significant image artefacts. Random correction methods provide a statistically separate measurement of the number of random events detected by each detector pair that is then subtracted from the prompt coincidence measurement. This subtraction of two measurements leads to an increase in the statistical uncertainty of the true coincidence rate.

In an ideal system the true count rate of the system increases linearly with increasing activity in the field of view (FOV). In real scanner true coincidence detection sensitivity depends both the activity and the material of the crystals. This phenomenon is called as dead time of the detectors. Dead time is defined as the time period when detector cannot record other events. Decay time constant for LSO and BGO-crystals are 40 ns and 300 ns, respectively (Germano et al., 2016). PET scanners dead time is ranging from 120 ns for LSO up to 1200 ns for Bishmuth Silicon Oxide (BSO) -crystals (Phelps, 2006). In dynamic studies like myocardial perfusion studies at high activity concentration dead time of the crystals may cause quantitative underestimations. At some extent dead time losses can be reduced using faster scintillators and dead time corrections.

When PET sinogram data is iteratively reconstructed the normalization, attenuation and scatter corrections are part of the statistical reconstruction algorithm. If filtered backprojection (FBP) reconstruction method is used then sinogram data has to be corrected before applying the analytic FBP reconstruction algorithm.

2.1.6 PET image spatial resolution

Spatial resolution is a minimum distance between two targets that can be distinguished from an image. In PET imaging spatial resolution is commonly given as full-width half maximum (FWHM) value (Figure 4). The FWHM is measured by determining the PET system response to a point or line source and it is position and radionuclide dependent. Spatial resolution of final PET image is a convolution of resolution response functions of positron range, photon noncolinearity, and detector resolution. Intrinsic physical limitations of spatial resolution in PET imaging are due to positron range and photon noncolinearity which both yields from annihilation process. In perspective of PET imaging, positron range is determined as a perpendicular distance from the emission site of positron to the line defined by the annihilation photons i.e LOR. Positron range is radionuclide dependent and it’s magnitude is related to kinetic energy distribution of the positron. Due to momentum conserving law in annihilation process two photons are not emitted exactly in opposite directions but with some small distribution of angles around 180 degree. This is called as noncolinearity, which is independent of radionuclide and it’s estimation is linearly dependent on a diameter of PET scanner. Both of these intrinsic limitations covers together a range of 1 to 2 millimetres and thus the ultimate limit for finale spatial resolution in PET imaging is around 2 mm with optimal detectors and small size of FOV (Panin et al., 2006).

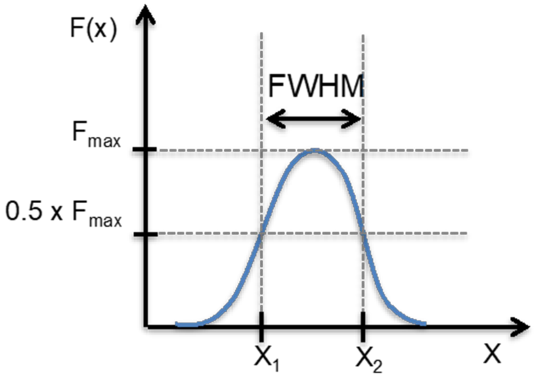

Figure 4. Function F(x) illustrates the one-dimensional response of a PET imaging system to a point source or point object. F(x) = PSF = point spread function, FWHM = Full Width at Half Maximum.

Detector resolution can be divided into geometric factors and physical factors, which depends on the detector and the scanner design. Physical component is caused by nonideal properties of the detectors such as detector scatter, light sharing and cross-talk. In a block detector the geometric resolution is dependent on the distance between the radioactive point source and detector pair. Geometric resolution is also dependent the width of the detector element. Spatial resolutions in the conventional PMT based block detectors of clinical PET scanners are around 5 mm in axial and transaxial directions (Germano et al., 2016).

2.1.7 PET system sensitivity

Overall number of events collected in PET imaging is dictated by an amount of radioactivity injected, a fraction of the activity that specifically binds with tissues of interest, an imaging time and a sensitivity of PET system. Thus the system sensitivity is a major determinant of final image quality and is depending on the efficiency of the detectors at 511 keV, the solid angle coverage of the detectors, the location of the radioactivity with respect to the detectors, and the timing and energy windows applied to the data. Sensitivity is thus strongly dependent of the thickness of the scintillation detector and the width of used energy window.

Currently clinical PET scans are done mainly in 3D acquisition mode where all possible coincidence planes are accepted. In 3D acquisition the exact scatter and random correction methods as well as low enough death time of detectors are important due to markedly increased fraction of scattered events and higher singles event rate that can result in relatively poor image quality in the regions of large amount of activity. This can be a concern if target is close to bladder region where the most of the tracers as 18F-FDG is extracted.

2.1.8 PET image reconstruction methods

In image reconstruction mathematical algorithms of computed tomography (CT) are applied to convert acquired and adequately sampled line integrals, i.e. sinogram, into a 2D PET image. Two image reconstruction approaches are used in PET: analytical and iterative reconstruction. In PET image reconstruction historically the most commonly used analytical method has been a filtered backprojection (FBP). Disadvantage is that FBP has no option to model the degrading factors such as intercrystal scatter, noncolinearity or positron range. Furthermore, FBP cannot handle the statistical properties of the data. Instead FBP assumes noise-free data and weights all LORs equally. Due to these limitations FBP is no longer used in daily clinical PET practise.

Idea of iterative image reconstruction is to have an initial guess of radioactivity distribution of the imaged object. Then this guess is forward-projected into sinogram elements. This estimated projection data is then compared with the actual measured projection data by applying a mathematical cost-function in the process. The difference between the calculated and measured projection data is exploited to update the initial guess closer to the true radioactivity distribution according to the mathematical algorithm that used to minimize or maximize the cost-function. By repeating this iterative process the image estimate should start to converge towards the true distribution of radioactivity in the object. This means that the cost function converges towards it's minimum or maximum value during the iterative process. The major advance compared to FBP algorithm is that iterative algorithms allows to include factors as system geometry, object and septa scatter, detector characteristics, positron range and noncolinearity in the reconstruction process to improve the probability that the annihilation pair emitted at certain point in the object or image space is detected in the corresponding sinogram projection element. These factors are included in the forward projection process and they can be determined and adjusted by calculation (e.g. geometric effects), simulation (e.g. detector scatter) and using standardised phantom measurements. This means that the forward-projection function of iterative reconstruction process reflects a simulation of the entire PET imaging system and can lead to more quantitatively accurate PET images and improvements in signal to noise ratio (SNR) or spatial resolution. Iterative method can produce about two times better SNR at a given spatial resolution than FBP method that means fourfold increase in the effective sensitivity of the PET scanner allowing to use lower injected activity or shorter imaging time (Phelps, 2006). However, iterative algorithms are nonlinear that can make their behaviour quite difficult to predict.

In modern advanced PET scanners the iterative reconstruction algorithm has possibility to incorporate ToF information into the reconstruction process. ToF information is time resolution that is determined as FWHM of spread around a mean time difference of the detected events for two crystals in coincidence (Budinger, 1983). ToF resolution depends on the properties of the scintillation detector, as decay time, and coincidence electronics. ToF information focuses the probability distribution of detected coincidence annihilation event along the LOR between the opposite crystals. An advantage of ToF-PET is the sensitivity gain, i.e. increased SNR, particularly in large patients (Lois et al., 2010).

2.1.9 Quantitative PET image analysis

The idea of PET imaging is to visualize a 3D image volume where each individual voxel (i.e. volume element) represents the regional tissue radioactivity concentration. In PET it is possible to classify a lesion in terms of its metabolic rate if 18F-FDG is used (Phelps, 2006). This requires that the PET system is accurately calibrated that can be done by scanning a uniform phantom with a known activity concentration. This yields to the calibration factor that can be used to convert measured image counts into an activity concentration (Bq/ml) of the imaged target. Local activity concentration of PET image or volume is determined by drawing region of interest (ROI) or volume of interest (VOI) on the image or the volume. In a dynamic imaging ROIs or VOIs can be applied to the same region or volume on all images to generate a time activity curve that shows the radiotracer concentration in the specific part of the body over time. The acquired time activity data sets can then be applied with a compartmental model to determine biologically meaningful parameters that can reflect the behaviour of the studied disease. These dynamic models also enable to construct parametric images for disease or study of interest.

2.1.10 PET image segmentation and registration

Image segmentation is an image processing tool that classifies pixel elements into regions or classes that are homogenous with respect to one or more characteristics. In CT or MRI image segmentation is used to delineate different tissue types. In PET image segmentation is used in combination with image registration. Image registration refers to the process in which image volumes are realigned into a common anatomical coordinate space. Image registration is often used to correct patient motion between different imaging studies or modalities. Image registration is applied when functional PET images and anatomical MRI or CT images are fused together for visualisation, and when CT-image is used as CTAC for PET. Robust registration methods to fuse anatomical and PET image volumes have been developed and these rely mainly on manual or semi-automated alignment methods using rigid translation and rotations of the two image volumes within an accuracy of few millimetres. These methods has shown to correct patient motion between the imaging modalities very well but they usually ignores the target motion during the PET scan that can be significantly different than in the reference anatomical imaging at least in the cardiac and thoracic region imaging (Phelps, 2006).

2.1.11 Partial volume effect in PET system

Challenge in the ROI and VOI analysis is a quantitative determination of the activity concentration in region or volumes that are small compared with the resolution of the PET scanner. A point source of radiation in PET scanner appears in PET image as a finite-sized lumb. The maximum activity concentration of this lump is lower than actual due to limited spatial resolution of PET system. This phenomenon is known as a partial volume effect (PVE). It has been reported that when the target size is less than 3 times the FWHM of the PET system PVE can severely affect qualitative and quantitative analysis of PET images (Hoffman et al., 1979; Kessler et al., 1984; Soret et al., 2002; Soret et al., 2007). The relation between PVE and target size is nonlinear so that the smaller the target is, the greater the underestimation of the uptake value is (Jaskowiak et al., 2005; Soret et al., 2007) (Figure 5). Recovery coefficient (RC) is a measure of PVE that is determined as a fraction of measured peak activity concentration and true activity concentration of the target. RC is dependent mainly on target size and spatial image resolution (i.e. FWHM value of PSF). However, in clinical studies also the target to background ratio (TBR), reconstruction parameters, applied ROI or VOI size and motion of target has to be counted in when determining the actual RC value of the target (Soret et al., 2007).

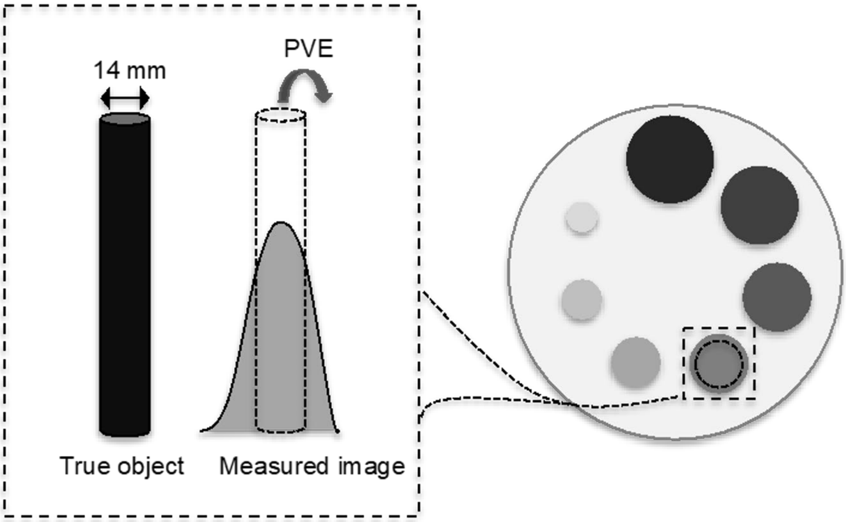

Figure 5. The same activity concentration in different size of targets have lower than actual activity concentration in PET image due to PVE. The magnitude of PVE (i.e. RC) is stronger in the smaller targets. PVE = partial volume effect, RC = recovery coefficient.

PVE refers to two distinct phenomena that make intensity values of small target in PET images lower from what they actually are. The first phenomenon is 3D image blurring that is caused by the finite spatial resolution of the PET system. Spatial resolution is determined by the detector design (i.e. mostly scintillator crystal dimensions), positron range, noncollinearity, reconstruction parameters such as number of iterations and number of subsets in iterative algorithm, and postfiltering (Soret et al., 2007). This limited spatial resolution causes activity spillover effect between a small source and it’s surroundings. Due to spillover effect the image of the small hot source is a larger but dimmer than it truly is in low activity background. PVE also depends on the shape of the target. Spheric targets are the most compact, and thus other shape of targets is more affected by PVE being more prone to spilling in and spilling out effects. Thus size, shape, and uptake of the target fully determine the spilling out effect, which is depended on spatial resolution of PET system (Boellaard et al., 2004). However, the spilling in depends on TBR, and this effect is often difficult to estimate.

The second phenomenon causing PVE is image sampling that is often called as a tissue fraction effect. In PET image the radiotracer distribution is sampled on a voxel grid, where the contours of the voxels do not match the actual contours of the tracer distribution. Most voxels therefore include different types of tissues, and thus the signal intensity in a voxel is the mean of the signal intensities of tissues in the voxel. PVE can be partly controlled through the choice of reconstruction parameters. Applying the optimal reconstruction parameters (i.e. mainly matrix size of FOV and iteration numbers) leads to the optimal spatial resolution and thus less PVE (Jaskowiak et al., 2005). However, when applying the small voxel size the tradeoff between improved spatial resolution is often to be balanced against increased noise.

Biases introduced by PVE depend also on the size of the region used to measure small target uptake (Geworski et al., 2000). When assessing clinical PET images quantitatively, standardized uptake values (SUVs) are often used to distinguish benign from malignant tumors. SUV is a measure of local concentration of tracer divided by the injected dose normalized by the body weight (Keyes, 1995). Maximum uptake value of one voxel (i.e. SUVmax) is commonly used as a measure of small tumor metabolic activity because the value is independent of the observer. In principle, maximum uptake value of target is the least affected by PVE and so SUVmax is often considered the best measure of tumor uptake. SUVmax usually provides a slight overestimation of the true maximum pixel value due to effect of noise (Soret et al., 2007). In patient studies, where background activity is always present, maximum uptake value has reported to be strongly affected by noise and therefore the reconstruction parameters, such as number of iteration, smoothing and voxel size, should be optimized and kept constant between the follow-up studies (Boellaard et al., 2004; Krak et al., 2005). Therefore in high-noise situations, maximum uptake value can behave in an unpredictable manner (Soret et al., 2007). In case of a non-homogenous uptake of small target, even without noise, a single voxel uptake value may not be representative of overall target uptake. Even if relatively large overall variability of SUVs in clinical practice has shown to be present (Lodge et al., 2012) still the SUVs have shown to provide reasonable clinical assesments of tumor response to therapy (Kinahan & Fletcher, 2010).

Methods like manually drawn VOI (Krak et al., 2005), fixed size VOI and activity threshold based VOI methods, have also been proposed to determine the size of the region to measure small target uptake value. Manually drawn VOI method is prone to observer variability. The fixed size VOI method can yield very biased results because it depends on the size of the target with respect to the size of the VOI.

However, using the size of VOI that corresponds to PET scanner spatial resolution has proposed to be most stable method relative to noise characteristics of the PET image (Geworski et al., 2000). The threshold based VOI method is objective and the resulting volume may depend on how much noise is present. However, this problem can be addressed by smoothing the image to get more reliable uptake value.

2.1.12 PET system partial volume correction methods

Recovery coefficient (RC) is a simple region-based method for partial volume correction (PVC) in PET tumor imaging down to lesions, which size are at least 1.5 times FWHM (Geworski et al., 2000; Soret et al., 2007). RC is basically a geometrical factor that is dependent only on the relationship between spatial resolution and target shape and size (Geworski et al., 2000). RC values can be precalculated as a function of a sphere size and TBR for a wide range of spatial resolution values (Hoffman, Huang, et al., 1979; Kessler et al., 1984). These RC-values are usually determined in phantom studies. Estimated metabolically active target size and shape is usually measured from co-registered CT or MR images. The PVC for the small target can then be done by dividing the measured activity of the target by the RC-factor that corresponds to the size and shape of the target.

One method for compensating the activity spillover effect is to enhance spatial resolution by modeling the detector response function (i.e. point spread function, PSF) into the iterative reconstruction process (Alessio et al., 2006). PSF is position dependent and can be determined through analytical derivations (Schmitt et al., 1988), Monte Carlo simulations (Alessio et al., 2006) or empirically (Frese et al., 2003). Details of these correction methods are studied and recently implemented in the new generation PET scanners but these technical features are too demanding to go through in this concept.

It has been reported that for current PET scanner resolution (around 5 mm) the spheric target with 5 mm diameter has RC correction value about 20 if no background activity is present (Rousset et al., 1998; Soret et al., 2007). RC value depends not only on target volume and shape but also on image sampling. RC value may be inappropriate due to spillover effects if the tumor is close to two structures with different activity concentrations (Soret et al., 2007). Clinical studies have been shown that small tumors, which diameter is less than 2 cm, were better distinguished with RC method for PVC than without the correction (Hickeson et al., 2002). PVC methods have been shown significantly suppress spillover and recovery effects of myocardium uptake due to limited spatial resolution of PET scanners (Hove et al., 1998; Nuyts et al., 1996). In addition, motion can introduce large biases in small target uptake estimates, especially in thoracic region where misregistration between CTAC and PET data can lead significant errors to SUVmax values and size estimations of small lung lesions if a respiratory motion is not properly corrected (Erdi et al., 2004). Thus the effort expended in attempting to correct PVE must be balanced against the magnitude of the other, mainly motion related, errors (Soret et al., 2007).

2.1.13 TBR in small target PET imaging

In PET imaging common index used to differentiate benign from malignant tumors is the tumor-to-background activity ratio (Lowe et al., 1994). Soret et al have performed a comprehensive simulated thoracic phantom (Zubal et al., 1994) study to determine a TBR effect on hot and small tumors with and without AC in lung or soft tissue regions (Soret et al., 2002). Main trend that Soret et al observed in their study was that TBR was systematically greater with AC than without for lung tumors but not for soft tissue tumors. Their observation disagrees with earlier results of Bengel et al, who have reported that without AC the measured TBR was not depended on lesion localization in their patient study (F M Bengel et al., 1997). In the same article Bengel et al reported also that in their phantom study higher tumor contrast has been observed for images not corrected for attenuation. Soret et al have emphasized that their study confirmed that both SUV and TBR provides similar accuracy to differentiate malignant from benign pulmonary lesions with AC (Knight et al., 1996) but not without AC (Soret et al., 2002). Soret et al also reported that tumor diameter of 5 mm and PET scanner intrinsic spatial resolution of 4 mm TBR and SUV underestimation up to 85% was observed when true TBR was 13 (Soret et al., 2002). However, the study of Soret was a simulated data where the effects of noise, randoms, scatter, and physiological motions were not included. Strauss et al have also made estimation, what is required TBR value for detection of different size of lesions (Strauss & Narula, 2007). The lesion size larger than a resolution of PET scanner was assumed to be able to detect if a measured TBR is at least 1.5 in the PET image, which corresponds about true TBR value 3 in the target. From estimations presented by Strauss et al can be obtained that true TBR values in tissue needs to increase exponentially when the lesion size gets smaller than the spatial resolution of the scanner if the lesion is assumed to be detected.

2.2 Anatomy and dimensions of heart and coronaries

Heart consists of myocardium, valves and vessels. The normal myocardium wall thickness is from around 10 mm to over 15 mm between end-diastole and end-systole (Freiberg et al., 2004; Klein & Huesman, 2002; Porenta et al., 1995). Coronary arteries that supply myocardium usually originates from sinuses of valsalva of the aortic root. The coronary arteries mainly travel on the epicardial sulcuses of heart. There are two main coronaries, left coronary and right coronary artery. Left main coronary artery usually branches after 1 to 2 cm to left anterior descending artery (LAD) and to left circumflex artery (LCX). Inner diameter of a lumen for coronary arteries gradually narrows towards the distal parts of the arteries. Mean inner diameter for the proximal parts of the coronaries vary from 4.5 mm to 2.8 mm. Women have 9% smaller epicardial arterial diameter than men. Lumen diameter is significantly increased among men with left ventricular hypertrophy (+17%) or dilated cardiomyopathy (+12%) (Dodge et al., 1992).

2.3 Atherosclerosis and vulnerable coronary plaques

Cardiovascular disease was the second leading cause of mortality worldwide in 2013 (Bowry et al., 2015). Atherosclerosis is the primary cause of CAD. Atherosclerosis is a slowly evolving disease that starts already at early age and develops over the course of tens of years. Atherosclerosis is not only a lipid storage disease, but also vascular inflammation has a fundamental role in all stages of the disease. Atherosclerosis is characterized as a chronic inflammatory disorder that involves endothelial injury of the arteries, lipid deposition, matrix metabolism, calcification, and smooth muscle migration. Atherosclerotic plaques of arteries involve numerous cell types, including T-lymphocytes, macrophages, vascular smooth muscle cells, and endothelial cells (T. Wang et al., 2012). These numerous molecular events that lead to atherosclerosis are constantly under extensive scientific study.

There are two types of atherosclerotic plaques: stable and vulnerable. Stable atherosclerotic plaques have thick fibrous caps and calcification. Vulnerable plaques are unstable and have increased inflammatory cells and lipid infiltration with thin overlying caps (T. Wang et al., 2012). Histological findings has shown that site of tearing of ruptured plaque has been influenced by variation in the mechanical strength of cap tissue due to focal accumulation of foam cells in the intima of the coronary artery. Computer modelling has been applied to show that an eccentric pools of lipid concentrated stress on the cap of different forms of plaques, especially near the edge of the plaque (Richardson et al., 1989). Vulnerable plaques have shown to have lesser degree of calcification than ruptured ones (Virmani et al., 2006). It has also shown that calcification does not increase fibrous cap stress in typical ruptured or stable coronary plaques but accumulation of lipid pool increases stresses of plaque dramatically (Huang et al., 2001). However, extensive calcification in coronary arteries has prognostic value for having subclinical risk of CAD and this risk can be evaluated using cardiac CT imaging with coronary calcium score technique (Agatston et al., 1990).

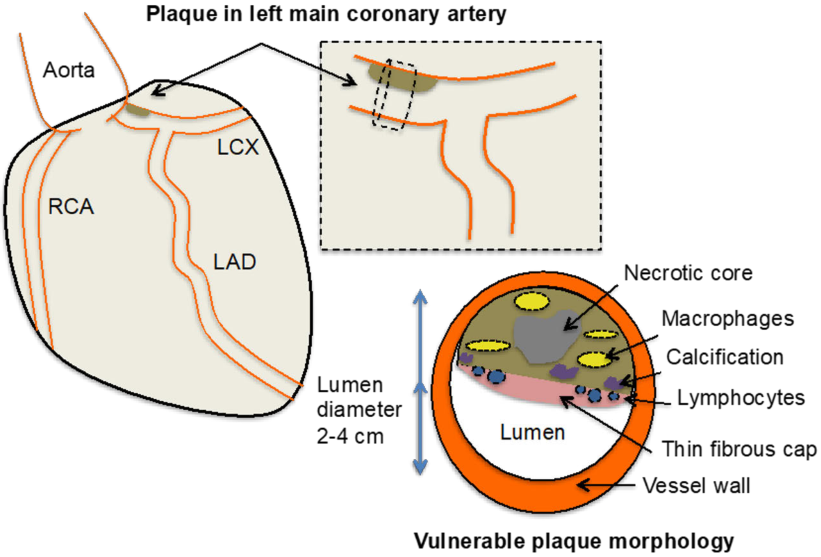

Figure 6. Illustration of coronary artery anatomy and vulnerable plaque morphology.

Morphologic characteristics of the vulnerable coronary plaques as inflamed fibrous cap thickness and length, plaque area, and necrotic core area are reviewed by Narula (Narula et al., 2008). Illustration of vulnerable plaque morphology is presented in Figure 6. Using pathological methods it has been shown that for vulnerable plaque fibrous cap thickness is less than 65 μm (Virmani et al., 2006) and length around 5 mm (Cheruvu et al., 2007), and for mean length of necrotic core is 8 mm and necrotic area is mostly less than 3 mm^2 (Virmani et al., 2006). The size of the ruptured plaques have been shown to be larger than stable ones, and the range of area of ruptured plaques is measured to be from 12 to 17 mm^2 (Ehara et al., 2004; Hoffmann et al., 2006) when imaging modalities as intravascular ultrasound (IVUS) and CT have been used. In editorial review of Strauss et al have vulnerable lesions reported typically occupy more than a third of the vessel circumference, often extend for 2 to 22 mm, being less than 1 mm thick, and having total lesion volume likely less than 0.1 mL (Strauss & Narula, 2007). After rupture of the plaque the size of a thrombus determines the likelihood of a clinical event. Strauss et al have reported that basis of autopsy findings fewer than 1% of atheroma ruptures will result in a clinical event (Strauss & Narula, 2007). However, the rupture of vulnerable plaques has potential to be a critical in converting asymptomatic atherosclerosis to a clinical event. Coronary artery angiography and IVUS studies before and after nonfatal ACS have found that hemodynamically insignificant lesions typically cause ACS (Fuster et al., 1992a, 1992b). Vulnerable coronary plaques are relatively non-stenotic (<75% cross-sectional area stenosis), have a larger lipid core and an often inflamed thin fibrous cap, and are associated with positive remodeling (Falk et al., 1995). Myocardial infarctions has also shown to occur more often in the proximal and middle part of the coronary arteries suggesting that these vulnerable areas may be achievable by imaging modalities (Wang et al., 2004).

2.4 Cardiac CT and MR imaging

CT technology has advanced rapidly in the begin of 20 th century so that 64-slice multidetector CT scanners have enabled full heart coverage within few heartbeats and during a single, tolerable 10 to 15 second length breath-hold (BH). When compared with conventional fluoroscopic angiography imaging CT has poorer spatial resolution but significantly better contrast resolution. Thus in CT image it is possible to distinguish blood from air, fat, and bone but unfortunately not from muscle or other soft tissue without iodinated contrast agent. Factors that affects to contrast resolution are tube voltage, slice thickness (i.e. detector width), pixel size, reconstruction filter, patient size and rotation speed of the gantry. Spatial resolution of CT imaging depends on many factors such as detector width, detector pitch, scan pitch, reconstruction algorithm kernels, tube current and voltage, pixel matrix, FOV and patient motion.

Due to recent improvements of hardware design, coil design, imaging sequence development and computing power, together with built-in unique multiplanar imaging capabilities, has cardiac magnetic resonance (CMR) imaging become a gold-standard method for evaluating cardiac morphology and function when compared to other cardiac imaging modalities. CMR imaging has specific challenges such as cardiac and respiratory motion, and flow phenomena to overcome. Therefore precise motion elimination techniques and novel CMR sequences are needed to correctly adjust to gain best image contrast between the blood and structures of cardiac tissues despite the fact that heart is constantly moving.

Two commonly used excitation pulse sequence families in MR imaging are a spin-echo and a gradient echo imaging techniques. Developments in CMR have gone in the direction of techniques that can be acquired during a single BH. Imaging speed is a key factor in most CMR applications and thus alternative signal acquisition strategies, as parallel imaging, have been developed. Parallel imaging techniques (SMASH, SENSE) rely on the use of multiple radiofrequency (RF) coils with different phased array elements. Simultaneous acquisition of spatial harmonics and sensitivity encoding are two widely used imaging techniques where imaging time has been able to reduce without significant loss of SNR (Pruessmann et al., 1999).

2.4.1 Coronary CT angiography

To be able to perform successful coronary computed tomography angiography (coronary CTA) the high spatial resolution CT is mandatory because diameter of coronary arteries starts proximally from around 5 to 3 mm and progressively taper distally to 1 mm or smaller. Spatial resolution of CT scanners has progressively improved to 0.4–0.6 mm on 64-slice scanners and for the newest vendors to 0.1 – 0.2 mm being at least as good as in invasive angiography (Toia et al., 2020). The temporal resolution is most dependent on the speed of the gantry rotation that is defined as the time it takes the gantry to make one complete 360° rotation. As the temporal resolution improves, the CT scanner is able to acquire motion-free images at higher heart rates. Most 64-slice scanners have a gantry rotation time of approximately 330 ms that results in a temporal resolution of 165 ms because "half-scan reconstruction" necessitates only 180° of data to reconstruct one CT slice image. Even better temporal resolutions can be achieved if multisegment reconstruction, or wider detector coverage or dual-source CT scanner is utilized (I. S. Rogers et al., 2010).

Advances in gantry speed and in the number of detector rows have improved the diagnostic accuracy of coronary CTA. At least 64-slice CTA has shown to have very good negative prognostic value for excluding CAD (Kajander et al., 2010). Some studies has reported that cardiac CTA has also potential to assess the fractional flow reserve (FFR) of coronaries (Nørgaard et al., 2014; Renker et al., 2014) with good accuracy when compared to the gold standard invasive FFR measurements. However, calcified vessels still represent a strong limitation to most CTA systems. CT based coronary plaque characterization has shown to be possible (Hamirani et al., 2010) and culprit (i.e. ruptured) plaques have shown to be larger than stable plaques (Hoffmann et al., 2006). After ACS culprit lesions have been shown to contain noncalcified soft plaques with attenuation of less than 30 HU. The vulnerable coronary plaques in CT have shown to be 110% positively remodeled, and also associated with spotty calcific deposits (Motoyama et al., 2007).

2.5 Clinical cardiac hybrid PET/CT imaging

All modern clinical PET devices are hybrid PET/CT (or PET/MR) devices. In hybrid device CT gantry and PET scanners are inserted together so that patient position remains unchanged between sequential CT and PET scans. Combined cardiac hybrid PET/CT imaging allows comprehensive and simultaneous information of heart morphology, as coronary anatomy, and molecular data as myocardial perfusion or metabolism in a single scanning session with good spatial co-registration between imaging modalities.

Cardiac PET imaging is considered a non-invasive clinical reference standard for absolute quantification of myocardial perfusion (Bengel et al., 2009; Qayyum & Kastrup, 2015) and viability imaging (Bengel et al., 2009; Lim et al., 2014). To obtain quantitatively accurate myocardial perfusion and viability PET images optimal and solid AC method is crucial (Kaufmann & Camici, 2005; Rajaram et al., 2013). Quantification of myocardial perfusion is based on mathematical compartment models (Kety, 1951) that describe the kinetics of most commonly used PET perfusion tracers as radiowater (^{15}O-H_2O) and ammonia (^{13}N-NH_3) (Hsu, 2013). To be quantitative these models have also to include limited resolution and cardiac motion related corrections in the model. The uncertainty of correct PET perfusion radiotracer concentration in myocardium is due to PVE, as PSF and spillover between chambers and myocardium (Hove et al., 1998; Hutchins et al., 1992; Nuyts et al., 1996), the impact of flow on myocardial extraction of ^{13}N-ammonia (Bellina et al., 1990) and the radiolabeled metabolites of ^{13}N-ammonia, which accumulate in the blood (Rosenspire et al., 1990). Due to limited spatial resolution of PET imaging the CMR and CT approaches has been widely estabilished to improve the detection of quantitative myocardial perfusion but yet these have not shown to be feasible in widely routine clinical practice (Qayyum & Kastrup, 2015).

Wollenweber et al have provided a comprehensive review of other more rarely applied cardiac PET imaging approaches, such as myocardial embryonic stem cell, sympathetic nervous system, extracellular matrix activation, apoptosis, angiogenesis and cardiac inflammation (i.e. sarcoidosis) imaging (Wollenweber & Bengel, 2014). Some of these phenomena are also important in vulnerable coronary plaque formation and rupture (Strauss & Narula, 2007). As these new cardiac PET imaging approaches aims to detect smaller spatial areas of the heart than routine applications novel, more sensitive and spatially more accurate PET imaging methods are needed.

2.5.1 CT based attenuation correction in cardiac PET

In hybrid PET/CT system it is routine to use the CTAC approach for attenuation correction of PET emission data. However, CTAC approach can also be a source of new image artifacts in cardiac PET imaging, and thus alter the accuracy of the diagnostics (Gould et al., 2007; Martinez-Möller et al., 2007). Potential problems, as image distortion, may arise in the process of scaling of the HU of CTAC data to 511-keV attenuation coefficients, especially if contrast media has been used during or prior to the CTAC scan, metallic objects (e.g., clips, prosthetic valves) are in the plane of the cardiac images, or arms are not up during the scans (i.e., arms at the side) (Daou, 2008; Kinahan et al., 2003; Visvikis et al., 2003). However, most relevant problem is the misalignment between CTAC and PET emission data. The misalignment can be due to inadvertent patient motion between the time of the

CTAC and emission acquisitions. More important source of error is that patient respiration and myocardial motion during the cardiac cycle generate misalignment between the CTAC and emission scan due to different scan lengths. Diagnostic cardiac CT scans are usually acquired during breath-hold and corrected for cardiac motion by prospective ECG-gating when the cardiac PET data is usually acquired during free breathing over several minutes (Klaus P Schäfers & Stegger, 2008). This means that these two datasets do not spatially overlay each other and an additional CT scan dedicated to AC is needed to perform in cardiac PET/CT studies if the aim is to get a best possible PET image quality.

2.6 Motion effects in cardiac imaging

Heart is under constant movement due to contraction and respiration that makes accurate cardiac imaging challenging. In fact, the spatial and temporal resolution of the imaging modalities are different for the organs that are influenced by the physiologic motions than when imaging non-moving organs (Daou, 2008).

2.6.1 Cardiac contraction motion effect

Although cardiac motion occurs in both systole and diastole the most of the motion occurs during systole just after isovolumetric contraction and just after isovolumetric relaxation phases (Wang et al., 1999). It has been reported that the motion of the coronary arteries is linear during the systolic phase and nonlinear during the diastolic phase (Saranathan et al., 2001). In CMR imaging total change in position along the long axis of heart between end-diastole and end-systole has shown to be the greatest at the base, which moves toward the apex about 13 mm during contraction, when the motion of the apex is nearly stationary (W. J. Rogers et al., 1991).

Wang et al have performed a conventional x-ray angiography study during breath-hold where the duration of the rest period of the cardiac cycle, cardiac motion velocities, displacement ranges, motion correlations, and reproducibility from heartbeat to heartbeat were studied (Wang et al., 1999). The rest period was determined as the time period when the motion of coronary arteries is less than 1 mm. They reported that the rest period located during diastole phase and was typically preceded by a gradually slowing of motion corresponding to the filling of ventricles, and was always followed by abrupt motion corresponding to the atrial systole at the late part of diastole. They showed that the rest period shortens as the heart rate increases when the systole is less variable. The rest period for the LCA (mean 131 ms) is longer than for the right coronary artery (RCA) (mean 120 ms). When heart rate exceeds the transition point at 55/min the rest period for both coronary arteries significantly decreases. At heart rates faster than 65/min the rest periods for both LCA and RCA approach to 70 ms asymptotically. Wang et al showed also that the RCA has a similar longitudinal displacement but a larger transverse displacement than does the LCA. The proximal part of the RCA also moved more than twice as much as the proximal part of the LCA, and the landmarks of the RCA exhibited larger velocities. Wang et al observed that motion of different points on the coronary arteries was not always correlated, and the pattern of coronary motion during cardiac cycle varies substantially from patient to patient. However, the coronary artery displacement ranges were clearly independent from the heart rate variations. Wang et al showed that, if no respiration and no change in cardiac output occurs, the coronary artery at the rest period returned to the same location from heartbeat to heartbeat, which is important finding considering the relative long lasting cardiac PET imaging.

Another 3D x-ray angiogram study by Shecter et al. showed that coronary arteries move consistently toward the left, inferior, and anterior during a cardiac contraction (Shechter et al., 2006). They reported that during cardiac cycle 3D displacement of the RCA ostium was 14.4 ± 1.9 mm (mean ± SD), left main origin 7.9 ± 2.2 mm, left main bifurcation 8.5 ± 1.7 mm, LAD 9.6 ± 1.3 mm, and LCX 12.1 ± 2.4 mm.

2.6.2 Respiratory motion effect

It has been reported that anatomical imaging modalities quantify at least 5 mm and mean 10.5 mm maximal respiratory motion amplitude of heart in the cranio-caudal direction during tidal breathing for all cardiac patients (Daou, 2008). Apical part of the heart has been shown to move slightly more than basal part of the heart due to respiratory motion in CMR study (Wang et al., 1995). In the same study mean respiratory motions of proximal parts of LCA and RCA has been reported to be in cranio-caudal direction 13.1 mm and 10.5 mm, respectively. The motion ranges to the other orthogonal directions was reported to be less than 3 mm for heart and coronaries. According to this finding the right to left and anterior to posterior motions of the coronary arteries are in the range of the diameter of the coronaries and almost negligible when compared to the spatial resolution of current PET scanners.

In cardiac PET respiratory motion of heart has been shown to cause image artifacts and quantitatively significant contrast degradation of true tracer distribution of myocardium (Livieratos et al., 2006; Ter-Pogossian et al., 1982). In hybrid cardiac PET/CT the respiratory derived misregistration between the PET and CTAC scans has shown to cause severe clinical problems, such as altered myocardial uptake particularly in the lateral and anterior regions at the lung-myocardial interface (Le Meunier et al., 2006) and misinterpretation of regional myocardial perfusion especially during cardiac PET stress imaging (Rajaram et al., 2013). It has been reported that in clinical cardiac PET perfusion studies misregistration is frequent and misalignment between CTAC map and PET image dataset is about 6 mm ± 6 mm (mean ± SD) (Martinez-Möller, Souvatzoglou, et al., 2007). In the same study it was reported that if misalignment is more than 6 mm the registration had clinically noticeable effects, and when the misalignment was more than 8 mm (29% of the scans) the effects on the tracer uptake were severe. However in the same study was also showed that artifacts due to misregistration can be eliminated by repeating cardiac PET reconstruction after manual realignment of the CT image data, or using an automated emission-driven correction method.

It has been shown that due to respiratory motion the effective FWHM of PET system can be formulated as follows (Daou, 2008):

$$Effective\ FWHM = \sqrt{FWHM^2 + Motion\ amplitude^2}$$

According to this formula the mean axial effective FWHM in cardiac PET is around 11.6 mm, when applying the current PET system FWHM (i.e. 5 mm) (Germano et al., 2016) and reported mean axial respiratory motion amplitude (i.e. 10.5 mm) (Daou, 2008). Remarkable is that when both cardiac and respiratory motions are taken into account the real effective FWHM of PET system in cardiac imaging is even higher. This underlines why both respiratory and cardiac motion handling is mandatory to accomplish high resolution cardiac PET images.

2.7 Motion compensations in cardiac imaging

Since the motion of heart is showed to be minimal at mid-diastole (Wang et al., 1999) the data is preferred to acquire during this period to eliminate the contraction motion related image artefacts. The contraction motion of the heart is commonly assumed to be cyclic and to follow the periodic ECG signal (Wang et al., 1999). Thus ECG signal is routinely used for controlling the data acquisition periods in cardiac CT and CMR. Recently ECG signal is also used in cardiac PET as a post-processing tool to eliminate cardiac contraction motion related image degradations. However, in precisely ECG represents electrical activity of the heart and not directly the mechanical contraction motion of myocardium. Thus it is suggested that seismocardiography may be more accurate to determine rest periods of cardiac motion cycle than ECG (Wick et al., 2012). However, the method’s efficacy is not yet proven in routine clinical studies.

With current fast cardiac CT scanners respiratory motion problem has been solved with breath-hold (BH), and no additional respiratory compensation method is needed. Most often in CMR the respiratory motion problem is also handled with sequential BHs. However, it has been reported that without any feedback signal to aid BH, the diaphragmatic cranio-caudal position can vary about 8.3 mm between different BHs at the same targeted BH-level (Liu et al., 1993).

Different measurement settings to follow physiology of respiration (Morel et al., 1983; Seppä et al., 2010; Wadhwani & Longini, 1973), volume changes of lungs (Konno & Mead, 1967) and variability of respiratory patterns in different body positions (Dawood et al., 2007; Houtveen et al., 2006; Ishida et al., 2011; Liu et al., 2009; Ruan et al., 2006) have been widely studied. During free breathing, most of the time is spent in a position close to that of expiration phase of the respiratory cycle. End-expiration level has also shown to be the most stable position in the respiratory cycle, while the end inspiration peaks shows much variability (Daou, 2008; Dawood et al., 2007; Liu et al., 2009).

Respiratory motion of thoraco-abdominal organs consists of the variable combination of translation, rotation, and deformation at the voxel level even for the same organ. Respiratory motion of the heart has shown to have more variability than contraction motion due to individual breathing patterns (Liu et al., 2009; Martinez-Möller et al., 2007). Thoraco-abdominal organ motions may neither be totally in phase with respiratory motion (Daou, 2008; Liu et al., 2009). However, good correlation between lung volume change and change of circumference or anterior-posterior displacement of ribcage or abdomen has been showed during tidal breathing (Gribbin, 1983; Konno & Mead, 1967). Strong correlations between diaphragm or heart motion and chest wall motion based respiratory signals have been reported in CMR (Santelli et al., 2011) and radiotherapy (Vedam et al., 2003).

Due to strong correlation between respiratory induced heart and diaphragm motions (Martinez-Möller et al., 2007; Wang et al., 1995) the diaphragm motion detecting methods have been widely studied to handle the respiratory motion effects, as degrading spatial resolution, in cardiac PET (Nehmeh & Erdi, 2008). In turn, wide individual variability has been reported between respiratory induced coronary and diaphragmatic motions during free breathing in real-time MRI (Danias et al., 1999). Thus the respiratory motion compensation has shown to be more complex problem to solve than cardiac contraction compensation, but in some extent, it has been shown to be possible with external respiratory motion detecting devices (Nehmeh & Erdi, 2008).

2.8 Gating as cardiac motion compensation in PET/CT

Gating, i.e. sorting the data into separate data files, i.e. gates, with respect to respiratory or contraction motion phase, is proposed as a method to minimize respiratory and contraction motion related image artifacts. Commonly gated cardiac

PET data is acquired in LM acquisition where synchronization information between emission data and ECG and/or respiratory gating signals is included in LM data structure as separate gating time event. This allows retrospective gated PET data reconstruction where the synchronization information, the gating time events and the gating signal processing is utilized to gain gated cardiac PET images. In consequence, each gated PET image contains only a portion of the detected coincidence events, which means that tradeoff for improved spatial resolution is impaired SNR in the gated PET images (Schäfers et al., 2005). To maintain both SNR and spatial resolution for diagnostic gated PET studies compensation methods as prolonged scan time, increased injected radioactive dose or motion correction algorithms are the options. In clinical PET only acceptable approach is the motion correction algorithms, which can include all original coincidence events in the one motion corrected PET image without affecting the patient throughput or patient radiation dose.

2.8.1 ECG based cardiac gating in PET and CT

Cardiac PET imaging has been shown to be possible using an ECG gated acquisition that can generate systolic and diastolic images of the heart (Hoffman et al., 1979; Ter-Pogossian et al., 1982). ECG gating has been shown to allow quite accurate estimations of left ventricular volumes, ejection fraction, and myocardial mass from cardiac PET images when compared to CMR (Khorsand et al., 2003; Porenta et al., 1995). For healthy subjects in ECG-gated cardiac PET the mean end-diastolic wall thickness and mean endocardial wall radial motion has been reported to be 15 mm and 5 mm, respectively (Freiberg et al., 2004). However, in the same study the endocardial wall motion reported systemically underestimated and myocardial end-diastolic wall thickness overestimated by ECG-gated cardiac PET when compared with CMR. In this study of Freiberg at al. RR interval of ECG was divided into 8 bins in gated cardiac PET acquisition and gated cine MRI acquisition was performed with a fixed-frame duration of 50 ms during systolc phase.

In cardiac CT during BH the ECG gating can be either prospectively triggered or retrospectively gated. Retrospectively gated cardiac CT is usually acquired in helical mode where tube current is delivered throughout the cardiac cycle, and thus permits reconstruction of a cine data set of cardiac contraction. The helical mode imaging is more forgiving for heart rate variabilities during the CT scan and thus improves the coronary CT image quality for all coronary artery segments, which motions are not exactly in synchrony (Wang et al., 1999). The benefits of retrospective approach come at the cost of increased and often unnecessary radiation exposure to the patient.

When heart rate is regular and below 65/min the prospective ECG triggering, known as “step and shoot” mode of acquisition, is usually applied for coronary CT. Prospective triggered cardiac CT acquires the axial image data during the predefined R-R interval of ECG over a few consecutive heartbeats by moving the patient table stepwise during the every other heartbeat. The R-R intervals at the mid-diastole, i.e. from 50% to 80% intervals, are common because during this interval the motion of coronaries has been shown to be minimal (Wang et al., 1999). The primary benefit of prospective-triggered CT scan is the reduction of the patient radiation dose. In addition, image quality may be compromised with misregistration and slab artifacts if ectopic beats, arrhythmias, or heart rate variability occurs during the CT acquisition.

2.8.2 Respiratory gated cardiac PET/CT

The most common way to acquire thoracic region PET scan is during shallow free breathing. This traditional method maintains the count statistics and leads to quite good image quality. However, it does not address the problem of decreased effective PET resolution due to respiratory motion. It has been shown that in cardiac PET/CT a simple, and very often used, approach using a fast low-dose CT scan without gating and during a breath-hold for AC of cardiac PET is inappropriate and may lead to false diagnostic conclusions (Goerres et al., 2002; Schäfers et al., 2005). Ideally, both the PET and CTAC scans should be acquired with cardiac and respiratory gating to ensure an accurate quantitative image reconstruction. However, if no respiratory or cardiac motion correction is performed for cardiac PET data the suggestion for optimal CTAC is to acquire low dose average cine CT data slowly during free breathing over at least one breathing cycle and without ECG gating (Cook et al., 2007; Liu et al., 2009; Pan et al., 2006). This allows better spatial co-registration between CTAC map and PET data, and thus eliminates the misregistration problems.

Methods that use gating to overcome respiratory related problems are based mainly on acquisitions where PET data is acquired on list mode together with an external respiration detecting device that produces a synchronized signal that follows the frequency and magnitude of respiration of patient during the scan. Most commonly used methods are based on chest wall movements or lung volume changes of the patients. Chest wall motion can be detected with an elastic belt or a camera-based method. Both methods are commonly used for respiratory gating in radiotherapy (Li et al., 2006), CT (Nehmeh et al., 2004; Pan et al., 2004), and PET (Nehmeh et al., 2002) imaging. Lung volume changes can be measured indirectly using spirometry, which detects airflow changes in respiratory tract during breathing. Spirometry is commonly used in clinical pulmonology and during anesthesia. Spirometry has been used as a research tool to trigger gated radiotherapy (Zhang et al., 2003), quantitative CT (Kalender et al., 1990), and gated PET (Zubal et al., 1984). Temperature sensor (Boucher et al., 2004; Ehman et al., 1984), bioimpedance signal (Koivumäki et al., 2014; Koivumäki et al., 2015; Wadhwani & Longini, 1973) and accelometer based seismocardiography (Tadi et al., 2014) methods have also been proposed to be possible to apply for respiratory gating in research settings. Inherent PET list mode data is also introduced as a self-respiratory gating technique in research settings and have shown to be comparable with techniques based on external signal monitoring (Büther et al., 2010). However, the data-driven self-gating methods have developed slowly and these have been commercially available for only a short time on the latest and most advanced PET/CT scanners.

Respiratory gating in PET is done by either time-based or amplitude-based methods. The time-based methods divide the respiratory signal into different phases with reference to time in each breathing cycle. Then the PET list mode data from corresponding time phases of each breathing cycle are summed up into separate time-based respiratory gates. However, the depth of respiration is not taken into account in the time-based methods. The amplitude-based methods divide the respiratory signal into different phases with reference to the magnitude of the signal. Then the PET list mode data from corresponding amplitude phases of each breathing cycle are summed up into separate amplitude-based respiratory gates. Both of these primary methods can be further subdivided two ways depending on the method of selecting the gate width, i.e. either variable or constant. In the variable-gating method, the width of each gate is calculated individually whereas in the constant-gating method the width of all gates is equal. Dawood et al have been compared different time- and amplitude-based respiratory gating methods with respect to their noise properties and their accuracy with respect to capturing the respiratory motion in cardiac PET imaging using a camera-based abdominal motion sensing method to acquire respiratory gating signals (Dawood et al., 2007). The cardiac contraction motion was neglected and eight respiratory gates for all gating methods were used in their study. They reported that for motion capturing the amplitude-based methods were superior to time-based methods, and the variable-amplitude-based method captured the respiratory motion best while keeping a constant noise level of gated PET image among all respiratory phases. Dawood et al concluded in their study that the large differences between amplitude- and time-based gating methods can be explain due to irregular and asymmetrical breathing patterns of the patients.

Daou et al have been analyzed in their review article the benefits and disadvantages of the reported respiratory gating methods to minimize respiratory related motion problems, i.e. CTAC and PET data misregistration and PET image blur (Daou, 2008). The equal goal for these methods is to minimize the respiratory motion in gated PET images and at the same time guarantee the correct co-registration between the CTAC map and PET images. Thus the respiratory corrected PET data should allow a net improvement of the effective resolution of the PET system approaching that of the PET system without motion. This should translate into an improvement of PET sensitivity for detecting small uptake lesions and more accurate quantification of tracer uptake and volume of PET lesions (Daou, 2008). To achieve these goals the best suggested respiratory gating approach by Daou et al was to unite respiratory gated 4D-PET and 4D-CTAC scans, which both are acquired over a complete respiratory cycle (Nehmeh et al., 2004; Pan et al., 2004). Nehmeh et al have been shown that this 4D PET/CT approach significantly improves the co-registration of PET and CT lesions, reduces PET-derived tumor volumes, and increases lesion SUV (Nehmeh et al., 2004). However, major disadvantage of 4D-CTAC scan is significantly increased radiation dose to the patient when compared to normal CTAC scan. Other suggested possible approach to overcome the missregistration problem between PET and CTAC scans is a single-gate respiratory synchronized PET where end-expiration or end-inspiration respiratory gated PET image is matched with an end-expiration or end-inspiration CT scan that is acquired during a breath-hold (Fin et al., 2008; Meirelles et al., 2007; Nehmeh et al., 2007).

All respiratory gated PET methods suffers the low SNR of the gated PET images due to the fact that only a part of the acquired PET data is used for image reconstruction. To overcome this loss of statistics different image level transformation methods to maintain the statistics of gated PET data are reported, and one of the first was a rigid-body transformation method (Livieratos et al., 2005). Also an optical flow based method has been reported where PET image data is transformed from the individual respiratory gates to one static phase within the breathing cycle and then transformed images are added up to get a complete dataset with minimum motion that contains all acquired information (Dawood et al., 2008; Dawood et al., 2006). This transformed PET dataset is then reconstructed again with a co-registering CTAC scan which has been taken during a breath-hold at same static phase within the breathing cycle than the PET image. These basic optical flow methods assume that the brightness of the objects remains constant between the frames. This condition is not fulfilled in cardiac PET data where the brightness of the myocardium is not accurately resolved due to the PVE. Thus it has been proposed an improved a mass preserving optical flow method of cardiac motion correction in 3D PET data that corrects the cardiac motion efficiently despite the PVE of the cardiac PET data (Dawood et al., 2013). Also a joint image and motion reconstruction method, that exclusively works on the measured gated PET data, has been proposed to improve PET image quality without any external motion measurements (Blume et al., 2010; Blume et al., 2012).

2.8.3 Dual gated cardiac PET/CT

Ter-Pogossian et al have been reported that degradation of reconstructions of true tracer distribution occurs in cardiac PET due to both contraction and respiratory induced motion of the heart. They also proposed that the motion related influences could be minimized using dual gating (DG) approach i.e. simultaneous gating with respect to both cardiac contraction and respiration (Ter-Pogossian et al., 1982). Zubal et al have been shown that dual gated nuclear cardiac imaging is feasible using list mode acquisition together with respiratory and ECG signal acquisition which are further synchronized with the list mode data (Zubal et al., 1984). They concluded that dual gated cardiac images show better definition of the myocardium and therefore have the potential of improving the resolution and detectability of small cardiac lesions, and the characterization of cardiac wall motion. After that Klein et al have been introduced a DG-method using online histogramming of PET data together with signal processing software (Klein et al., 1998). Their real-time DG-method was based on prospectively defined time-gating with constant gate lengths. This Klein’s method has been reported to be vulnerable for heart and respiratory rate irregularities, which make it inappropriate to the most patient studies (Martinez-Möller et al., 2007). Dual-gating method for mouse heart PET imaging has been reported to be a feasible but the approach is not suitable for human cardiac studies due to differences of breathing patterns between mouse and humans (Yang et al., 2005). Martinez-Möller et al have been reported a potential technique for dual gated cardiac PET studies using list mode acquisition together with additional signal prosessing for a belt derived respiratory gating signal (Martinez-Möller et al., 2007). In their method both respiratory and ECG gating is based on time-gating with constant gate length definition. The reported results showed that the DG-technique is able to eliminate partly the effects of motion induced by respiration and cardiac contraction. Buther et al have been introduced a self-gating DG-technique for cardiac PET imaging that analyses the PET list mode data stream on a frame-by-frame basis to obtain the contraction and respiratory motion of heart (Büther et al., 2009). They reported that their self-gating technique is comparable to conventional signal based gating methods to detect the myocardial motions in PET. However, the self-gating method by Buther et al or the dual-gating method by Martinez-Möller et al are scanner related approaches and are not designed to a small target, as a vulnerable coronary plaque, detection in PET.

2.9 Small target cardiac PET/CT imaging

When aiming to small target cardiac PET/CT imaging, as the vulnerable coronary plague imaging, in addition to motion related problems, i.e. motion amplitude, motion patterns and gating methods, it’s needed to be consider other relevant effects that affects the detection of the small moving targets in PET (Fox & Strauss, 2009; Lucignani, 2009). Main additional considerable effects are the effect of target size versus spatial resolution of PET, and thus PVE, TBR and reconstruction algorithms of the PET system (i.e. choices of reconstruction parameters as matrix size, iteration numbers and smoothing).

2.9.1 Motion effects in small target PET/CT imaging

In Figure 7 is illustrated in general, how motion of small size target affects on detected activity, and thus image quality in PET. Park et al have studied how the linear and periodic motion affects the detection of small targets in PET/CT imaging (Park et al., 2008). They put the spherical targets in the dynamic thorax and NEMA IEC body phantoms and evaluated the effect of one-dimensional translational motion amplitude (1 to 2 cm), target size (diameter from 10 to 37 mm), TBR value and gating numbers on the target volume activity and recovery coefficient (RC) behavior. RC values were based on a maximum voxel (3 mm width) activity value inside the target volume.

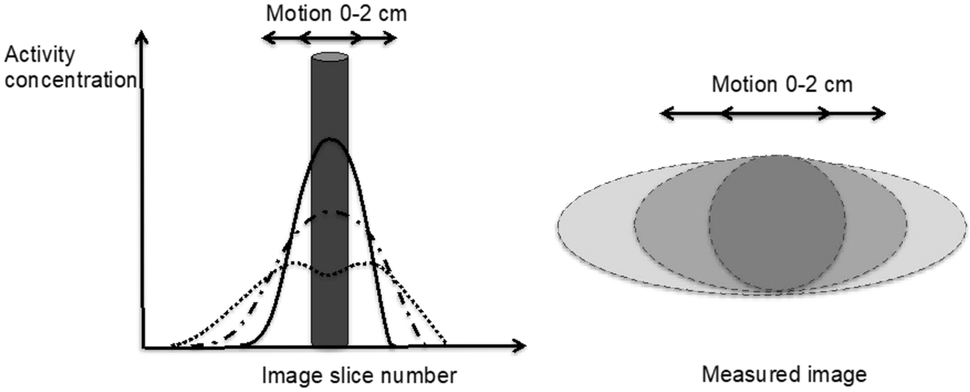

Figure 7. Illustration how motion of small target affects on detected activity and image quality in PET. Motion reduces the observed activity of small target and blurs image quality.

Park et al reported that without gating even 1 cm respiratory motion significantly lowers the measured activity value of the all size of the targets, and thus also the RC values of the targets, when compared to static mode. The report showed that signal loss not only depends on the magnitude of respiratory motion amplitude but also on respiratory pattern, especially when constant time-based gating was applied. However, the main conclusion were that 4D gated PET successfully recovered most of the RC loss due to the motion, and the best values where measured at the end of exhalation and inhalation phases of the respiration when respiratory motion has a sinusoidal pattern and the time-based gating approach is used. The main conclusion of their study was that 5-bin constant time-based gating was enough to recover the RCs very close to the standard reference values for all size of the spheres, with or without the background activity, when 2 cm motion amplitude was applied. Also the measured target volume activity values were reported to be optimal when 5 gating bins were used. If fewer bins were used, the volumes of all spheres were overestimated due to the smearing effect of motion. However, when more than 5 gating bins were used they reported that it resulted in the larger overestimations of RCs due to the poor counting statistics and higher image noise, and this effect was more significant as the sphere size was larger or as the TBR decreased. They also informed that the applied 5-bin gating method was equivalent to the 4 min scan time, which is in the range of a common scan time used in clinical 3D PET scan protocols. When measuring the image quality effects of the targets, they noticed that for the largest 37 mm sphere that the SNR became worse whereas lesion detectability, contrast to noise ratio (CNR), became better when the TBR became higher. Overall both SNRand CNR values were deteriorated as the number of gating bins was increased. Notable in the study of Park et al was that with 2 cm motion the smallest 10 mm diameter sphere was reported to be visible when the used TBR were at least 8 but with the TBR value of 4 the smallest sphere was not visible any more even when the gating was applied.

2.9.2 Vulnerable coronary plaque PET/CT imaging

It has been reported that the higher the TBR value the more likely small moving target can be detected by PET (Park et al., 2008; Strauss & Narula, 2007). When focusing on vulnerable coronary plaque PET imaging it means that used tracer should have high specific affinity to the plaque structures when compared to it’s surroundings. As vulnerable coronary plaque has ongoing inflammation process, the 18F-FDG has been proposed to be possible target for vulnerable atherosclerotic plaque PET imaging (Fox & Strauss, 2009; Vallabhajosula & Fuster, 1997). Rudd et al. were first to report a potential relationship of focal 18F-FDG uptake in carotic PET images with carotid atherosclerosis on symptomatic cerebrovascular disease patients (J.H.F. Rudd et al., 2002). After that Tawakol et al showed a correlation between macrophage density and TBR of 18F-FDG uptake in inflamed human carotid endarterectomy specimens (Tawakol et al., 2006). The measured TBR values of 18F-FDG uptake in carotic plaque were at most 5 in their study.

Whereas from results of Soret (Soret et al., 2002) and estimations of Strauss (Strauss & Narula, 2007) can be derived that if the average size of vulnerable coronary plaque (volume less than 0.1 mL) are aimed to detect with PET the true TBR value are required to be approximately at least from 10 to 20 with the current generation of PET scanners when perfect plaque motion detection and correction are explicitly assumed to be achieved. In same article Strauss et al have gave their opinion on the instrumentation that is needed to image inflamed coronary plaque. Their statement is that all studies will require respiratory and cardiac gating to eliminate motion and thus permit a possibility for coronary plaque imaging. Their opinion was that resolution of SPECT scanners is too low to achieve vulnerable coronary plaque imaging but with PET it's possible to achive if the TBR of used tracer is high enough.

Only few clinical patient studies have been reported that vulnerable coronary plaque detection using 18F-FDG PET could be possible (Alexanderson et al., 2008; Dunphy et al., 2005; Wykrzykowska et al., 2009). Williams et al have been reported that the patients who have a very high-fat, low-carbohydrate, protein-permitted (VHFLCPP) diet before 18F-FDG injection have significantly lower myocardial SUV values than the patients who follows a standard fasting diet instructions (Williams & Kolodny, 2008). This specific diet preparation exploits well-known inverse metabolic relationship between glucose and fatty acids that is based on glucose-fatty acid cycle (Randle et al., 1963). This specific diet is potential method to improve the TBR of 18F-FDG uptake into vulnerable coronary plaque and thus improve the detection of the plaque in PET (Fox & Strauss, 2009). Also a few pharmacologic interventions have been proposed to have possible desirable affect on lesion 18F-FDG uptake (Fox & Strauss, 2009).

3 Aims

This PhD consists of eight different substudies that are published in four individual publications. The included substudies, applied methods and aims of the substudies are presented shortly in Table 1. All substudies where PET/CT scans were acquired the Discovery VCT (VCT) scanner (General Electric Medical Systems, Milwaukee, WI, US) was used. Spesific aims of the study are:

1. To develop a novel DG-method for small target cardiac PET imaging. Hypothesis: (1) The method is feasible to construct for cardiac PET imaging with widely available commercial PET/CT scanner. (2) The method excludes most of respiratory and contraction motion of heart in cardiac PET imaging, and maintains high enough sensitivity to detect small active targets of heart. (3) The method improves the detection of hot and small cardiac structures, such as artificial vulnerable coronary plaques, when compared to standard gated PET imaging methods. These hypothesis where tested by applying the self-programmed DG-algorithm to two self-reconstructed phantom PET studies. (Publication I)
2. To enhance and validate the quantitative DG-method. Hypothesis: The enhanced DG-method is quantitative after precise parameter adjustments. The hypothesis were tested by comparing validated clinical PET methods and the enhanced DG-method in the standard NEMA image quality phantom PET study. (Publication II)
3. To study the performance of the quantitative DG-method in animal and clinical patient cardiac PET imaging. Hypothesis: The DG-method improves the quantitative detection of small artificial coronary plaques of minipigs, and small, hot and focal 18F-FDG uptake lesions in the myocardium and in the coronary vessel walls of the cardiac patients when compared to standard cardiac PET imaging methods. The hypothesis were tested by imaging eigth minipigs which had inserted small radioactive target in their coronaries and cardiac sarcoidosis suspected or CAD patients (Publication II)

4. To study spirometry derived lung volume signal amplitude and pressure belt signal amplitude feasibility for cardiac vessel motion detection in cardiac MRI. To study spirometry based lung volume signal and thoracic impedance signal accuracy in respiratory gated cardiac PET. Hypothesis: (1) The signal amplitude change for two studied respiratory methods have at least good linear relation with the cardiac vessel motions in the three-level breath-hold cardiac MRI. (2) The change of the lung volume signal amplitude has at least good linear correlation with the motion of the center of the myocardium 18F-FDG activity in the respiratory gated cardiac PET. (3) Simple 3-lead ECG configured thoracic impedance signal is feasible for respiratory gated cardiac PET, and the detected myocardial motion amplitude and pattern in cardiac PET is comparable with the lung volume based respiratory gating method. The first hypothesis was tested in the cardiac MRI during the breath-holds with nine volunteers. Second and third hypothesis was tested with clinical 18F-FDG cardiac patients by applying the respiratory gating in PET data. (Publications III and IV)

Table 1. PhD consists of eight different substudies that are published in four different publications. Overall three different imaging modalities are applied for these studies. Cardiac motion during these studies are managed with using ECG gating and four different respiratory gating signals. RPM = video monitored chest wall motion, Vol = spirometric lung volume change, Imp = 3-lead ECG based thoracic impedance signal, Belt = chest wall motion induced pressure changes in elastic belt. Gating options: Man = manual mode measurement, Simu = simulation mode measurement, x = real motion measurement, - = not applied. CMA = Center of myocardium 18F-FDG activity

	Publication	Modality	Gating				Aim/Focus
Imaging setups			ECG	RPM	Vol	Imp/Belt	
2D-phantom	I	PET	Man	Man	-	-/-	DG-algorithm
Heart phantom	I	PET, (CT)	Man	x	-	-/-	Plaque
NEMA phantom	II	PET	Simu	Simu	-	-/-	Quantitation
Minipig coronary	II	PET, CT	x	x	-	-/-	Plaque
Heart sarcoidosis	II	PET	x	x	-	-/-	Motion
CAD coronary	II	PET, CT	x	x	-	-/-	Plaque
CMA of heart	III/IV	PET, (CT)	-	(x)	x	x/-	Motion
Cardiac vessels	III	MR	x	-	x	-/x	Motion

4 Materials and Methods

4.1 Ethical approvements and study subjects

All clinical PET/CT studies were conducted according to Good Clinical Practice, the Declaration of Helsinki, and US 21 CFR Part 50 (Protection of Human Subjects) and Part 56 (Institutional Review Boards). The protocols of human PET/CT studies and animal study were submitted to the appropriate Ethics Review Committee (ERC) or Institutional Review Board (IRB), and their written unconditional approval were obtained before commencement of the studies. Written informed consent for the human PET/CT studies were obtained from all subjects before protocol-specific procedures were carried out. The consent form generated with the assistance of study board (SB) and was approved by the ERC/IRB. All participants were also informed of their right to withdraw from the study at any time.

In study I no patients or volunteers were recruited. In studies I and II were the feasibility of the reconstructed dual gated cardiac PET/CT imaging method tested with the self-constructed and the certified phantoms. Patients participating in the PET/CT studies were recruited through the Department of Cardiology of the Turku University Hospital (Study II, III and IV). In cardiac MRI study (part of the Study III) volunteers from the institution of the PET Centre were recruited. In study II minipigs was used, and these animals were taken care and crown according to laws of animal care.

4.2 PET/CT scanner characteristics and performance

All PET/CT studies was performed using Discovery VCT (VCT) scanner (General Electric Medical Systems, Milwaukee, WI, USA), which combine a helical 64-slice CT scanner and BGO block PET tomograph with a large 70-cm patient port. CT scanner covers 40 mm axial depth with a slice thickness of 0.625 mm enabling an accurate cardiac CTA imaging. The PET scanner is a multi-ring BGO block detector system of 8x6 matrix where BGO crystals are arranged in 24 rings. Crystal dimensions are 4.7 mm × 6.3 mm × 30 mm in transaxial, axial and radial direction, respectively. Numbers of crystals are 13,440. Energy window option of 425–650 keV and coincidence time window 9.3 ns were used for 3D mode acquisition.

In 3D mode at the centre of the FOV spatial resolution of VCT PET scanner in transaxial and axial direction is reported to be 5.12 mm and 5.18 mm, respectively. The sensitivity at the centre of FOV is reported to be 8.8 cps/kBq. The system scatter fraction is reported to be 33.9% in 3D mode at energy of 425 keV. The more spesific technical specifications and performance values for VCT PET/CT scanner can be found from Teräs et al (Teräs et al., 2007).

4.2.1 PET scanner technical features for gated PET

The GE Discovery VCT PET/CT scanner has the capacity to acquire data in a LM file in which every event occurring during the acquisition is written in a chronological manner. Benefit of the LM acquisition is that it enables clinicians to create sinogram data of different durations. In the DG-project, this LM acquisition option enables easier post processing of the dual gated PET data. Before the DG-project started the scanner was upgraded in order to have two separate trigger signal input connectors that were able to send the time informations of the trigger events into the LM file (Figure 8 on left). At the time of the project started this capacity was an additional feature and was only accessible for research purposes. The structure of the LM file is coded in 32-bit words, which represent time markers, ring positions, detected coincidence events and trigger events. The time markers are written in every millisecond in the LM file. The trigger events from the two gating devices have their identifiers which are differentiated by a 7 bit tag at the end of the 32-bit words in the LM file.

Figure 8. On left is a photo of two different trigger input connectors of the scanner. On right is a photo of ECG monitor that is connected to the ECG trigger input where it can send the trigger information from the R-peak of the ECG-cycle.

4.3 Gating devices

4.3.1 ECG monitoring device

In the PET patient studies ECG was monitored using a commercial ECG monitor IVY 3150-B (IVY Biomedical Systems, USA) (Figure 8, image on right) using standard 3-lead ECG cables and standard electrode positions (Figure 9, image on lower left). The sampling frequency of the ECG monitor was 300 Hz. The ECG monitor can also generate a trigger event at every R-peak of the ECG cycle that was directly sent to the PET/CT scanner in the gated PET studies. The ECG monitor can also be set as a simulation mode, when it simulates the steady heart even if the electrodes are not attached to the patient. This simulation mode was applied in NEMA phantom study (see section 4.7) to generate the cyclical ECG trigger events into the PET LM data stream.

4.3.2 Respiratory monitoring devices

Four different commercial respiratory motion monitoring methods was tested and analysed for respiratory induced cardiac motion detection and/or respiratory gating. The first method was a clinically accepted device, called Real-Time Position Management (RPM) Respiratory Gating System (Varian Medical Systems, USA), that had been used as a respiratory motion detecting and gating device in thoracic region PET/CT imaging (Nehmeh et al., 2002; Nehmeh, et al., 2004). This RPM device constructs from two parts (Figure 9, upper row images). First part is a small plastic block, which front surface has a one below the other two infrared-light reflective markers. Second part is a charge-coupled devide (CCD) camera that tracks the vertical displacement of the pair of reflective markers on the plastic block that is attached on the patient's chest. Thus the RPM device follows one-dimensional vertical expansion and contraction motion of the chest wall that has shown to correlate with the diaphragm motion (Gribbin, 1983; Konno & Mead, 1967), which in turn has shown to correlate with respiratory induced heart displacement (Wang et al., 1995). This RPM device is designed to monitor the respiratory motion with a sampling frequency of 25 Hz. The RPM also generates a trigger event every time the patient inspiration turns to expiration, and sends it to the separate respiratory trigger input-port in the PET/CT scanner (Figure 8, image on left) so that the trigger time information is included also in the PET LM data stream. The trigger moment is referred as zero phase of the respiratory cycle. The acquired respiratory signal data together with the information of the trigger events was saved in a separate log file. The limiting ability of the first version of the RPM device was the fact that the log file was able to save only the 8 last minutes of the acquired respiratory signal. This limitation restricted the length of the 2D-phantom and the dynamic heart phantom gated PET studies to 8 minutes, before the version upgraded (version 1.6), which had possibility to save longer periods of respiratory signal data. This RPM device has additional rotating phantom to which the plastic block was able to attach so that the device was able to simulate the respiratory motion. This simulation option was used in NEMA phantom study (see section 4.7). Otherwise the infrared-light reflecting block was attached to with a tape on the abdomen-chest border of the subjects of the PET studies. In the dynamic heart phantom PET study an additional stand for the block was reconstructed to the phantom so that the horizontal (respiratory mimicking) motion of the phantom box (see section 4.6) was connected to the vertical motion of this stand/block.

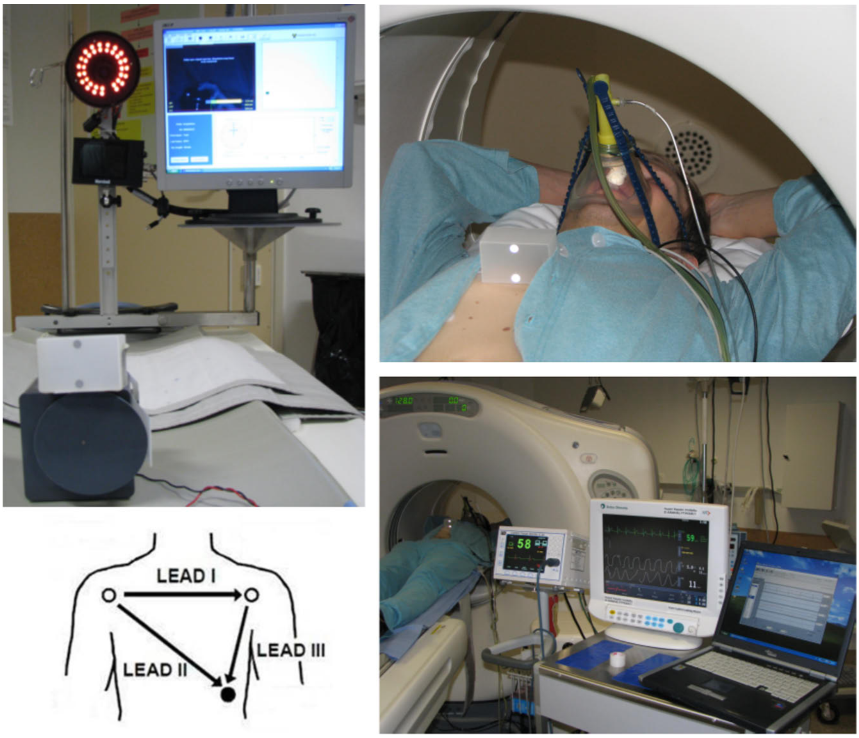

Figure 9. ECG and respiratory monitoring setups. Upper left image: RPM's IR-camera that follows respiratory motion. Upper right image: The plastic block with infrared markings over the chest to follow patient's respiratory motion. Air-tight mask that is connected to Datex Ohmeda monitor for spirometer measurements. Lower left image: Standard 3-lead ECG configuration that was used for thoracic impedance measurement with Datex Ohmeda monitor. Lower right image: From left to right is the PET/CT scanner, IVY ECG-monitor, Datex Ohmeda monitor, and laptop for spirometer and impedance signal processing.

As an additional option the RPM device can also be used to control dynamic CT scans from which respiratory gated CTAC maps can be generated for the phase-matched PET emission studies. With this option the RPM device controls the CT tube acquisition so that dynamic CineCT scan (120 kV, 30 mA) (Nehmeh, et al., 2004; Pan et al., 2004) is acquired over one RPM controlled breathing cycle. When applying the commercial post-processing tools to this dynamic CT data, it can be separate to different respiratory phases by exploiting the simultaneously acquired RPM respiratory signal. This procedure produces N number constant width time-based respiratory gated CT data files from the acquired breathing cycle. Further on these respiratory gated CT files can be used for AC with similarly gated matched PET emission data. This respiratory gated CineCTAC option is exploited in the respiratory and dual gated human cardiac PET/CT studies (Study II, III and IV).

In spirometry measurement airflow signals were acquired using two slightly different monitoring devices. In the cardiac MR and PET studies were used MR compatible iMM MRI patient monitor including an E-MRICAiOVX airway module (GE Healthcare) and S/5 Datex Ohmeda anesthesia monitor (GE Healthcare), respectively. In airflow measurement settings subjects wore an air-tight breathing mask which was connected to the monitors (Figure 9, images on right) to which subject’s airflow signal during the MR or PET scan was stored. The sampling frequency for both MR and PET spirometry monitors were 25 Hz, and the acquired signals were saved to a log file. These airflow signals were post-processed off-line so that derived lung volume chance signals were used for signal analysing, motion correlation and respiratory gating in the performed cardiac MR and/or PET studies (see sections 4.9 and 4.10)

The S/5 Datex Ohmeda anesthesia monitor has an additional option to monitor and save the signal from the 3-lead surface electrodes. This option allows filtering the signal from the 3-lead electric cables so that it separates an ECG signal and a thoracic impedance signal from the original signal. In the applied measurement set standard ECG cables, standard Blue Sensor R ECG electrode pads (Ambu, Ballerup, Denmark) and standard ECG electrode positions were applied (Figure 9, image on lower left). Thoracic impedance was measured by supplying current between two electrodes and by measuring the differential current from the third electrode (Figure 9, on lower left). The input current was 200 μA and frequency 31 kHz. The used measurement set for electrode locations and the choice for the supplying current electrodes followed instructions of user manual supplied by the manufacturer. The sampling frequency for the ECG signal was 300 Hz and for the thoracic impedance signal 25 Hz. Similar as the lung volume signal both ECG and impedance signals were saved to files on the S/5 monitor for off-line post-prosessing.

The fourth studied method was an elastic belt (Invivo) that was integrated in used Philips Gyroscan Intera 1.5 T Nova Dual MRI scanner. The device had been as an optional respiratory gating device for thoracic region clinical MRI studies in Turku PET Centre. Before the MRI study this elastic belt is attached firmly over the subject's chest-abdomen border. The idea of the belt function is that during breathing the belt stretches and shortens along the chest wall motions. Doing so a pressure sensor inside the belt creates a respiratory signal that reflects the stretchability of the elastic belt. The sampling frequency for belt signal was also 25 Hz and the signal was saved to a separate file for off-line postprosessing.

4.4 Dual gated cardiac PET method (Public. I)

Dual-gated cardiac PET method was developed for the studies that are performed using the Discovery VCT PET/CT scanner (General Electric Medical Systems, Milwaukee, WI, USA) in the LM acquisition mode. The ECG and respiratory monitoring devices that were able to generate the trigger events into the LM file were used for the synchronization between LM file and the monitored ECG or respiratory signal information. Thus the DG-method can separate the acquired PET data between the dual gated LM files in order of the one millisecond. The main idea in the DG-method to overcome the cardiac contraction motion is to focus on the end-diastolic part of the ECG cycle that has shown to be most stable one (Wang et al., 1999) allowing to optimize the dual gated image statistics in the diastolic PET images. Thus the duration of systolic ECG phases were fixed and only the last diastolic ECG phase was allowed to vary during the date definition process of the DG-method. The respiratory gating part of the DG-method is optimized for amplitude-based constant width gating, but the method is also adjustable for time-based gating or variable-width gating approaches. The main assumptions of the DG-method were the following: respiratory motion and heart rate of a subject stays relatively stable during a PET scan; baseline of the respiratory gating signal stays relatively stable; and the trigger signal information are sent to the LM data at the moment when the inspiration turns to expiration and at every R-peak of ECG cycle. These principles and the workflow of the DG-method are illustrated in Figure 10 and Table 2.

4.4.1 Dual gating procedure in cardiac PET

After dual gated PET LM acquisition the dual gated LM file and raw data files (RDFs) were exported from the PET/CT scanner database for the offline data processing. Simultaneously acquired respiratory gating signal data was also exported for the offline processing. The DG-algorithm to analyse gating signals and to separate the dual gated PET data accoring to these gating signals were self-designed and self-programmed using MatLab programming environment (MathWorks, Inc.) that were run on a virtual 64-bit server computer in the Turku PET Centre.

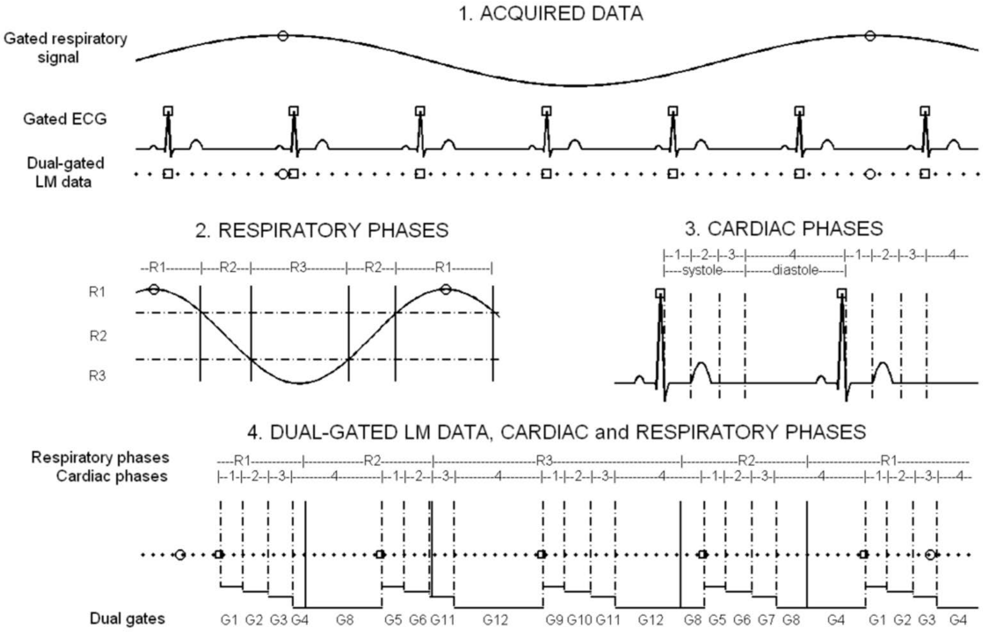

Figure 10. Schematic illustration of the dual gating method: ECG signal is separated to four gates of which three are during systole and fixed length, and the fourth represents diastole which lenght is allowed to vary. Respiratory signal is separated to three constant-width amplitude gates. Trigger event time information that are sent to PET LM data stream are illustrated with open square (for ECG) or open circle (for respiration). This leads to 12 dual gates (G1 to G12). Dot = LM data event

In the beginning of the workflow the self-programmed DG-algorithm determines trigger events for a dual gated LM file and a respiratory gating signal file. After that the algorithm synchronizes time events of the respiratory gating signal and the dual gated LM file using the cross correlation spectrum between the time differences of the determined trigger events from the both files. According to choices of respiratory and ECG gate numbers, amplitude or time based respiratory gating, and ECG gate definition, the algorithm defines time event information for the transition points between the dual gates. Last the algorithm separates the LM data into subgroups according to information of transition points of the dual gates and the information of time synchronization between the respiratory gating signal and the LM data. Thus dual gated coincidence PET data of each subgroup is copied to a file with same order number than the corresponding dual gate. According to this procedure 12 dual gated LM files are generated in default setting where three respiratory and four cardiac gates are used (see Figure 10). The format of new files and the original LM file are the same, only the coincidence data is modified. Thereafter, dual gated LM files are imported back to the LM disk of the PET/CT scanner. Each dual gated LM file is then histogrammed to sinograms separately using the manufacturer's unlisting programs and further on reconstructed to PET images applying the standard iterative OSEM-based reconstruction algorith. The whole workflow of the dual gating procedure are illustrated in Figure 11.

Table 2. Definition of dual gating phases for cardiac PET imaging: Three constant-width amplitude based respiratory gates and four partly variable time-based ECG gates.

	Respiratory gating		Cardiac contraction gating	
Dual gate	Phase	Amplitude threshold	Phase	Length
G1	R1	> 75%	1: Rapid ventricular ejection	50 ms – 130 ms
G2	R1	> 75%	2: Isovolumetric phase	130 ms – 420 ms
G3	R1	> 75%	3: Rapid ventricular filling	420 ms – 550 ms
G4	R1	> 75%	4: Late diastole	550 ms – next 50 ms
G5	R2	25% – 75%	1: Rapid ventricular ejection	50 ms – 130 ms
….	…	…	…	…
G9	R3	< 25%	1: Rapid ventricular ejection	50 ms – 130 ms
G10	R3	< 25%	2: Isovolumetric phase	130 ms – 420 ms
G11	R3	< 25%	3: Rapid ventricular filling	420 ms – 550 ms
G12	R3	< 25%	4: Late diastole	550 ms – next 50 ms

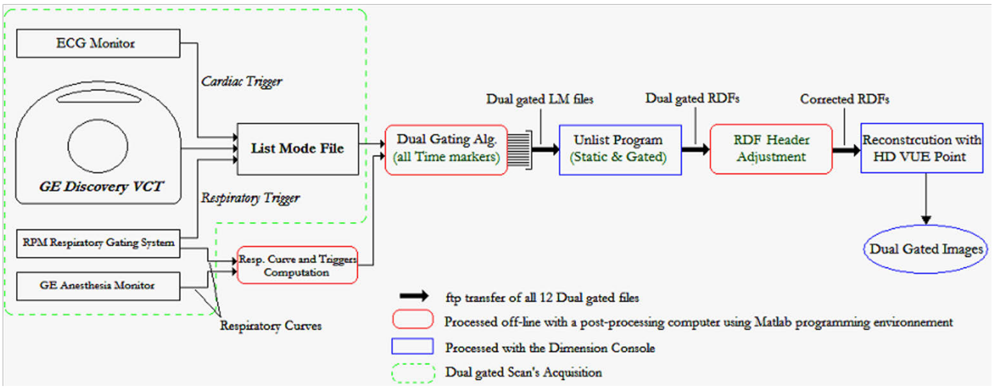

Figure 11. Illustration of the workflow of the dual gating procedure in cardiac PET imaging.

4.4.2 Data quantitation in dual gated cardiac PET

Due to above described dual gating post-processing the time spent into each dual gated LM file is different than the original scan time. To maintain dual-gated PET image quantification the actual scan time of the dual gated LM file needed to calculate and some additional RDF header parameters had to be investigated, tested and corrected.

During the unlisting process of LM emission data file the RDF of the scan is simultaneously processed to include information from RDF header parameters obtained during the scan. Attributes such as scan length (=BinDuration) and Events Lost are stored in the header information of the RDF during the scan and are used during the unlisting process. When the post-processed dual gated LM data files are unlisted using this scanner’s standard protocol the original RDF of the scan has incorrect header information for all the dual gated data files. Thus the RDF header information for the time duration and lost coincidence events were needed to correct for each dual gated data files separately before the unlisting processes. To do this an additional algorithm for correcting the RDF header information was developed using MATLAB programming environment (MathWorks, Inc.). The correct acquisition times for each dual gated data files were achieved from the calculations of the dual gating algorithm. This work was done collaboration with Nicolas Durand-Schaefer and GE Healthcare, and is presented in detail by Durand-Schaefer master thesis (Durand-Schaefer, 2008). This quantification process of dual gating method was tested with a NEMA Image Quality phantom in study II (see section 4.7).

4.5 Dual gated 2D-phantom PET study (Public. I)

In study I two self-constructed phantoms were used to test the capability of the dual gating method in simulated small target cardiac PET imaging. First the feasibility of the dual gated PET/CT method was tested with a 2D-phantom mimicking respiratory and cardiac motions (Figure 12).

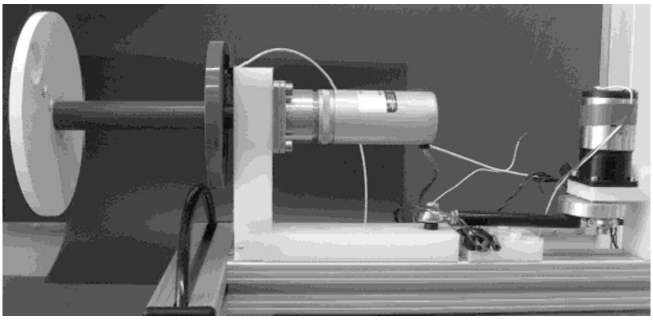

Figure 12. Photograph of the 2D-phantom. On the left is rotating and axially moving disk where the radioactive source is attached.

The 2D-phantom consists of a solid disc that rotates on a constant velocity and moves axially back and forth. Directions of these motions are orthogonal to each other and both motions are periodical. The axial displacement of the disc, frequencies of both motions, and radial position of the imaged target on the disc are partly adjustable. Both motions generate synchronized trigger signals at certain point of each motion period. These trigger signals are launched by magnetic and mechanical sensors. This 2D-phantom is able to connect to the GE Discovery VCT PET/CT scanner with the two separate trigger inputs.

In the 2D phantom study the radius of circular motion was set at 30 mm from the centre of the disk and motion amplitude of axial displacement was set at 20 mm. Cylindrical shape (3 mm diameter and 5 mm height) of radioactive source of ^{11}C was attached to 30 mm from the centre of the rotating disk. Frequencies of ECG and respiratory motions were set to 54 cycles/min and 17 cycles/min.

A normal static CTAC-scan and a 5-min dual gated emission scan were acquired. The thresholds of cardiac and respiratory phases were chosen to obtain the same size of cardiac and respiratory motions for all phases. Parameters of the DG-algorithm were adjusted so that for the circular motion four time-based constant-width phases were used, because circular velocity was constant. Whereas for the axial motion three amplitude-based variable-width phases were used, because the velocity of axial motion was partly position dependent.

Post-processing of dual gated PET LM data was done according to presented DG-method in section 4.4 without quantitative corrections to the raw PET data files. All PET images were reconstructed using an iterative OSEM reconstruction algorithm with a 256 x 256 matrix size, the axial field of view 50 cm, two iterations and 28 subsets. This resulted to the voxel size of $2.0 \times 2.0 \times 3.27$ mm^3 (13 μL).

Performance of the DG-algorithm was analysed so that the number of active time events and number of coincidence events in each dual gated LM file was counted. Active time events were those when coincidence events were present in dual gated LM file. The number of time events was counted by the algorithm and the number of coincidence events was counted by the manufacturer's software after unlisting of dual gated LM data.

4.6 Dual gated dynamic heart phantom PET study (Public. I)

After successful 2D-phantom study a dynamic heart phantom with motions mimicking realistic respiratory and cardiac motions was constructed (Figure 13 and 14) (Sipila et al., 2007) to test the DG-method's capability to improve artificial coronary plaque detection in the second part of the study I.

4.6.1 Dynamic heart phantom technical characteristics

Volume of left ventricular chamber, ejection fraction, myocardium thickness, diameters of coronaries and size of coronary plaques on the surface of myocardium were chosen to mimic real values of the human heart. Our heart phantom consists of two rubber balloons, with diameters of ca. 50 and 80 mm leading to wall distance of 10-15 mm mimicking myocardial wall of the left ventricle. Coronary vessels were modelled using silicon tubes, with inner diameters ranging from 1 to 3.5 mm, fixed on the surface of the myocardium with a tubular elastic net bandage, and four artificial coronary plaques (porous aluminium oxide balls, diameter from 1 to 3 mm) were attached in the pockets on the artificial coronary arteries (Figure 13). Contraction motion was simulated by a pneumatic pump (Figure 14). The relay was included in the power circuit to delay the contraction of the heart phantom during the diastolic phase. ECG trigger was launched by magnetic sensor at the beginning of contraction of the ventricle referring the beginning of systole. Respiratory motion was simulated by axially moving the box inside of which the heart was fixed. Respiratory motion was connected with IR-reflective block to the RPM system. The box was filled with water to have more realistic attenuation and scatter conditions.

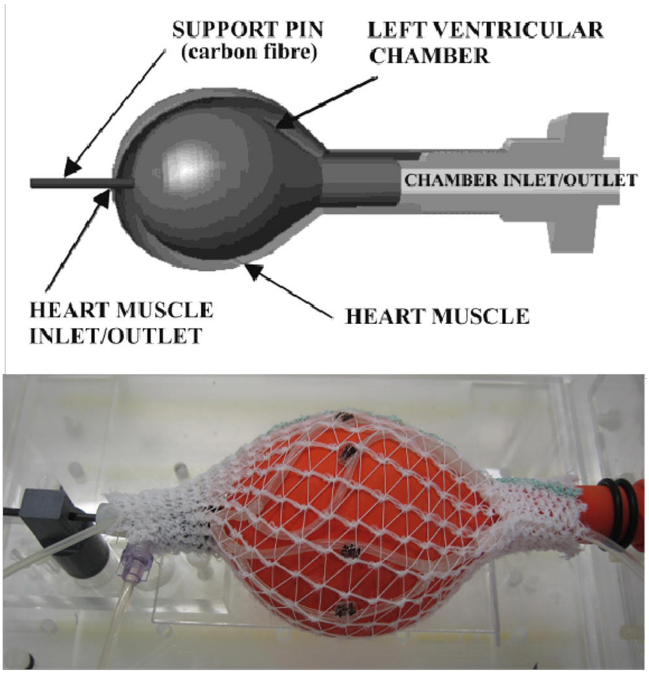

Figure 13. Up: Structure of dynamic heart phantom. Below: Image of dynamic heart phantom. Black pockets are vulnerable coronary plaque positions.

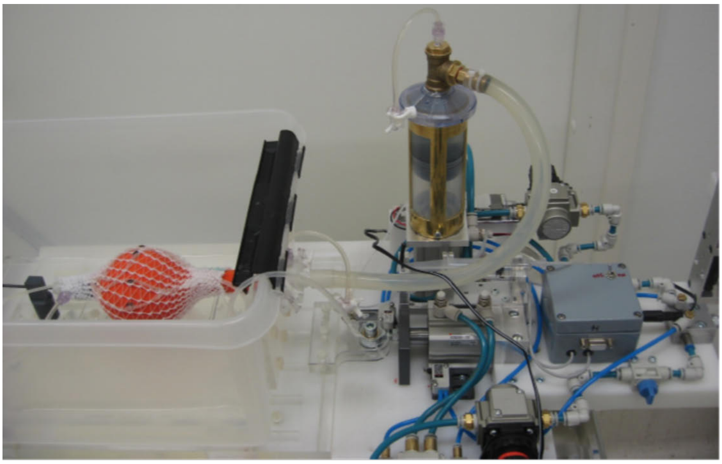

Figure 14. Structure of the heart phantom. Pneumatic pump that induces contraction motion of myocardium in the plastic box that is axially moved by the electric motor.

4.6.2 Study setup and imaging protocol

Coronaries, myocardium, and ventricle were filled with concentrations of radioactive 18F-FDG and CT contrast agent that mimicked real myocardial 18F-

FDG PET and coronary CTA imaging protocols. In addition, the porous plaques were infiltrated with the variable activity of 18F-FDG so that relation between plaque and surrounding heart activity varied around from 600 to 6000. The concentration ratios between different compartments were chosen to mimic assumed radioisotope tracer ratios in real heart if optimal plaque spesific tracer could be achievable. The radioactivity of each plaque was measured with a cross-calibrated well counter (Ortec, USA). The activity of plaques ranged from 1 to 6 kBq and with the plaque volume of around 10 to 15 µl. The box where heart phantom was placed was filled with water to have more realistic attenuation and scatter conditions. Pumping rate and time of diastole (delay of contraction) were set to 51 bpm and 400 ms, respectively. Respiratory rate was set to 19 cycles/min.

Imaging protocol was the following: the RPM driven respiratory gated 4D-CT with dual motions to get phase-matched respiratory gated CTAC for dual gated PET images, 30-min dual gated PET LM acquisition, Static CTAC without phantom motions, 5-min PET acquisition in static mode without phantom motions.

4.6.3 Data processing and image reconstruction

Post-processing of dual gated PET LM data was done according to presented DG-method in section 4.4 without quantitative corrections for the raw PET data files. Parameters of the algorithm were adjusted so that the cardiac contraction was divided to four time-based variable-width and respiratory motion to three amplitude-based constant-width phases mimicking the dual gated cardiac PET study protocol (Figure 10). The length of all three systolic phases was chosen to be 260 ms meaning that the time of diastolic phase was close to the contraction delay time. The choice of respiration gating parameters was aimed to include same amount of the respiratory motion into each respiratory phase.

All PET images were reconstructed using an iterative OSEM reconstruction algorithm with a 256 × 256 matrix size, the axial field of view 50 cm, two iterations and 28 subsets. This resulted to the voxel size of 2.0 × 2.0 × 3.27 mm^3 (13 µL).

Respiratory gated CT images were used for CTAC of corresponding emission data files when reconstructing dual gated PET images. Using the manufacturer's post-processing method together with acquired RPM signal the 4D-CT data was divided to five CTAC images which corresponded to the five time-based constant-width respiratory phases of the RPM signal (Nehmeh, et al., 2004). CTAC images from time gated respiratory phases 1 to 3 were coupled with the amplitude gated respiratory phases R1 to R3 of dual gated emission data, respectively, and further used for attenuation corrections of dual gated PET sinograms. This approach assumes that dynamic phantom respiratory motion, and thus RPM signal, resembles sine wave and is regular enough so that chosen approach for the AC phases matches well with the PET phases.

4.6.4 Analysing methods

Analyses of all plaques were done for each dual gated image, non-gated image, and image from the scan without motions. Motion analyses of the plaque in the voxel space (voxel size 2.0 × 2.0 × 3.27 mm^3) was performed by selecting the voxel of plaque with a maximum activity, and by analyzing the values of adjacent voxels in axial, sagittal, and coronal directions resulting the three orthogonal activity profiles of the plaque. Parabolic fit over the centre points of maximum and two adjacent voxels were used to determine the maximum activity and position of the peak.

Recovery coeffient values (RCs) were determined for each plaque dividing measured maximum activity value of plaque with true plaque activity value. Percent recovery coefficient values (RC%) were determined for each plaque dividing mean maximum activity value of plaque over all dual gates with the maximum activity value of non moving plaque. The width of the plaque was also measured in every orthogonal direction by determining the intersection points between the horizontal line at half maximum and lines, which were drawn between the centre points of adjacent voxels at the both sides of the half maximum value. The distance between these intersection points was defined as a full width at half maximum (FWHM) for the plaque in every orthogonal direction.

The measurements of image analyzing were performed using the manufacturer's standard image processing tools at the workstation together with self programmed algorithms in the MatLab programming environment (MathWorks, Inc.).

4.7 NEMA phantom study (Public II)

In study II a NEMA 2001 image quality phantom, which simulates the body with non-uniform attenuation, was used to verify that data post-processing during dual gating procedure does not alter the quantification of PET images.

4.7.1 Study setup and imaging protocol

The NEMA phantom without any actual motions was imaged in static PET mode and in dual-gated PET mode to ensure that images were not affected by misregistration between CTAC and emission data. Inside the phantom, three spheres with diameters of 10, 17, and 28 mm was used. The spheres were filled with a radioactive solution of 18F-FDG with an activity concentration of 35.5 kBq/ml. A standard CTAC scan acquired for AC was followed by a 7-min static and a 7-min dual-gated emission scan. Static scan was acquired to get static image reconstructions with acquisition times matching with the individual dual gate image reconstruction in order to compare dual-gated parameters with the static reference parameters. In dual gated scan trigger events for ECG and respiratory motions were simulated. The cardiac triggers were simulated using the IVY 3150-B ECG monitor (IVY Biomedical Systems, USA) in a test mode at a heart rate of 65 bpm. The simulated respiratory motion was mimicked with a device that produces a cyclic respiratory-like motion of the reflectors' box for the RPM. This generated respiratory motion of the box was followed with the RPM device. Both simulated triggers were sent to the scanner LM data stream as in normal dual gated PET studies.

4.7.2 Data processing and image reconstruction

The phantom data that was acquired in the static PET mode was reconstructed using the scanners' standard unlisting protocol by applying the matching acquisition times with individual dual gated image reconstructions. The dual gated phantom data was post-processed and reconstructed using our quantitative dual-gating protocol. The parameters of the DG-algorithm were adjusted so that 4 time-based variable-width cardiac and 3 amplitude based constant-width respiratory gates were used as presented in Figure 10. This produced 12 dual gated images, which each of contained different amount of emission data according to their dual gated acquisition time lengths. In addition, manufacturer's time based constant-width respiratory gating unlisting process was also applied to dual gated LM data to get validated reference respiratory gated PET images for SNR analysis comparision.

All static, respiratory gated and dual gated PET images, with and without RDF parameter corrections, were reconstructed with the 3D-OSEM reconstruction method with (two iterations, 28 subsets) to a 128 × 128 matrix and 35-cm field of view (FOV) with 47 slices. Slice thickness was 3.27 mm, which gives a voxel volume of 24.5 mm^3 (i.e. 24.5 µl). During reconstruction, all standard corrections were performed.

4.7.3 Analysing methods

The image-quality parameters referring to data scatter fraction, dead-time, and decay correction factors were measured for reconstructions of the static and the dual gated modes. If these factors remained unchanged during dual gating process the validity of the quantitation preserved correction for RDF was proven.

The evolution of the signal-to-noise ratio (SNR) as a function of the acquisition time was also analyzed. All three spheres were analyzed in each static, respiratory gated and dual gated image using a standard VOI analyzing method that computes the maximum value, the mean value, and the standard deviation of the activity concentration within the volume. The evolution of SNR was compared to different dual-gated frame lengths to see the effect of statistics in image quality. The activity and SNR values within the spheres derived from static and respiratory gated scans were compared to corresponding dual-gated frame lengths to see if the RDF parameter corrected dual gating process preserves the statistics.

4.8 Dual gated minipig cardiac PET study (Public. II)

The idea of the minipig study was to study if the small radioactive point source which is artificially positioned in the coronary artery of the minipig is detectable with current generation PET/CT scanner and what is the effect of the gating methods in the image quality parameters and how the background activity affect on the detection accuracy of the point source. The project was approved by Ethical committee for animal studies (1606/06).

4.8.1 Study setup and imaging protocol

In minipig study (Study II) eight 30 – 40 kg weighted minipigs were included into the study. Before the study the minipigs were anesthetized using ketamine and pancuronium, tracheostomized by surgeon and ventilated using common clinical respirator that was connected with clinical spirometer to follow the exchange of respiratory gases. The subclavian artery of minipig was also prepared in sight by surgeon. The clinical angiographic coronary catheter (5F) was prepared so that the radioactive source of known activity was inserted in small hole (2 mm length and 1 mm width and depth) of the tip of the catheter. The tip of the catheter was sealed and the activity of the catheter was measured in the cross-calibrated well-counter (3” × 3” NaI crystal) and was around 6 kBq in the volume of 2 µl. In angiographic laboratory the radioactive catheter was inserted by cardiologist through the prepared subclavian artery inside the coronary artery of the minipig so that the tip of the catheter was positioned in the main branch of the left or right coronary artery and the other end of the catheter was stitched on the skin of the minipig. This fixing procedure was done to prevent the tip of the catheter to slide out from the coronary artery. After fixing procedure the position of the tip of the catheter inside the coronary artery was confirmed with the fluoroscopic angiographic imaging by cardiologist. The workflow of the performed minipig study is illustrated in Figure 15. First CTA scan was performed using step-and-shoot cine protocol, Thereafter static CTAC scan (100 kV, 80 mA) was done during breath-hold (i.e. respirator was turned off). Length of the dual gated PET scan was 15-min, and intravenous (iv.)

18F-FDG radioactivity dose was around 50 MBq before second PET scan. Standard ECG monitor was used for cardiac monitoring and ECG gating. The RPM device was used for respiratory signal acquisition and for respiratory gated phase-matched dynamic CT scans (120 kV, 30 mA) for AC of gated PET (see details in section 4.6.3).

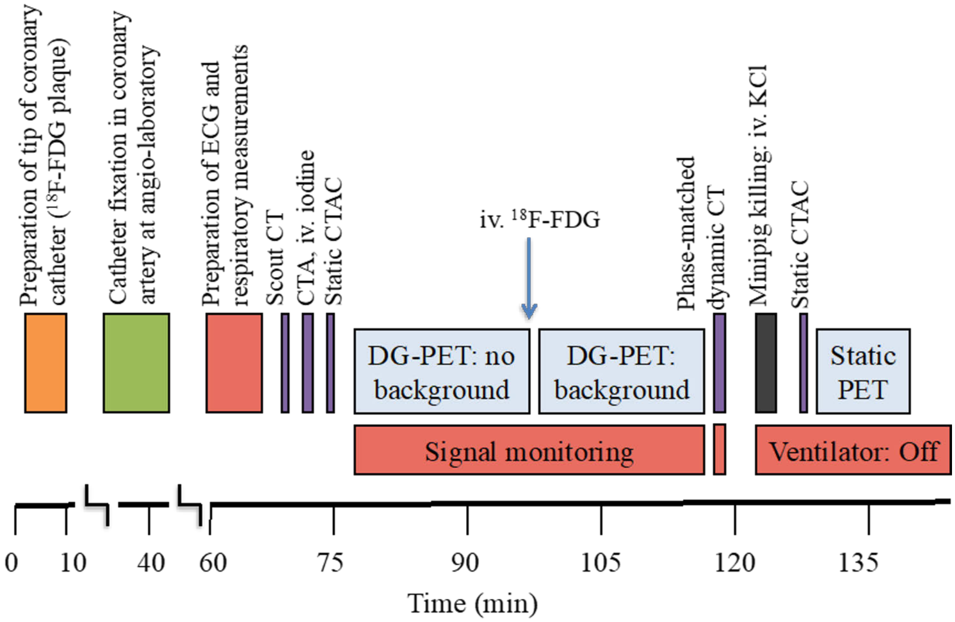

Figure 15. The workflow of the minipig study.

4.8.2 Data processing and image reconstruction

Post-processing of dual gated PET LM data was done together with quantitative corrections in the RDF files. Parameters of the algorithm were adjusted so that 4 time-based cardiac and 3 amplitude based constant-width respiratory gates were used as presented Figure 10 and Table 2. All PET images were reconstructed with the 3D-OSEM reconstruction method with (two iterations, 28 subsets) to a 128 × 128 matrix and 35-cm field of view (FOV). With a slice thickness of 3.27 mm, this gives a voxel volume of 24.5 µl (Study II, III, IV).

4.8.3 Analysing methods

Activity profiles together with FHWM for artificial coronary plaque were determined for all reconstructed image sets. The maximum activity values of the artificial coronary plaque from all reconstructed image sets were determined using maximum voxel analyzing method. Displacements of the artificial coronary plaque (i.e. maximum voxel) positions due to respiratory and/or contraction motions were measured for gated image sets. The plaque reference displacements due to contraction and respiratory motions were estimated by measuring the movement of the tip of the catheter from planar fluoroscopic angiogram images. TBR values for the different image sets were determined by comparing the measured maximum activity value of the plaque with the background activity values that where measured from both LCA and RCA myocardium territories.

The measurements of image analyzing were performed using the manufacturer's standard image processing tools at the workstation together with self programmed algorithms in the MatLab programming environment (MathWorks, Inc.).

4.9 Clinical cardiac PET/CT study (Public. II)

Coronary artery disease and suspected cardiac sarcoidosis patients were recruited to evaluate the efficacy of cardiac DG-method to detect smaller cardiac structures than usual in clinical non-gated cardiac PET/CT imaging.

4.9.1 Cardiac PET/CT setups

The feasibility of dual gated cardiac PET/CT imaging with 18F-FDG in clinical situation was tested for six patients in two patient groups. Two patients had a suspected cardiac sarcoidosis and four patients had CAD, where the inclusion criteria was unstable angina pectoris or small NSTEMI (non-ST elevation myocardial infarction) that was stabilized within 2 days.

Before the study all patients had 10 to 12 hour fasting state. In patients with sarcoidosis, no other means for reducing the tracer myocardial uptake were used. For the CAD patients, two additional methods were used to suppress the myocardial 18F-FDG uptake in order to better distinguish possible vulnerable coronary plaques. In the first method, 20% Lipovenös (Kabi Vitrum, Uppsala, Sweden) intralipid iv-infusion was started to administer 1 hour before the tracer injection and was continued over the whole PET examination. The used infusion rate was constant 0,1 ml/min/10 kg. This Lipovenös is a safe lipid homogenous emulsion, consisting of soybean oil and glycerol, which is used as a source of energy and essentially fatty acids in patients in need of parenteral nutrition therapy. In Finland it is available with special license and could be used in PET studies. Before the 18F-FDG tracer injection (dose 330-370 MBq) first blood samples (glucose, FFA, lactate) were controlled. 100 min after the tracer injection second blood samples (FFA, lactate) were controlled. This Lipovenös method was used for two CAD patients. In the second method VHFLCPP diet one day prior to the fasting period of the study was used (Williams & Kolodny, 2008) to get low blood glucose and insulin levels, and at the same to get high free fatty acid (FFA) levels to suppress 18F-FDG accumulation in the myocardium. If patients had metformin medication it was instructed to pause 48 hours before the study. This VHFLCPP diet method was used for two CAD patients, who were instructed to keep food diary for their eating.

In same imaging setting before the dual gated cardiac PET/CT acquisition all CAD patients had additional clinical CTA scan which why according to standard clinical protocol they had also iv-administered betablocker and sublinguinal nitroglyserine spray right before the CTA scan.

4.9.2 Cardiac PET/CT imaging protocols

Imaging setup for the cardiac PET/CT is illustrated in Figure 16. Spiral clinical CTA and Static CTAC scans were performed during the breath-hold at end-inspiration. All respiratory or dual gated cardiac PET scans (from 20 to 30 min) started 120 min after injection of around 350 MBq of 18F-FDG. The RPM device was used for the respiratory gated phase-matched dynamic CT scan. For the two cardiac sarcoidosis suspected patients the imaging setup differs that is presented in Figure 16 so that the length of the dual gated PET LM acquisition was only 8-min and no additional clinical CTA or the phase-matched dynamic CT scans were performed. Cardiac rhythm of the patients during the imaging protocol was followed using standard ECG IVY 3150-B monitor (IVY Biomedical Systems, USA). The respiratory monitoring and gating was done with the RPM device. Radiation dose for the patients was 1 mSv from static CTAC, 7 mSv from clinical CTA, 6.5 mSv from 18F-FDG (350 MBq) and 6.5 mSv from cine CTAC. Clinical spiral CTA scan with retrospective ECG gating was performed only for the two CAD patients in the Study II.

4.9.3 Data processing and image reconstruction (Public. II)

All sarcoidosis-suspected and CAD patients PET data were post-processed and reconstructed using the scanners' standard time-based constant-width single channel gating protocols (i.e. either respiratory or ECG gating) and our quantitative dual-gating protocol. Post-processing of dual gated PET LM data was done together with quantitative corrections in the RDF files. Parameters of the algorithm were adjusted so that 4 time-based cardiac and 3 amplitude based constant-width respiratory gates were used as presented in Figure 10 and Table 2. Aim of this parametric choice was to get the best statistics and sensitivity to the end-expiratory diastolic phase which is the longest and during which the movement has shown to be the smallest. Overall in the CAD study non-gated, 5 time-based constant-width respiratory-gated, 12 time-based constant-width cardiac-gated, and 12 dual-gated PET images were reconstructed.

In CTA study of CAD patients the CT raw data were reconstructed with cross-sectional images at 0.4 mm intervals using routine filtered backprojection and applying retrospective ECG gating. All sarcoidosis and CAD patients' cardiac PET images were reconstructed with the 3D-OSEM reconstruction method with (two iterations, 28 subsets) to a 128 × 128 matrix and 35-cm field of view (FOV) with 47 slices. Slice thickness was 3.27 mm, which gives a voxel volume of 24.5 mm^3 (i.e. 24.5 µl). During reconstruction all corrections were applied. For respiratory and dual-gated dataset the dynamic phase-matched CTAC maps were used for AC (see details in section 4.6.3), whereas static CTAC maps were applied for non-gated and ECG-gated datasets.

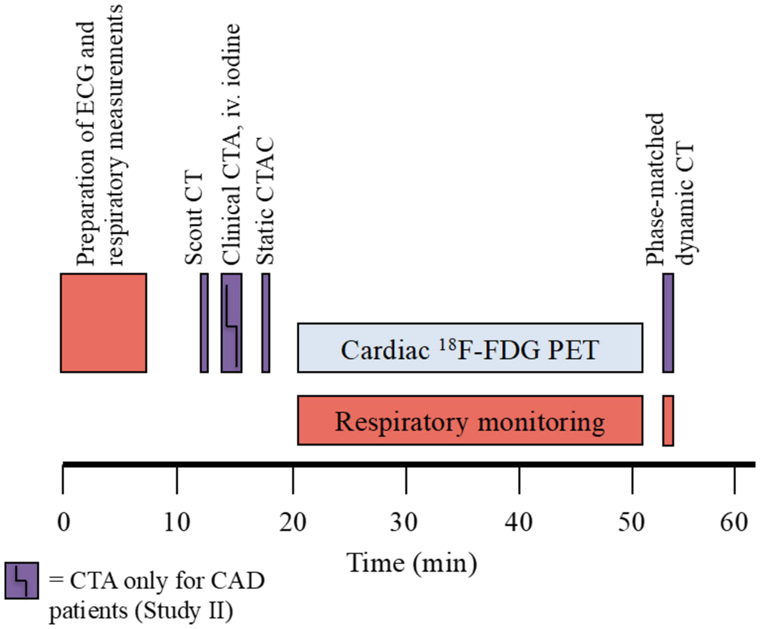

Figure 16. Imaging protocol of the cardiac PET/CT studies (Study II, III and IV).

4.9.4 Analysing methods (Public. II)

All post-processed and reconstructed PET and CT image datasets were transferred to a dedicated AW Workstation (General Electric Medical Systems, Milwaukee, USA) for further image processing using PET and CT image fusion and qualitative and quantitative analysing techniques and tools for PET image datasets.

Targets of the image analysis for suspected cardiac sarcoidosis PET/CT study:

- Is there hot and focal 18F-FDG uptake lesions visible in the myocardium that could be suspective for cardiac sarcoidosis.
- Does the gating improve the detection of the smaller details of myocardium structure as papillary muscles or hot focal 18F-FDG lesions?
- What are the maximum detected displacements of the myocardial borders due to respiratory and contraction motions?

Targets of the image analysis for CAD PET/CT study:

- What is the effect of the interventions to suppress myocardium 18F-FDG uptake?
- Is there suspective focal 18F-FDG uptake lesions in the coronary territory of the fused PET and CTA image series, that could be differentiated from the myocardium?
- What are the quantitative 18F-FDG activity values over the suspected coronary lesions, and what are the relations of the lesions activity to myocardium activity i.e. TBR-value.
- What are the differences in quantitative ROI analysis of these lesions between non-gated, gated, and dual-gated PET images.

4.10 Cardiac MR study (Public. III)

In the first part of the study III nine healthy volunteers (two female and seven male, aged from 24 to 46) were included in cardiac MRI study which studied the correlation between cardiac vessel motion amplitude and spirometric lung volume or elastic belt pressure changes at different breath-hold positions.

4.10.1 CMR study setup and imaging protocol

The overview of the performed cardiac MRI study protocol is presented in Figure 17. During cardiac MR imaging respiratory motion of the subjects was followed using the commercial spirometry device and Invivo elastic belt (see section 4.3.2). Cardiac MR imaging was performed using Philips Gyroscan Intera 1.5 T Nova Dual MRI scanner (Best, the Netherlands) and a balanced fast field echo (b-FFE) sequence. Cardiac MR images were acquired during three breath-hold tasks (inspiration, middle- expiration, and expiration) and during diastolic phase of cardiac contraction. Overall three separate MR imaging sets were performed in three orthogonal (axial, coronal, and sagittal) directions (Figure 17). Image acquisition parameters of MR scans were: repetition time/echo time (TR/TE) varied from 3.1 ms/ 1.5 ms to 3.6 ms/1.8 ms, flip angle = 60°, ECG-gating delay = 250 ms and length = 500 ms, number of signal averages = 1. The voxel size of the reconstructed images was 1.46 × 1.45 × 5 mm in sagittal and transaxial scans and 1.56 × 1.56 × 5 mm in coronal scans.

Breath-hold instructions were given to subjects immediately before each sequentially performed BH period. Instructions for the first BH task were: ‘‘inhale, exhale, inhale and hold the breath’’. Two other breathing instructions for breath-hold tasks were: ‘‘inhale, exhale, inhale, half exhale and hold the breath’’ and ‘‘inhale, exhale and hold the breath’’. A single BH period lasted from 4 to 6 seconds and each BH task consisted of 7 to 13 sequential BH periods. Altogether three MR images from three different BH levels were acquired for each subject and for each imaging direction (Figure 17). During each MRI scan both spirometry and belt signals were acquired and stored to separate files on laptop for signal post-prosessing.

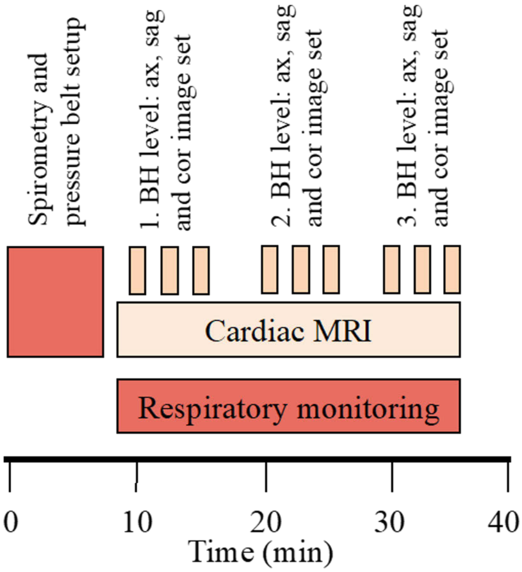

Figure 17. Imaging protocol for the cardiac MRI study. BH = breath-hold.

4.10.2 Data processing and image analysing methods

All cardiac MRI images were reconstructed using standard clinical reconstruction protocols. All cardiac MRI image datasets were transferred to a dedicated AW Workstation (General Electric Medical Systems, Milwaukee, USA) for further image processing using qualitative and quantitative analysing techniques and tools for MRI image datasets. Two experienced medical doctors analysed all cardiac MRI images. They determined visually and independently 3D coordinates of voxels where proximal end of LCA or distal end of sinus coronary (SC) vessel were localized and these voxel positions were defined as 3D positions of the vessels. 3D position of vessel that was determined during BH task of expiration was set of reference to which two other 3D positions of vessels were compared. The displacement between the 3D positions of vessel was determined as 3D motion of the vessel within the accuracy of the voxel size. 3D positions and motions of vessels were determined for all three imaging direction separately.

For all subjects during each BH task the volume and pressure signal amplitudes and BH levels (i.e. values of volume and pressure changes) were determined. Pearson's correlation and linear regression analysis were carried out between the amplitude values of three averaged BH levels and corresponding LCA or SC motions over the subjects. Residual s of linear regression fit were used to estimate the mean values and ranges of LCA and SC motion estimation errors. The equations showing the linear dependences between the amplitude values of respiratory signals and the LCA or SC motion estimations were derived using a least squares fitting. The BH task of inspirium was used to determine mean value and range of both signal amplitudes and mean value and range of motion of LCA and SC vessels over the analyzed subjects. For each BH task consistence of sequential BH periods was also evaluated. Range of BH values during each BH task was determined and the value that was at most 25% of the signal value was allowed, otherwise the data of that task was not included into analysis.

4.11 Respiratory gated cardiac PET studies (Public. III and IV)

After cardiac MR study showed that spirometer based lung volume signal correlated better than belt derived respiratory signal with coronary vessel motions (see section 4.10) the performance of the lung volume signal in the respiratory gated cardiac PET study was evaluated. During this respiratory gated cardiac PET study we noticed that the applied commercial spirometer device had an extra in-build option that enabled to filter the thoracic impedance signal out of the standard 3-lead ECG signal. The ongoing respiratory gated cardiac PET study continued the way that also the thoracic impedance signal was acquired and applied as respiratory gating signal parallel to the volume signal. The aim of this study was to find out the performance of these respiratory gating methods to detect and minimize the respiratory induced cardiac motion in clinical PET imaging.

4.11.1 Respiratory gated cardiac PET setup

The respiratory gated cardiac PET study started after the pilot coronary plaque study (see section 4.9) ended. The recruiment of CAD patients were continued to a main coronary plaque PET study, which is not part of this PhD thesis. However, suitable CAD patients from this main coronary plaque PET study were in tandem recruited to this parallel respiratory gating study. Nine parallel recruited CAD patients were included in the study protocol where correlation between spirometry derived lung volume change and center of myocardium 18F-FDG activity (CMA) motion in cardiac PET was investigated (Public III). Similarly seven CAD patients were recruited and included in the study protocol were additional 3-lead ECG based thoracic impedance signal was acquired and used for respiratory gating, and compared with the lung volume signal based respiratory gating (Public IV). In both studies cardiac rhythm of the patients was followed during the PET/CT scans using the standard ECG monitor IVY 3150-B (IVY Biomedical Systems, USA). Study setup and imaging protocol were similar with the pilot coronary plaque study (see section 4.9.2 and Figure 16).

4.11.2 Data processing and image reconstruction

Amplitude-based gating method with constant-width gates was chosen for respiratory gating to ensure the same amount of motion in each gate that was important for the objective of the PET studies. Because the method of constant-width amplitude gates was chosen, the time interval and also the statistics of each gate can vary. With the used PET scanner, data of around 3.0 minutes should be included in each cardiac PET image to ensure optimal image quality (Brown et al., 2010). The number of gates was chosen to be five to fulfill the requirements of image quality and to detect most of the CMA motion. Respiratory gated CTAC images were reconstructed from Cine-CT-images applying five equally length time based gates for RPM signal. This choice allowed to get well enough matching CT attenuation maps for volume and impedance signal gated PET images. In Figure 18 is illustrated an example of typical volume and impedance signal and the amplitude based respiratory gating approach. PET image reconstruction was done by iterative OSEM algorithm with a 35-cm axial field of view, two iterations, 28 subsets and 6-mm Gaussian post-filtering. The matrix size of reconstructed PET images was $256 \times 256 \times 47$ with voxel size of $1.37 \times 1.37 \times 3.27$ mm.

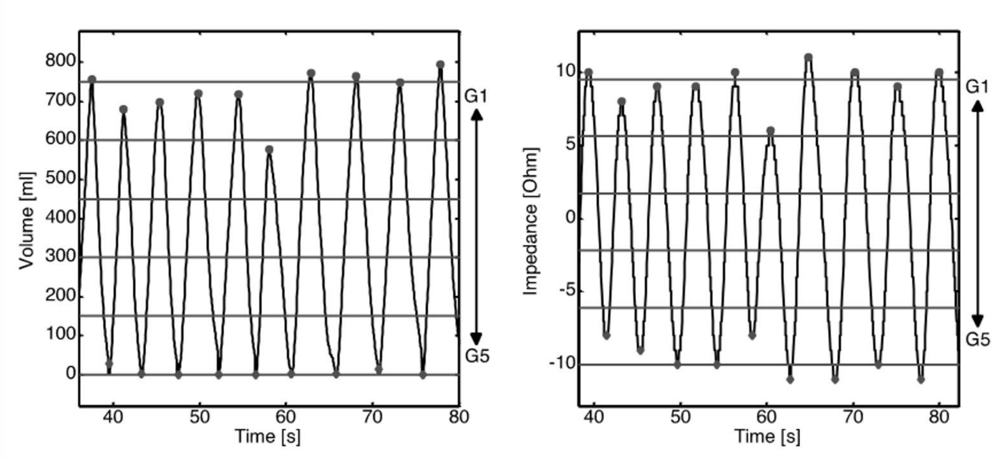

Figure 18. An example of a typical lung volume (on the left) and impedance (on the right) signal and the description of five constant-width amplitude-based gating method in the respiratory gated human cardiac PET study.

4.11.3 Gated PET image and signal analysis

The voxels of myocardium 18F-FDG uptake in non-gated PET image were segmented using a 150-mL volume covering the dimensions of 5.5 × 5.5 × 8 cm. This volume template was used to determine the CMA from the five respiratory gated cardiac PET images. Motion of CMA was determined between two outermost respiratory gated (G1 and G5) PET images, because those reflect to the maximum respiratory induced motion of myocardium and correspond to the definition of the gating amplitude. All three respiratory signals (RPM, volume and impedance) were post-processed and analysed. Correlation and linear regression analysis between the gating amplitudes of volume or impedance signals and the corresponding CMA motions were carried out. Pairwise correlation analysis for signal amplitudes and signal respiratory cycle times were performed between the three respiratory signals. The mean difference and correlation analysis between the two, volume or impedance signal based, subsets of the maximal CMA motions were calculated. Correlation analysis between the gating amplitudes of the volume and impedance signals, and corresponding maximal CMA motions were also performed. All signal processing and data analysis were done using MATLAB programming environment (MathWorks, Inc.).

4.12 Statistical analysing methods

In studies III and IV correlation analysis was performed using Matlab's Pearson's correlation function. The following grading was used for the correlation coefficient

(CC): excellent (|r| ≥ 0.99), very good (0.99 > |r| ≥ 0.95), good (0.95 > |r| ≥ 0.90), moderate (0.90 > |r| ≥ 0.70), mild (0.70 > |r| ≥ 0.40), and weak (0.40 > |r| ≥ 0). Linear regression analysis was based on Matlab's polynomial fitting function that finds the coefficients of a polynomial f of degree n that fits the data f(x) to y in the least square sense without weighting. The degree of fitted polynomial was one. The wellness of fitting function f was evaluated by calculating the mean and maximum estimation error between the estimated and the measured motion values.

5 Results

5.1 2D-phantom, dynamic heart phantom and NEMA phantom studies (Public. I and II)

2D phantom study (Study I) showed that the reconstructed DG-method preserves the original LM data and divides the motion of radioactive target correctly to 12 spatially different segments with well-defined borders on the cylindrical surface (Figure 19, images on left).

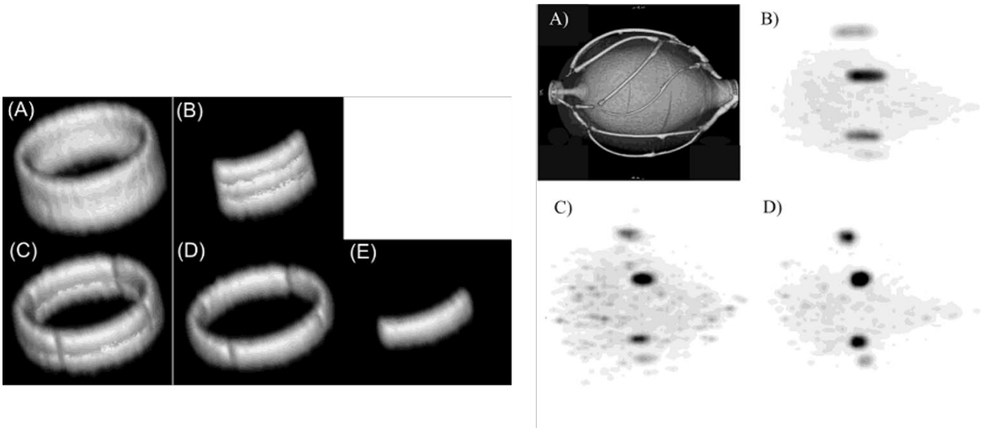

Figure 19. On left is dual gated PET images from the 2D phantom study (Study I): (A) Non-gated, (B) three fused dual gated, (C) eight fused dual gated, (D) four fused dual gated and (E) a single dual gated PET images. Image B illustrates cardiac gated only and image D illustrates respiratory gated only situation. On right is images from the dynamic heart phantom study (Study I): (A) a 3D illustration of CTA image, (B) non-gated PET image, (C) dual-gated PET image, and (D) no-motion PET image.

The dynamic heart phantom study (Study I) showed that the reconstructed phantom simulate well enough the structure, measurements and motions of left ventricle, myocardium and coronaries in PET (Figure 19, images on right). The dynamic hearth phantom cardiac contraction and respiratory motion patterns simulated well enough realistic heart movements. Results from the analysis of the 6 kBq coronary plaque is presented in Table 3 and Figure 20. Dual gated PET images of dynamic heart phantom showed 51% reduction of contraction motion (true motion 7 mm) and 70% reduction of respiratory motion (true motion 20 mm) for the 6 kBq active spherical (3 mm diameter) plaque when maximum voxel analysis was used. Detected average SUVmax of 6 kBq plaque over all 12 dual gated images improved 89% when compared to non-gated images (Table 3). FWHM values of the activity profiles of the hot plaques were almost restored with dual gating when compared to activity profiles derived from the static (i.e no motion) heart phantom PET scan. Thus in dual gated PET images the maximum activity value of the 6 kBq plaque was 80% from the maximum value of the static scan. However, for all studies and reconstructions the obtained maximum activities for plaques were only a fraction of true activities of the plaques due to PVE. The measured recovery coefficient values for plaques were around 0.03 for both dual gated or no motion images.

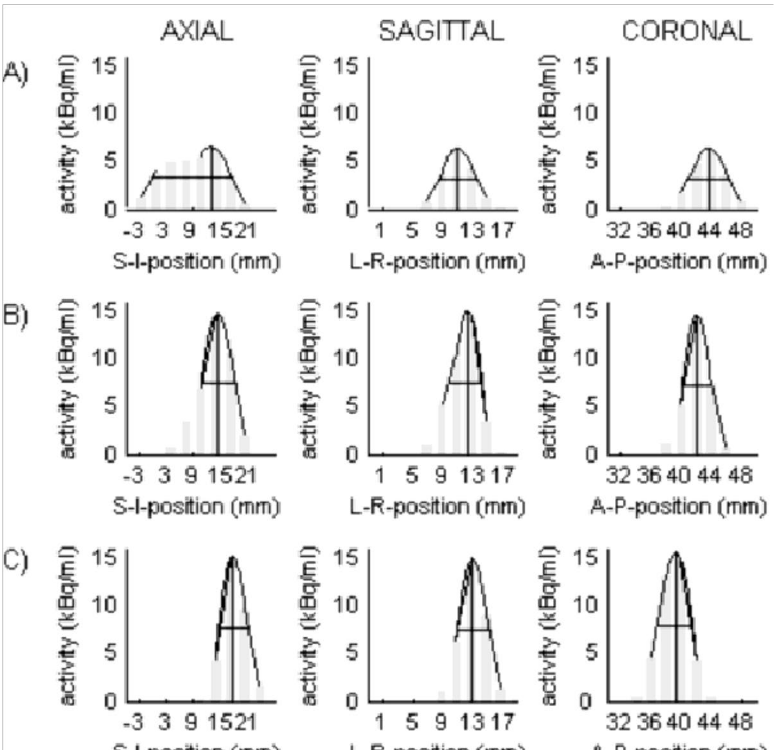

Figure 20. Activity profiles of the 6 kBq plaque from the PET images of the dynamic heart phantom study (Study I): (A) Non-gated, (B) Dual gated, and (C) No motion gating options. Qualitatively activity profiles from the dual gated image do not differ much from the profile from no motion image.

Table3. PET image analysis of the 6 kBq coronary plaque (diameter around 3 mm, and activity concentration around 450 kBq/ml) in the dynamic heart phantom study (Study I) with different gating options.

PET image type	Maximum plaque activity (kBq/ml):	Percent recovery: RC%	Recovery coefficient: RC	FWHM: Axial (mm)	FWHM: Sagittal (mm)	FWHM: Coronal (mm)
Non-gated	6.5	0.43	0.01	17.8	5.1	5.4
ECG gated	9.5 ± 1.1	0.63	0.02	13.9 ± 3.3	3.9 ± 0.7	4.0 ± 0.8
Resp gated	13.1 ± 2.9	0.86	0.03	7.9 ± 1.3	5.5 ± 0.5	5.3 ± 0.3
Dual gated	12.2 ± 1.9	0.80	0.03	8.6 ± 0.4	4.4 ± 0.4	3.9 ± 0.7
No motion	15.2	1.00	0.03	6.4	4.1	4.5

Table 4. NEMA phantom study (Study II). Correction factors of dual gated PET images with and without RDF parameter adjustments compared to correction factors of static PET images with different acquisition times.

	Parameters from dual gated images without RDF header adjustments			Parameters from dual gated images with RDF header adjustments			Parameters from static image reconstruction		
Time (s)	Scatter fraction factor	Dead time factor	Decay factor	Scatter fraction factor	Dead time factor	Decay factor	Scatter fraction factor	Dead time factor	Decay factor
8	na	53.13	1.0227	0.12	1.001	1.0227	0.12	1.001	1.0227
13	na	32.67	1.0227	0.13	1.001	1.0227	0.13	1.001	1.0227
18	0.99	23.87	1.0227	0.15	1.001	1.0227	0.14	1.001	1.0227
29	0.65	14.52	1.0227	0.16	1.001	1.0227	0.15	1.001	1.0227
50	0.37	8.48	1.0227	0.17	1.001	1.0227	0.16	1.001	1.0227
64	0.29	6.58	1.0227	0.17	1.001	1.0227	0.17	1.001	1.0227
111	0.23	3.80	1.0227	0.19	1.001	1.0227	0.19	1.001	1.0227
420	-	-	-	-	-	-	0.22	1.001	1.0227

NEMA phantom study (Study II) showed that RDF parameter corrections are mandatory if the DG-method is applied to cardiac PET imaging to get quantitative PET images. The study also showed that performed parameter corrections were done correctly and were sufficient. After the corrections the scatter fraction and dead-time factors for dual gated images were similar than the corresponding factors that were derived from similar time length static scan (Table 4). The mean activity concentrations within the spheres derived from the dual gated images were also comparable to the values obtained from the reference images when considering the possible spatial missregistration errors due to manually drawn VOI and the used voxel size compared to the size of the target spheres (Table 5). Also the measured SNR values for the spheres derived from dual gated images were comparable with the values derived from the static scan (Table 5).

Table 5. Image quality analysis of NEMA phantom study (Study II). Dual gated PET images maintains the quantitative activity concentration and SNR values of the target when compared to standardized non-gated and manufacturer’s own respiratory gating methods.

		Sphere 28 mm		
Gating method	Scan duration (s)	Mean (kBq/ml)	SD (kBq/ml)	SNR
Static	111	28.5	4.9	5.82
GE resp gating	105	29.2	5.2	5.62
Dual gating	111	28.6	5.0	5.72

5.2 Minipig study (Public. II)

In minipig study (Study II) five out of eight minipigs survived through whole study protocol. The catheter with the radiactive tip was fixed successfully in the proximal part of the main coronaries of the minipigs. Fluoroscopy angiogram showed that most of the catheter motion was caused by the cardiac contraction motion and only a small cranio-caudal displacement of the catheter by respiration was seen in the apical part of the heart. Similar observation was made with the RPM motion tracking device during PET scans so that detected chest wall motions of the minipigs due to the respirator were only around 1 mm in the anterior-posterior direction.

The hot and small plaques placed were visually separable from the myocardium activity in all reconstructed PET images for all succeeded minipig studies (Figure

21). Measured displacements of the plaques in end-expiration between diastole and systole was around 5 mm in superior-inferior direction and around 4 mm in anterior-posterior direction when displacements were determined between the corresponding maximum positions of the fitted activity profiles of the plaques from the dual gated cardiac PET images. Displacements on the right-left direction were negligible.

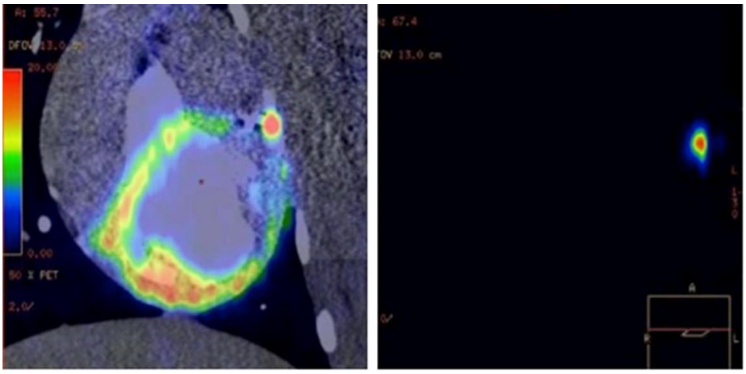

Figure 21. Minipig study (Study II). On left is fused CTA and PET images: the coronary plaque can be distinguished from the background activity. On right is PET only image: the hot coronary plaque is easily visible without background activity.

Results of the image analysis for minipig "Case 8" is presented in the Table 6. With and without background activity the maximum activity values for the plaques from dual gated PET images were very close to the corresponding values for the plaques derived from no motion scan, whereas the non-gated PET images derived much lower activity values for the plaques. The FWHM values for the plaques derived from the dual gated PET images were almost the same as the corresponding values derived from no motion PET images, and also very close to the FWHM values of the used PET scanner (Teräs et al., 2007). In one successful minipig case the maximum voxel activity value of the plaque derived from diastolic dual-gated PET image increased 107% when compared to the corresponding value derived from the non-gated PET image, and was 99% of the corresponding value derived from the killed non-moving PET image. One representative minipig case showed that the measured target-to-background ratio (TBR) between the manual VOI-analysis over the plaque and the myocardium increased 87% between non-gated and the best dual-gated PET image derived values, and for the same best dual-gated image this TBR value was 90% of the corresponding value derived from the killed no-motion PET image. Overall the best correlation values between maximum activity values, TBR values and also FWHM values for the plaques were achieved when the end-expiration diastolic phase PET images were compared to the killed no-motion PET images.

Table 6. Minipig study (Study II): Results from the image analysis for minipig "Case 8". TBR = plaque activity / mean myocardium activity on RCA territory, Dg = Dual gated.

	Maximum plaque activity concentration (kBq/ml): Background		Mean myocardium activity concentration (kBq/ml)		TBR: Plaque / RCA	FWHM Axial (mm)	FWHM Sagittal (mm)	FWHM Coronal (mm)
Image type	No	Yes	LCA	RCA				
Dg 10	26.3	31.9	6.1	17.9	1.78	7.0	5.1	5.1
Dg 12	18.8	23.3	6.1	17.6	1.32	7.4	5.1	8.9
Dg av. (1–12)	22.5	28.7 ± 5.8	5.9	17.4	1.65	6.9 ± 1.0	5.3 ± 1.0	6.5 ± 1.3
Non-gated	16.6	15.4	5.7	16.2	0.95	11.0	6.7	11.2
Killed/Static	-	32.0	7.0	16.2	1.97	6.3	5.1	5.5

5.3 Dual gated clinical cardiac PET/CT (Public. II)

First cardiac patient studies (Study II) showed that the DG-protocol and algorithm worked in a clinical setting, and the patients tolerate it well. A clear improvement in spatial resolution was seen in dual gated PET images when compared to non-gated images. Indeed, the papillary muscles from the left ventricle became visible and the myocardial wall thickness was thinner and sharper in the dual-gated PET images (Figure 22). However, the image statistics showed to be somewhat poorer in the dual-gated PET images than no-gated images. DG-protocol showed that the cranio-caudal directional cardiac motion was somewhat 7 mm due to cardiac contraction and 15 mm due to respiration (Figure 22).

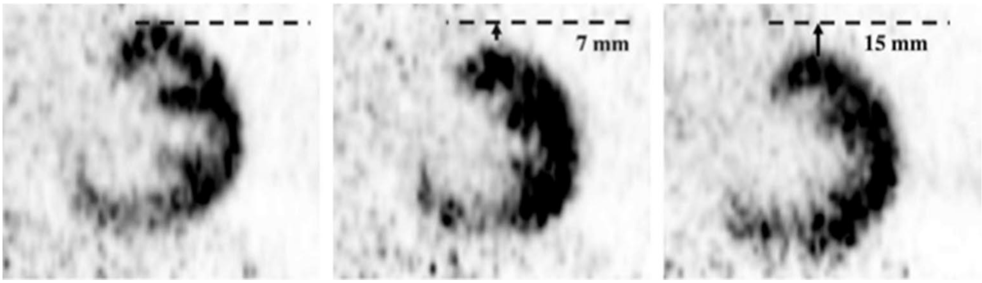

Figure 22. Dual-gated images of sarcoidosis patient's myocardium (Study II): Left: end-expiration and diastole; Middle: end-expiration and systole; Right: end-inspiration and diastole.

In CAD patient study (Study II) VHFLCPP diet reduced the 18F-FDG myocardium uptake remarkably for all four studied patients showing that if 18F-FDG is used for cardiac PET imaging to detect the inflammable vulnerable coronary plaques this diet should be carry out before the study to improve the plaque detection. In this preliminary CAD study only one of the four patients showed possible detection of vulnerable coronary plaque in proximal part of the coronary artery territory when the DG-method was applied (Figure 23). In this specific case the active 18F-FDG uptake was seen to localize in the proximal part of the LAD in the fused PET/CTA image where the diastolic end-expiratory dual gated PET image was used (Figure 23). However, in non-gated, respiratory gated or cardiac gated PET images were no active 18F-FDG accumulation to be seen in the corresponding part of the LAD vessel (Figure 23). The TBR analysis between the values of mean 18F-FDG uptake based on manual ROI drawing over the proximal part of LAD and the myocardium showed that only the dual gated PET image had the significant specific uptake on the proximal part of the LAD, and is more than twice as much as the corresponding TBR value measured from non-gated PET image (Table 7).

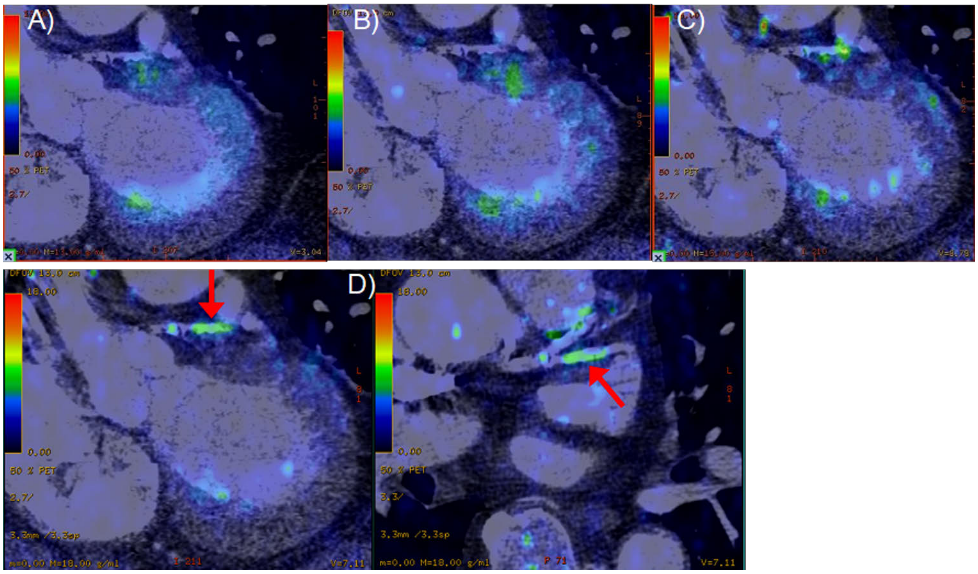

Figure 23. Human cardiac PET/CT study (Study II). Fused coronal image slices from the coronary CTA and 18F-FDG PET: A) non-gated PET-image, B) ECG-gated PET-image, C) respiratory gated PET-image. Fused coronal and axial image slices from the coronary CTA and 18F-FDG PET: D) dual gated PET-images. Only in dual gated PET-image can be distinguished the focal 18F-FDG activity over the coronary vessel (arrow).

Table 7. Human cardiac PET/CT study (Study II): Case5. Analysis of the focal coronary artery activity in proksimal LAD using different gating options. TBR = target to background ratio.

	Measured ROI activity (kBq/ml)		TBR:
PET image type	Myocardium	LAD	LAD / Myocardium
Non-gated ie. static image	4.0	3.4	0.85
GE respiratory gated	4.0	3.4	0.85
GE cardiac gated	4.2	4.6	1.10
Dual gated (dual gate12)	3.9	7.0	1.79

5.4 Cardiac MR study (Public. III)

In cardiac MR study (Study III) the spirometric mask was well tolerated by the volunteers and no discomfort about the mask was reported. The cardiac MR image quality was slightly declined due to accepted variations (4% to 23% of signal amplitude) in sequential breath-hold levels and the used non-uniform voxel size dimensions (Figure 24). The quality of spirometric volume signals were very good and no remarkable baseline variation was detected. However, slight sloping down was detectable in pressure belt signals during a breath-hold for some volunteers but no such effect was present in volume signals meaning that no airflow leakage was present (Figure 25). The correspondence of the 3D positions and displacements of the vessels in MR images between two specialists were good when considering the voxel size dimensions (see Publication III, Figure 8).

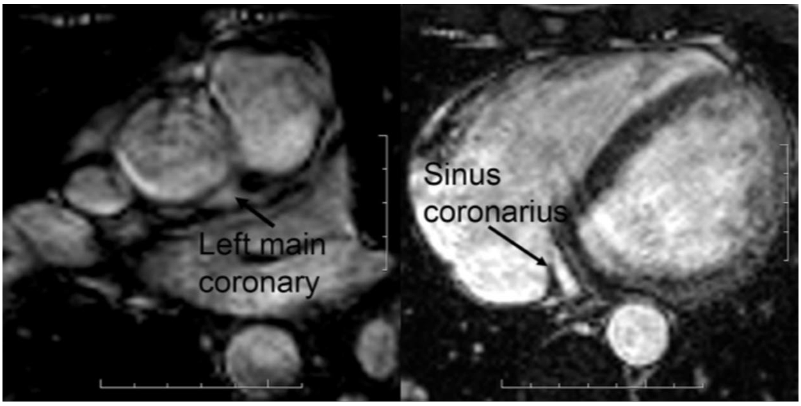

Figure 24. Axial slices of the cardiac MR images (Study III). On left: Orifice of the left main coronary. On right: drainage of the sinus coronarius.

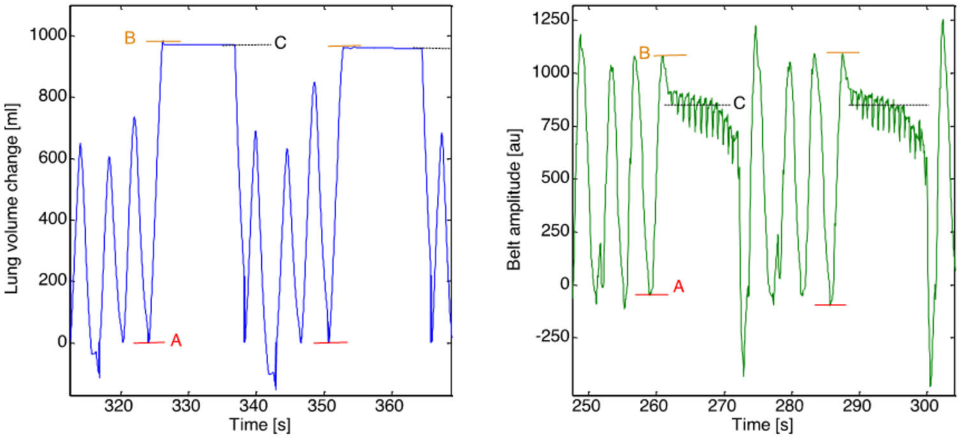

Figure 25. Cardiac MR study (Study III): Respiration monitoring signals during the two sequential end-expiration breath-hold periods. On left: lung volume signal. On right: pressure belt signal. Levels A and B determines the value of the signal amplitude for the breath-hold task. Line C presents the average value of the signal during the breath-hold.

Results from the correlation analysis between signal amplitudes and vessel motions are presented in Table 8. The changes of spirometric volume signal showed to have good correlation with both LCA and SC motions of heart whereas the changes of pressure belt signal showed to have moderate correlation with both vessel motions. The both estimated LCA and SC motions were more accurately derived by spirometric volume signal than by the elastic pressure signal. The mean estimation error for LCA and SC motions were 2.0 mm and 2.6 mm for spirometry, and 2.9 mm and 3.3 mm for belt signal respectively. Mean maximum displacement value for LCA and SC motions was very similar 14.8 mm and 16.4 mm. However, maximum displacement values varied markedly between the volunteers, for LCA from 7.7 mm to 24.0 mm and for SC from 7.1 to 24.8 mm.

Table 8. Cardiac MR study (Study III) correlation analysis. V_{spiro} and P_{belt} refer to spirometric lung volume [l] and pressure belt [au] changes. Values are calculated over three orthogonal image sets and over eight volunteers. All correlation coefficients have p-value < 0.001.

Vessel motion vs. resp. signal change	Regression slope [mm/l] or [mm/au]	Intercept of y-axis [mm]	Correlation coefficient
LCA motion vs. V_{spiro}	11.91 ± 0.73	0.94 ± 0.20	0.92 ± 0.02
SC motion vs. V_{spiro}	12.95 ± 0.62	1.13 ± 0.45	0.90 ± 0.03
LCA motion vs. P_{belt}	19.66 ± 1.28	-2.91 ± 0.59	0.86 ± 0.04
SC motion vs. P_{belt}	21.74 ± 3.07	-3.15 ± 1.32	0.84 ± 0.05

5.5 Respiratory gated cardiac PET studies (Public. III and IV)

In respiratory gated cardiac PET studies (Study III and IV) the spirometric mask was well tolerated by the CAD patients. The quality of spirometric volume signal was very good (Study III and IV) and the quality of the impedance signal fairly good (Study IV). The cycle lengths of RPM and lung volume or impedance signals were used to synchronize the signals in time. This synchronization was shown to be reliable as the correlation between the cycle lengths of the signals was excellent (Study III and IV) (Figure 26 and Figure 27 on left).

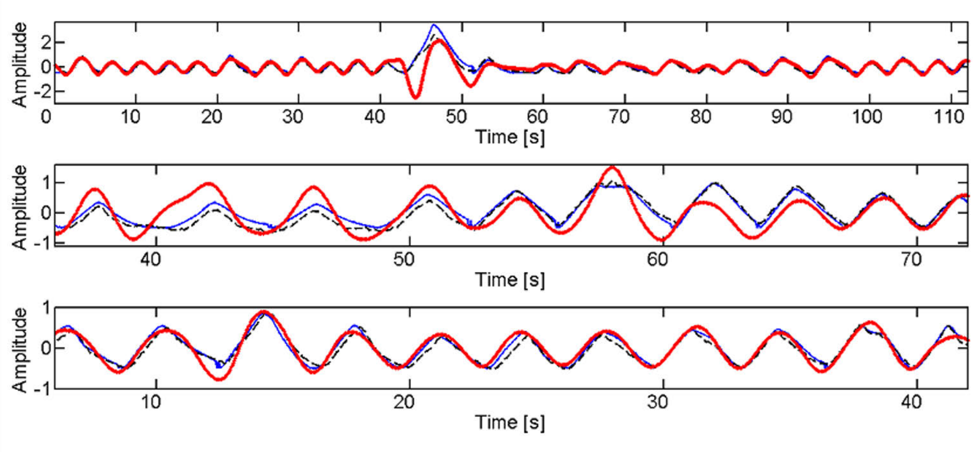

Figure 26. Respiratory gated cardiac PET (Study IV): Three representative examples of normalized respiratory signals, impedance (thick red line), lung volume (thin blue line), and RPM (dashed black line), derived from CAD patients. Top: One deep breathing cycle stands out from shallow breathing. Middle: All signals are synchronized but impedance has different amplitude values than volume and RPM. Bottom: All signals have good correlation. RPM = Real-Time Position Management signal that follows the vertical displacement of the chest.

In the Study IV the patient related volume and impedance signal respiratory cycle length correlations were from good to excellent for local maximum or minimum (Figure 27). The volume and RPM signal respiratory cycle length correlations were from very good to excellent CC values for local maximum or minimum. Normalized spirometric lung volume, RPM and impedance signal amplitudes had overall moderate to good correlation values so that correlation between volume and RPM signal amplitudes was the most accurate. For few single patients there was weak or no correlation between impedance and volume or RPM amplitudes.

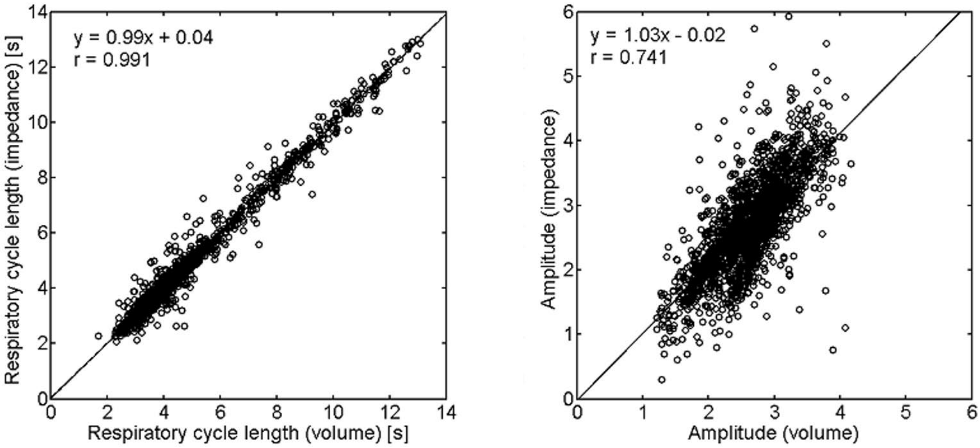

Figure 27. Respiratory gated cardiac PET (Study IV): Respiratory signal correlation between volume and impedance signals derived from CAD patients. On left: Respiratory cycle length correlation plot. On right: Signal amplitude correlation plot.

In the respiratory gated cardiac PET studies (Study III and Study IV) the applied respiratory gating methods together with choice of five respiratory gates enabled visually good PET and CTAC image quality when compared to clinical cardiac PET and CTAC image quality. Segmented myocardium structures from PET-images corresponded the clinical knowledge and experience what the myocardium structures looks like in cardiac 18F-FDG PET-images (Figure 28). A good linear dependence (CC value of 0.93, p-value < 0.001) between the spirometric volume change and the measured CMA motion was detected (Figure 29). Mean and maximum estimation errors for CMA motions based on the lung volume changes were 0.9 and 2.5 mm. More than 90% of the CMA motions were along axial direction and maximal difference between total CMA motion and axial CMA motion was less than 1.0 mm for all patients.

Figure 28. Respiratory gated cardiac PET (Study III and IV). An example of transaxial cardiac 18F-FDG PET-images after the myocardial segmentation in Study III.

Detected maximal CMA motions between volume and impedance gating methods were very close to each other having only 1.2 mm mean difference over all seven studied patients. The correlation value between these two gating methods for the maximal CMA motions was good 0.948. The CMA motion was more evenly distributed between adjacent gates for volume than impedance gating (Figure 30). There was no correlation (CC value -0.326) between the absolute value of the gating amplitudes. The correlation between absolute gating amplitudes and the maximal CMA motions was 0.937 for volume gating and -0.430 for impedance gating.

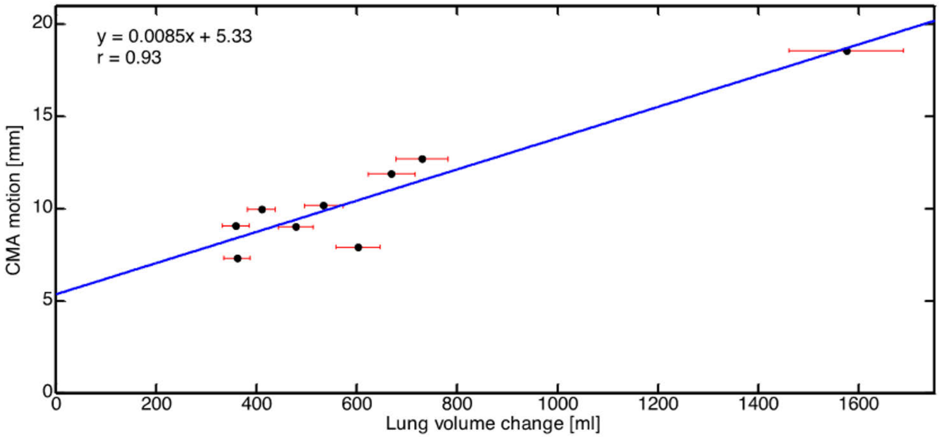

Figure 29. Respiratory gated cardiac PET (Study III): Scatter plot and linear relation between motions of center of myocardium 18F-FDG activities (CMA) and quantitative lung volume respiratory gating amplitudes.

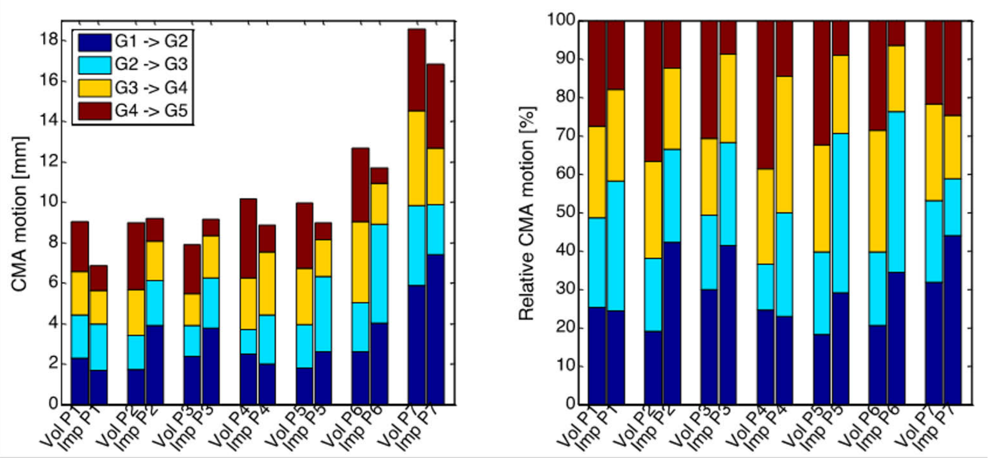

Figure 30. Respiratory gated cardiac PET (Study IV): Motions of center of myocardium 18F-FDG activities (CMA) derived from respiratory gated 18F-FDG cardiac PET. Respiratory gating was done based on lung volume (Vol) or impedance (Imp) signals. On left: absolute cardiac CMA motions and distribution between adjacent respiratory gates (G1-G5) for both gating methods. On right: percentage distribution of cardiac motions between adjacent respiratory gates for both gating methods.

6 Discussion

Traditional risk assessment of CAD has been based on patient vulnerability indexes as Framingham (Anderson et al., 1991) and PROCAM (Assmann et al., 2002) which has been shown to predict long-term outcome in large populations. To provide better clinical route to identify, treat, and prevent near future victims of ACS or sudden cardiac death focus has put on cardiovascular vulnerable patient. This means that the focus of risk patients should be on the characterisation of the vulnerable plaque, vulnerable blood and the vulnerable myocardium (Naghavi et al., 2003a, 2003b). Especially more detailed characterization of the atherosclerotic plaque could be helpful to improve risk assessment and to direct the intensive, already existing and emerging, medical treatment for the right persons to prevent plaque ruptures, and thus ACS. Imaging has an important role to assess these risk patients who have vulnerable coronary plaques prone to rupture. Due to superior sensitivity to measure the metabolic phenomenon as inflammation the noninvasive PET imaging is one of the most promising modality to assess if these risk patients have vulnerable coronary plaques prone to rupture in their coronary trees. However, major challenges in PET imaging of coronary plaques include their small size and their constant motion due to both cardiac contraction and respiration motion together with the challenge of developing vulnerable plaque specific tracer compound.

Relative few studies have been published where PET imaging has been used to identify the possible vulnerable coronary plaque detection in risk patients. The main reason for this is that it is not yet developed a tracer which specific accumulation ratio into vulnerable plaque would be so high that the relatively low spatial resolution of PET imaging could detect these less than voxel size plaques that on top of that are in constant motion. Due to long PET imaging times the inaccuracies due to cardiac and respiratory motions have been handled by applying cardiac or respiratory gating. Only few preliminary publications was known where these two gating methods were performed at the same time as DG-method. Top of that, no clinically available commercial dual gating approaches for small target, as vulnerable coronary plaque, detection was published or put on the market when this study started. Thus the aim of our study was to develop and test if the robust dual gating cardiac PET imaging method is feasible to implement in clinical conditions and using widely available commercial PET/CT scanner. The specific purpose was to improve the detection of small realistically moving cardiac targets that mimics the characteristics of vulnerable coronary plaques. Since the sensitivity was of utmost importance we aimed for DG-method with minimal loss in count statistics. We expected to exclude most of the respiratory and contraction motion and still maintain enough sensitivity for imaging of vulnerable coronary plaques.

In study I we reconstructed and performed two phantom studies from which the latest one was with the realistically moving dynamic heart phantom. In the first rotating phantom study we showed that the developed DG-algorithm is reliable to detect and separate respiratory and cardiac motion and it maintains the count statistics when it is applied to data acquired with commercial PET/CT scanner. The following dynamic heart phantom study demonstrated that the method was robust enough and feasible to improve the detection accuracy of coronary plaques in PET images.

In study II the developed DG-algorithm was successfully applied *in vivo* conditions in minipigs and in clinical human cardiac PET studies. In addition, the dual gated NEMA2001 phantom study was performed to show that by applying appropriate corrections for reconstruction parameters after the dual gating procedure, the quantification of PET images is successfully maintained.

In the first part of the study III the spirometric lung volume and elastic belt pressure respiratory signal changes showed good or moderate linear correlation with the motion of coronary vessels in cardiac MRI study that was performed during the sequential breath-hold periods. As the spirometric lung volume measurement had better correlation with coronary vessel motions it was applied as respiratory gating signal to clinical cardiac PET study. This second part of the Study III showed that spirometric lung volume change linearly estimates motion of myocardium in PET with good accuracy and have potential to guide selection of optimal number of respiratory gates in cardiac PET.

In study IV we showed that spirometric, thoracic impedance and RPM signals have very good pairwise cycle length correlation. As result of this also the impedance signal is potential to be used as a time based respiratory gating signal in gated PET imaging. Moreover in this study we showed that, even if there was no pairwise correlation between spirometric volume and impedance signal amplitudes, the both volume and impedance signal amplitude based respiratory gating methods performed almost equally well when the accuracy was measured as the detected motion of myocardium between gated PET images. Thus this commercially widely available thoracic impedance signal method is potential to be used also for dual gating where the impedance signal is frequency filtered to separate ECG part and respiratory part from the signal as Koivumäki et al have previously proposed in their study (Koivumäki et al., 2012).

6.1 Dual gated cardiac PET method

The major goal of this study was to minimize the effect of contraction motion on the myocardium and/or the plaque imaging but not to detect and analyse the maximal magnitude of cardiac contraction in PET imaging (Study I and II). Thus the number of cardiac phases was minimized and focus was put on the diastolic phase of the cardiac contraction in the developed DG-method. Due to its longest duration without significant contraction motion (Wang et al., 1999) the diastolic phase is the most important to detect, and likely the easiest and effective approach.

In all dual or respiratory gated PET studies the amplitude based respiratory gating method was applied because it was showed to detect the motion of heart more accurately than time based respiratory gating (Dawood et al., 2007). In all gated PET studies amplitude-based gating method with equal width gates was chosen to ensure the same amount of motion in each gate that was important for the objective of the PET studies. Because the method of equal width amplitude gates was chosen, the time interval and also the statistics of each gate can vary due to variable breathing patterns. With the chosen gate numbers the scan time of the gated cardiac PET studies was determined so that the acquired data of around 3.0 minutes was included in each gated cardiac PET image that was shown to ensure optimal image quality with the used PET scanner (Brown et al., 2010).

In the dual gated phantom and cardiac PET studies (Study I and II) number of respiratory gates was chosen to be three. This choice of respiratory gate number in the dual gated PET studies was based on our experience in clinical respiratory gating studies, PET scanner resolution, knowledge of coronary plaque sizes, clinically acceptable scan times and knowledge of magnitude and pattern of cardiac motion. If one needs to track the moving target more exactly, larger numbers of cardiac and respiratory gates might be needed, that unfortunately comes with the cost of lost sensitivity (Dawood et al., 2009; Klén et al., 2020). So because the aim of these dual gated studies was to maintain the sensitivity of PET images to see the plaques in every dual gate image and get rough elimination of respiratory motion the choice of three was sufficient. Park et al. have shown that optimal compromise for the spherical 10 mm target with 20 mm motion amplitude is the use of 5 temporal respiratory gates in PET imaging when respiratory motion resembles the sine wave behaviour (Park et al., 2008). In our dynamic heart phantom (Study I) and CAD patient (Study II) studies respiratory motion signals were regular enough and no signal baseline drift occurred. So the applied choice of 3 amplitude based respiratory gates, in the studies that focused on small target PET imaging, can be considered as a good choice when compared with results of Park et al.

In the Studies III and IV where the efficacy of the different respiratory gating methods in cardiac PET imaging were compared the number of respiratory gates was chosen to be five to ensure that myocardium motion in gated PET was fully observed.

Taking into account the findings of Park et al. (Park et al., 2008) our choice allowed a reliable assessment of the gating method differences and in the process also fulfilled the requirements of the gated PET image quality. If necessary, according to respiratory motion amplitude, the applied algorithm can be easily adapted to different respiratory gate numbers as was shown in the Study III where also nine equal width gates was applied. In Study III the used respiratory gating method enabled a good PET image quality, reliable segmentation of CMA, and the phase-matched CTAC for gated PET images. Dawood et al have published the equation for the relation between optimal respiratory gating number and maximal respiratory motion of the heart in PET imaging (Dawood et al., 2009). Their equation suggests the use of eight gates if the respiratory motion of heart is 12 mm on average. Eight gates would have been an overestimation in our Study III due to differences between the gating approaches. Our study group in Turku PET Centre also studied the optimal number of gates in dual gated cardiac PET and found out that five respiratory and four cardiac gates was optimal number of gates to detect the cardiac motion in PET (Klén et al., 2020). Furthermore, in Study III our gating approach excluded on the average of 2.6% of PET data during extreme inhale breathing volumes to ensure the similar image quality and same amount of motion between each gated PET images. Overall our linear model between spirometric lung volume and motion amplitude of myocardium can be used together with the Klén’s or Dawood’s equations (Dawood et al., 2009; Klén et al., 2020) to estimate the optimal number of respiratory gates in a cardiac PET study, especially if the differences in gating methods are taken into account.

6.2 Respiratory gating methods in cardiac PET/CT

Chest wall motion tracking systems, as RPM (Nehmeh et al., 2002) and stretching belts (Martinez-Möller et al., 2007), are widely used for respiratory gating in current thoracic region clinical PET imaging. Even if the amplitude based gating approach is more accurate than time based gating to follow the respiratory motion of the heart it’s more prone to errors for following the baseline changes of the respiratory motion in patient studies (Martinez-Möller et al., 2007). Thus our approach in Study III and IV was to evaluate what are the differences between the spirometric volume, thoracic impedance and RPM signal based respiratory gated cardiac PET images, especially when the comparable amplitude based gating was applied.

First of all the duration of the study protocols in cardiac PET/CT was not significantly extended when these additional respiratory gating methods was applied. Only about 5 minutes extension was measured when spirometry device was used an addition to normal study protocol with RPM gating only. This was mainly due to the time to ensure that the mask settles correctly and no air leakage is present. When additional impedance registering was also applied no extension in study protocol was detected. All methods, even the spirometric mask, were well tolerated by the clinical patients and no discomfort about the mask was reported. It is possible that spirometric mask could be less tolerated if patient has acute or chronic obstructive respiratory tract disease or a tendency for anxiety.

In our study all three analysed signals, spirometric volume, thoracic impedance and RPM, had very good pairwise cycle length correlation showing that also the 3-lead impedance measurement detects the end-inspiration and end-expiration timing reliably. However, the amplitude correlations between three signals were mostly moderate to good, and the best correlation values were measured between volume and RPM signals. Explanation for the worse amplitude correlation for 3-lead impedance measuring system is that it is known to be more vulnerable for the possible source of errors, as electrode polarization and skin impedance, than a 4-lead systems where the impedance signal is measured between two non-current supplying electrodes (Grimnes & Martinsen, 2006). In our study the changes of impedance signals followed mostly the normal breathing pattern but a few markedly elevated peak values at the end of the deep inspiration breaths was obtained (Figure 26), which were most likely due to error from skin-electrode surface tension. However, the data during these erroneously cycles were removed before image reconstruction by applying the gating window restriction in the DG-algorithm. Noteworthy is the fact that visually the quality of the ECG signal was not compromised due to the simultaneous impedance measurement, which makes this 3-lead thoracic impedance approach potentially suitable also for dual gating without additional ECG recording.

Koivumäki et al. have studied optimal 4-lead configuration of thoracic impedance measurement for simultaneous ECG and respiratory signal detection (Koivumäki et al., 2012; Koivumäki et al., 2011). They measured different breathing patterns and compared the optimal 4-lead impedance signal to lung volume signal. They found excellent correlation for respiratory cycle lengths between impedance and volume signals as our 3-lead method had slightly weaker but still very good respiratory cycle length correlation. They showed that the optimal 4-lead configuration had average correlation value 0.95 for normalized impedance and volume signal amplitudes that is clearly better than the corresponding correlation value 0.58 or 0.74 in our 3-lead measurement study. The difference is mostly explained by the methodological differences between 3- and 4-lead measurement systems. Some of the differences can also originate from the fact that measured signal time in our study was more than 10 times longer than Koivumäki et al and we had hospitalized CAD patients as their subjects were healthy young adults.

6.3 Gated cardiac PET image analysis

Our aim was not to evaluate how reconstruction parameters affects to detection or activity profiles of plaques, but we are aware that parameters such as voxel size, number of iterations and smoothing has an influence through the PVE. In all our PET studies the used reconstruction voxel size was very close to the assumed real or used artificial plaque size why the analysis of artificial and clinical human coronary plaques was based on the maximum voxel position and activity values.

When analysing small and hot ROI areas as our plaques the PVE needs to be taken into account. Soret et al. has presented comprehensive analysis of the PVE to SUV or ROI values when imaging small, less than 3 x FWHM, targets (Soret et al., 2007). They showed in simulation studies that RC over ROI for the spherical, 5 mm diameter target is less than 5% from true activity due to PVE if the FWHM of the scanner is more than 5 mm. In the dynamic heart phantom study (Study II) the plaque around 3 mm in diameter (volume around 10 to 15 µl), with administered activity of 6 kBq, we obtained 15.2 kBq/ml activity concentration value when plaque was imaged without motions in weak background activity (Table 3). This yields approximately RC factor 0.03 for the plaque. This observation is in good concordance with results of Soret et al. In our study spatial resolution of PET scanner was around 5 mm to 6 mm (Teräs et al., 2007) and the applied voxel size was $2.0 \times 2.0 \times 3.27$ mm^3, ie. applied SUVmax-volume over the plaque was around 13 µl.

Our NEMA phantom study demonstrated that the corrections in the header of PET RDF file are needed for proper quantification of PET image after the DG-procedure. We obtained that without proper correction dead time correction factor of dual-gated images decreases with increasing acquisition duration. However, this adjustment was constant regardless of the acquisition duration, which was expected since the dead-time correction is mainly dependent on the count rate. Also, the scatter-fraction correction factor was clearly erroneously computed in dual-gated images without RDF header adjustments. There was also a clear increase of the scatter fraction with increasing acquisition duration in static and corrected dual-gated images. An explanation for this is that the scatter-correction algorithm requires enough coincidence events (statistics) to have a good estimate of the scatter fraction within reconstruction with only two iterations. Thus, the algorithm cannot reach an accurate estimate of the scatter fraction in a very short acquisition time. However, since the values of corrected dual gates and static images are extremely similar, it can be concluded that the scatter correction is performing well enough in the dual-gating algorithm. It was also shown that the correction for random coincidences was properly done in each dual gate and even for the dual gates with low statistics. The linear regression of the SNR in static images correlated with the dual-gated images with a correlation factor of 0.99, which highlights that the evolution of the SNR in dual-gated images is almost equal to its evolution in static images. No adjustments were needed for decay correction factor.

6.4 Cardiac phantoms performance in gated PET imaging

The first rotating phantom together with axial displacement was reconstructed to evaluate the correct gating performance of the reconstructed DG-method with known motions. To evaluate the performance potential of the DG-method in vulnerable coronary plaque detection we needed to reconstruct a realistic cardiac phantom for that. Several cardiac phantoms were already implemented but those were with contraction motion only (De Bondt et al., 2003, 2005; Visser et al., 2004). Furthermore, in our knowledge no realistic cardiac phantom that had both contraction and respiratory mimicking motions was commercially or scientifically presented or available in the beginning of the study. Thus we reconstructed our own cardiac phantom based on the anatomical and physiological knowledge of the dimensions and motions of left ventricle, coronary vessel and plaque (Daou, 2008; Narula et al., 2008; Shechter et al., 2006; Strauss & Narula, 2007; Wang et al., 1995). In the reconstructed heart phantom relatively more motion of coronaries was caused by respiratory movement while the contraction motion of the phantom was 7 mm, and mainly radial, which is likely somewhat less than reported around 10 to 15 mm, and mainly axial, contraction motion of coronaries in coronary angiography or MR imaging (Shechter et al., 2006; Wang et al., 1999). Even with this limitation with the heart phantom the DG-method detected 51% of contraction and 70% of respiratory motion for relatively hot but realistic size coronary plaque.

6.5 Minipig study performance in coronary plaque PET imaging

Feasibility of the DG-method in vivo coronary plaque detection was performed in minipig study where the plaque positions in the proximal parts of the main coronaries, heart motions and overall attenuation conditions where even more realistic than in the phantom studies. However, there are certain limitations in our minipig study model. The relatively long, about 2 hours, study protocol may be too stressfull for some of the minipigs and thus three minipigs did not survived at the end of our study protocol. One possible explanation for one or two of these premature deaths of the minipigs may be ACS due to occlusion of the coronary artery, which was caused by the present of the catheter. Another limitation was that the minipigs were put on respirator and the breathing of the minipigs were controlled by an external ventilator, which lead to breathing patterns that differ from free breathing.

Thus this ventilator driven breathing led to the smaller movement of the diaphragm than usually which in turn displaced the heart less than was assumed. Thus correcting for the detected respiratory movement gave very little benefit over cardiac gating only. These studies, however, showed that a small tip mimicking a coronary plaque could be imaged with fairly small statistics. The activity concentration and plaque-to-background ratio at the time of acquisition for plaque detection was estimated to be 150 kBq/ml and around 50, respectively. Later on Delso et al has shown that coronary plaques having activity around 0.39 kBq are detectable in minipig model with high background activity (Delso et al., 2011).

6.6 Clinical cardiac PET/CT study performance

The study protocol for clinical cardiac PET/CT studies followed mostly the clinical practice. In Study II we used additional VHLLP diet (Williams 2008) to suppress myocardial 18F-FDG uptake that made possible the potential detection of vulnerable coronary plaque for one stabilized ACS patient. Otherwise without myocardial suppression the detection of vulnerable coronary plaque seems to be very unlikely with 18F-FDG due to insufficient TBR between myocardium and the plaque activity.

Miss-registration between PET and CT attenuation correction is known to cause significant errors in quantitative cardiac PET imaging (Martinez-Möller et al., 2007). In a clinical setting, respiratory-gated CT for attenuation is also likely to be beneficial (CineCTAC) (Nehmeh et al., 2004). That was why we in Study II and III performed additional phase-matched dynamic CT to get optimal AC and image quality to gated cardiac PET images. This choice also enabled reliable myocardium segmentation in gated PET images and thus accurate CMA motion detection in Study III. It is evident that radiation dose was increased due to additional CineCTAC. Radiation doses in CT studies can be reduced by optimizing the tube current, and for CineCTAC current could be reduced from 30 to 10 mA. However, due to extra 3-5 mSv radiation dose from dynamic CT static CTAC scan should be considered as main approach also in gated cardiac PET studies and miss-registration problem could be managed with motion correction.

6.7 Breath controlled cardiac MR study performance

In breath controlled cardiac MRI study our aim was to evaluate which of the two respiration linked methods where more precise to follow the motion of the cardiac vessels. In the MRI study the quality of the cardiac images during breath-holds was slightly declined due to accepted variations (4%–23% of signal amplitude) in sequential BH levels and the used non-uniform voxel size dimensions. In MR images spatial accuracy error of vessel position was at most 3- 4 mm due to multiple BH periods and an average of 3–4 mm due to voxel dimensions. However, both limitations are in range of magnitude of coronary vessel diameter (Dodge et al., 1992) and thus the limitations can assume to have no relevant effect to the motion detection accuracy of the vessels. The actual localization accuracy of the vessel structures between the two physicians was relatively good. The defined BH levels were a bit of more repeatable in spirometry than in pressure belt signals. Slight sloping down was detectable in pressure belt signals during a BH for some volunteers but no such effect was present in volume signals meaning that no airflow leakage was present (Figure 25). It has been reported that holding breath is easier to maintain longer after inspiration whereas diaphragm position is more consistent after expiration (Feinberg & Johnson, 1995). This possible diaphragm relaxation during BH can explain the slight decrease seen in the pressure belt signals during the BH periods of inspirium and mid-expirium. Tracking error up to 20% of breathing amplitude can also be present in spirometry and is caused by stochastic signal based line variations (Zhang et al., 2003). However, in both studies the quality of spirometric volume signals was very good and no remarkable baseline variation was detected which is most likely due to the repeated self-calibration of the used spirometry device.

6.8 Vulnerable coronary plaque PET imaging

The PVE is the main concern in subvoxel size plaque detection with current PET scanners and thus the tracer accumulation in the small plaque should be very specific to gain high enough TBR values for plaque detection. The in-vivo TBR value for plaques varies according to the used radioactive tracer, plaque composition and surrounding tissue structure. The feasibility of 18F-FDG PET imaging for the coronary inflammation has reviewed by Rogers (Rogers & Tawakol, 2011). In coronary plaque imaging using 18F-FDG the theoretical limits for TBR is related mainly to the macrophages and their activity. Macrophages have shown to have glycolytic activity 5 to 20-fold higher than background tissues, and can increase up to 50-fold when activated (Kaim et al., 2002; Yamada et al., 1995). In practice Rudd et al. has reported that inflammatory carotic plaque mean 18F-FDG accumulation is 8 times more than in plasma or normal arterial wall (J.H.F. Rudd et al., 2002). In two other studies, where vulnerable plaque specific tracers, as monocyte chemoattractant protein-1 (MCP-1) and monoclonal antibody (MDA2) against epitopes of low-density-lipoprotein (LDL), have been studied, have reported similar range from 6 to 20-fold accumulation difference between to plaques and normal arterial tissue (Ohtsuki et al., 2001; Tsimikas et al., 1999). In case of 18F-FDG the TBR values in PET imaging can be even further improve by following the VHFLCPP diet

(Williams & Kolodny, 2008) that is rich in free fatty acids prior to 18F-FDG imaging. This specific diet has shown to result in a significant reduction in 18F-FDG uptake by the myocardium, without reducing 18F-FDG uptake in other tissues (de Groot et al., 2005; Williams & Kolodny, 2008), which was applied and observed also in our study. Correlations between vascular 18F-FDG uptake and atherosclerotic risk factors (Joly et al., 2009; Rudd et al., 2009) or risk of atherothrombosis (Rominger et al., 2009) have been reported. Dweck et al have been reported that [18F]Sodium-fluoride (18F-NaF) tracer could be a promising tracer for the assessment of coronary artery plaque (Dweck et al., 2012). 18F-NaF is an established PET tracer that detects bone formation and remodelling (Even-Sapir et al., 2006). Dweck et al suggested in their preliminary study that 18F-NaF could be more suitable for vulnerable coronary plaque detection than 18F-FDG due to result of myocardial spill over into the coronary arteries in 18F-FDG images, which they were observed despite the common VHFLCPP dietary restrictions (Dweck et al., 2012). The study showed that accumulation of 18F-NaF has strong correlation with coronary vessel calcium score when scores were less than 1000. Significant correlation between 18F-NaF activity and cardiovascular event rates and Framingham risk scores were also reported suggesting that 18F-NaF uptake provides different information, relating to metabolically active calcific plaque and developing micro-calcification (Dweck et al., 2012). Thus if active inflammatory and/or calcified coronary plaques could be detected with PET anti-inflammatory and/or antiatherosclerotic therapies, such as p38-α-kinase inhibitors (Rogers & Tawakol, 2011), could be targeted to these risk patients and possible prevent these plaques to rupture.

Strauss & Narula have reported theoretic calculations for the lower limit of TBR values for the coronary plaque detection in PET (Strauss & Narula, 2007). They showed that the needed TBR value for detection is strongly related to the plaque size. Strauss et al have emphasized that the relation is inversely exponential when the plaque size is smaller than the resolution of the PET scanner. Their theoretical calculations suggest that TBR values around 50 to 100 are needed for the detection of ca. 3 mm size plaques without motion with current PET scanner resolution. Delso et al have made comprehensive in vivo and ex vivo study where they showed that the sub-voxel size coronary plaque detection is theoretically possible with current generation PET scanners (Delso et al., 2011). They showed that without any motion the sub-voxel size plaque is detectable if TBR value between the plaque and myocardium uptake is between 50 to 100, and if at the same the plaque uptake value is at least 250 Bq. When the plaque uptake falls under this threshold the TBR requirement increases exponentially. The plaque and TBR values that were applied in our minipig study were rather high, even if the motions are taken into account, when compared to the results of Delso et al.

Another main concern is the constant motion of the heart, and thus plaques, during the PET imaging (Slomka et al., 2016). Motion deteriorates the plaque activity over larger volumes than actual plaque size. Thus the actual TBR value for the plaque detection is needed to be even higher than 50 to 100 that was shown by Delso et al (Delso et al., 2011). Thus the motion correction is mandatory for sub-voxel size plaque detection in PET. External signal based methods for deriving respiratory and cardiac gating information have been widely studied and have shown possibilities to improve the plaque detection, as was case also in this study. Kesner et al have been published a review article that introduces an alternative list-mode data-driven motion control framework to improve PET image enhancement of small moving targets (Kesner et al., 2014). These methods utilize motion information derived directly from raw acquisition PET data. Most of the data-driven gating research has focused on respiratory and not on cardiac motion because the pumping motion can be robustly handled by ECG signal based gating. Data-driven motion control techniques have been a long time under development process, and those have been estimated to provide a fast, inexpensive, and potentially robust systems for motion handling in PET (Kesner et al., 2014). Buther et al have shown that list-mode data-driven segmented centre-of-mass method can provide similar respiratory and cardiac gating information of heart motion during the PET scan than with external ECG or respiratory signal based methods (Büther et al., 2009). Buther et al have also shown that detection of lung or liver tumour motion is feasible with the list-mode data-driven PET gating methods (Büther et al., 2010). In the review article, Kesner et al. outlines that the resulting implications of data-driven motion control could be improved SUV measurements, lesion detection, CAD applications and motion characterization (Kesner et al., 2014). Recently at least one commercial operator have implemented in their newest PET/CT vendor data-driven motion control strategy for the cardiac motion elimination. This software, called as CardioFreeze^{TM} Siemens Medical Solutions USA, Inc., has marketed to reduce cardiac PET image blur from both cardiac and respiratory motion using only the external ECG trigger information for gating.

When gating methods are applied for motion elimination also the additional motion correction algorithms are then needed to reserve the statistics (Blume et al., 2012; Dawood et al., 2013). These motion correction methods should be based on the information of contraction and respiratory motion amplitudes and patterns between different gating phases. Our study group in Turku PET Centre was involved in the study where anatomical information of CT were successfully used for motion correction of dual gated cardiac PET images. Motion of myocardium was reduced, CNR was increased and target size was reduced when the motion correction methods were applied (Klén R et al., 2016). Catana has reported a comprehensive analysis of motion correction options for PET imaging (Catana, 2015). Catana has outlined the differences between pre-reconstruction, during reconstruction and post-reconstruction techniques for motion compensation of dual gated PET data. Post-reconstruction PET data driven approaches as optical flow algorithms have been proposed for deriving the motion field from the dual gated PET images (Dawood et al., 2008). Lamare et al. have been studied different post-reconstruction schemes of combining cardiac gated PET data in order to identify the best strategy to reconstruct motion free PET images from dual gated PET acquisitions (Lamare et al., 2014). They find significant benefits from both affine or elastic model based motion compensation approaches in both respiratory only or dual gated cardiac PET imaging setups in terms of image SNR and contrast values. Feng et al have published motion correction study for 4D cardiac PET images applying realistic XCAT phantom Monte Carlo simulations, where they compared non-rigid dual respiratory and cardiac motion correction methods after, during, and before image reconstruction (Feng et al., 2016). Their results showed that all three motion correction methods for dual gated PET data provided substantial improvement in the quality of 4D cardiac gated PET images as compared with no motion correction. Their conclusion were that when the goal is to reduce scan time or patient radiation dose during or before reconstruction applied motion correction provides a good compromise between image quality and computational times. In this current study, unfortunately, we did not have similar motion compensation algorithms available that we would applied to our dual gated cardiac PET data to combine all the data together and thus improve the image quality in terms of higher SNR values. However, our spirometry based lung volume change approach is one potential option for the more accurate individual respiratory motion handling in cardiac PET imaging due to individually optimal choice for the number of respiratory gates. In case of vulnerable plaque imaging contraction motion compensation is more demanding challenge due to fact that motion patterns are very rapid and different part of coronary vessels move in different phase and magnitude than other part of the vessels (Wang et al., 1999).

6.9 Future challenges and opportunities in small target cardiac PET and PET/MR imaging

The main limiting factor with analogic PET scanner for small target lesion detection is the relatively low spatial resolution that is around 4 to 5 mm (Germano et al., 2016). To improve the quality of small target PET imaging new reconstruction and hardware configuration has been recently prosed and also included in clinical routine. State of art in total body PET scanner, which long axial FOV covers the entire patient's body, has recently reviewed by Vandenberghe et al. (Stefaan Vandenberghe et al., 2020). They concludes that total body PET will improve imaging sensitivity up to factors 10-40 times when compared to standard 20 cm axial

FOV PET scanner. Hui et al. has published preliminary results of total body PET and they have reported that the system can have excellent delineation of small structures and lesions in PET (Hui et al., 2020). They emphasize the potential of the total body PET where the sensitivity gain offers the ability to perform thoracic PET imaging during a single breath-hold without motion artefacts. This would improve evaluation of lung cancers and small cardiac structures in PET images. The principles and advances of the recent ToF PET imaging are comprehensively reviewed by Vandenberghe et al (S. Vandenberghe et al., 2016). Including ToF information in PET reconstruction has shown to reduce background noise and to improve lesion-detection performance with high statistical power already at small number of iterations in phantom studies (Kadrmas et al., 2009a; Kadrmas et al., 2009b). Noteworthy is that the scanners which has same size crystal detectors the ToF reconstruction does not improve the spatial resolution of PET image (Jakoby et al., 2011). However, in clinical oncological studies better definition of small lesions, especially lower liver and lung lesion contrasts (El Fakhri et al, 2011), and noise reduction has reported to be improved when ToF is included in PET reconstruction (Lois et al., 2010). Benefits of ToF improvements have also shown to be linearly related with body-mass-index value of the patient (Lois et al., 2010). Advances in physics and technology of ToF PET have been recently reviewed by Schaart. He outlines the improvements in the ToF detectors, which are based on fast, bright, inorganic scintillators, and silicon based photomultipliers, which have widely displaced big analogic PMTs (Schaart, 2021). Surti and Karp have published review article in this spring where they introduce the latest commercial PET/CT scanners and those novel technologies and performances, that can reach up to 50 ps coincidence timing resolution (Surti & Karp, 2021). In myocardial perfusion PET imaging it has been also shown that ToF imaging results in contrast improvement, emphasized apical thinning and increased uptake in the lateral wall for N-13 ammonia (Tomiyama et al., 2015).

Lassen et al. have published a review article where they discuss recent advances in cardiac and respiratory gating and provide an overview of the most promising recent developments in the field (Lassen, Kwiecinski, & Slomka, 2019). Recently Lassen et al. have published data-driven motion detection and compensation method for coronary 18F-NaF PET imaging (Lassen, Kwiecinski, Cadet, et al., 2019). They found out that risk of patient repositioning, ie. gross patient motion (GPM), during up to 30 min PET scan is considerable in coronary PET imaging. They reported that automated retrospective data-driven GPM compensation is feasible and should be considered for coronary PET imaging. Lassen et al. have also shown that joint corrections for cardiac, respiratory and GPM in combination with background blood pool corrections markedly improve test-retest reproducibility of coronary ^{18}F-NaF PET (Lassen, Kwiecinski, Dey, et al., 2019).

Resolution recovery method as 3D modeling of scanner-specific point spread function (PSF) is another new improvement that is included into PET reconstruction to predict the input signal during the reconstruction. The modeling of the response point spread function has reported to improve both spatial resolution and noise properties of PET image (Panin et al., 2006). Furthermore, Akamatsu et al have shown that a combination of PSF modeling and ToF can improve PET image quality in terms of SNR, and thus using either lower injected activity or shorter acquisition times allows to obtain good image quality (Akamatsu et al., 2012). Nowadays both ToF and resolution recovery (PSF) methods are implemented in the latest PET scanners by all major vendors and these options have possibility to improve small target cardiac imaging accuracy in near future.

Integration of MR and PET has potential to improve cardiac PET imaging, but it is technically demanding (Quick, 2014). For example standard PET detectors could not be placed in the isocenter of an MRI scanner because of their scintillation crystal blocks read out by photomultiplier tubes (PMT), which are highly susceptible to magnetic fields (Pichler et al., 2008). However, vendors have introduced solid state PET detectors featuring digital silicon photomultipliers or avalanche photodiodes, which allows simultaneous PET/MR imaging with the new hybrid PET/MRscanners. First generation of integrated PET/MR imaging devices uses avalanche photodiode PET detector, which have more limited temporal performance and spatial resolution compared with standard photomultiplier detectors. Second generation of integrated devices using higher- performance solid-state photomultipliers that provide higher sensitivity and temporal resolution and allow time-of-flight imaging are introduced by many vendors (Ratib & Nkoulou, 2014). It is shown that the recent optimization of the entire coincidence detection chain, including the use of digital SiPM, improves the ToF PET system's coincidence resolving time to the values of 200–400 ps (Schaart, 2021). Thus uncertainty of the exact annihilation location along the LOR (i.e. depth resolution) is from 3 cm to 6 cm in these state-of-the-art ToF PET systems.

It is expected that the development and application of advanced triggering, nonrigid motion correction, and AC methods will have a substantial impact on PET/MR cardiac imaging in general and more specific in myocardial tissue quantification (Fieseler et al., 2013; Quick, 2014). As opposed to PET/CT, MR data in PET/MR can be acquired simultaneously to PET data acquisition. This inherently leads to less deviation and gross motion between both imaging modalities when compared with PET/CT imaging (Brendle et al., 2013). The accuracy of MR based AC in cardiac PET has shown to be comparable with CT based AC (Vontobel et al., 2015). Catana has made comprehensive analysis of motion correction options in PET/MRI (Catana, 2015). For cardiac cine MR only imaging respiratory and contraction motion correction with real-time respiratory self-gating combined with ECG-gating has been shown to be feasible (Uribe et al., 2007). Even more advanced image based navigation techniques have shown to be possible to apply for non-linear respiratory motion correction in coronary MR angiography imaging, obviating the need for respiratory gating (Henningsson & Botnar, 2013). A joint cardiac and respiratory motion estimation for motion corrected cardiac PET-MR has recently shown to provide more accurate motion estimation than using either modality separately (Kolbitsch et al., 2018). Data-driven, projection-based respiratory motion compensation of cardiac PET data has recently shown to be feasible without external motion tracking devices for PET/CT and PET/MR imaging (Lassen et al., 2020). In simultaneous PET-MR cardiac imaging Petibon et al have shown that it is feasible to incorporate both tagged-MR derived non rigid myocardial wall motion and PSF correction directly into the PET system matrix to improve PET image quality (Petibon et al., 2013). However, while tagged-MRI is optimal for measuring myocardial motion, it might not be the most efficient technique to track movements of coronary arteries (Petibon et al., 2014). Because coronary vessels are typically enclosed within an adipose matrix, Petibon et al have proposed MR based coronary motion correction technique for improved 18F-FDG-PET coronary plaque imaging in simultaneous cardiac phantom PET-MR imaging (Petibon et al., 2014). In their study they estimated respiratory and contraction motion fields for coronary vessels and heart, obtained from non-rigid registration of dynamic fat-MRI volumes, and incorporated those fields within the motion corrected framework of statistical iterative PET reconstruction. Significant improvements in terms of plaque contrast recovery and detectability were achieved as compared to conventional reconstruction techniques such as gating and motion uncorrected reconstruction methods. Thus it is predicted that PET/MRI could help characterize atherosclerotic plaques and differentiate plaques with a high risk of rupture from stable plaques (Petibon et al., 2014; Ratib & Nkoulou, 2014).

7 Conclusions

In this study the specific dual gated cardiac PET-method was developed, programmed and implemented. Benefits of the quantitative DG PET-method was studied with phantoms, minipigs and CAD patients.

The cardiac phantom PET study showed that small, active and moving plaques can be distinguished from myocardium activity, and the PET gating methods improved the detection sensitivity and resolution of the plaques. The DG PET-method improved the quantitative detection of small artificial coronary plaques of minipigs, and focal 18F-FDG uptake lesion in the LAD vessel wall of the CAD patient when compared to standard gating PET methods. MRI and 18F-FDG cardiac PET studies showed that the spirometry based lung volume signal has good linear relation with motions of the cardiac vessels and the myocardium, correspondingly. Standard 3-lead ECG connections specified thoracic impedance signal is feasible for amplitude-based respiratory gated cardiac PET. The impedance signal based gating method detects the similar myocardium motion amplitude and motion pattern in respiratory gated cardiac PET than the lung volume signal based gating method.

In clinical cardiac PET, the optimal motion handling solution should improve diagnostic accuracy of the disease under the study, and at the same time include fast and built-in reconstruction algorithm. Considering the latest research findings, the PET-data-driven respiratory motion correction methods appear the most suitable approach, together with standard ECG gating, to improve detection and correction of cardiac motion in clinical cardiac PET. However, the effectiveness of these newly implemented commercial applications for cardiac motion correction in PET has yet to be determined.

The specific conclusions of the studies are:

- The results of this study shows that the self-developed dual gated cardiac PET-method can improve the detection of small cardiac structures, as inflammatory coronary plaques, when 18F-FDG and VHFLCPP-diet are applied.
- The results of this study have increased the determination and measurement of individual cardiac movement induced by respiration.

Acknowledgements

This study was carried out within the Finnish Center of Excellence in Molecular Imaging in Cardiovascular and Metabolic Research at the Turku PET Centre, Department of Clinical Physiology and Nuclear Medicine in Turku University Hospital and University of Turku, Turku, Finland during the years 2006-2021. I express my sincere gratitude to the retired Professor Jaakko Hartiala (head of the department of Clinical Physiology and Nuclear Medicine at the beginning of the study) and especially to Professor Juhani Knuuti, the Director of Turku PET Centre, for providing excellent research facilities and all support for executing this project.

I still remember when you, Jaakko, received me openly at our first meeting in spring 2006 and guided me to Juhani's research team. Then I was just the rookie in medicine and unaware of the future. You both encouraged me to throw myself into unknown area of cardiac research with your own essence and example. Jaakko, I'm gratitude for your patient interest for my progress in research and clinical career for more than decade.

I owe my gratitude to my supervisors Professor Juhani Knuuti and Professor Mika Teräs. Juhani, your visions, enthusiasm and courage to take cardiac research to the forefront towards new innovations are breathtaking. Your ambition has been a driving force in my research as well. I'm grateful to you that you believed in my ability to contribute to your cardiac research team's ambitious goal of detecting inflammatory coronary plaques with PET. I admire your leadership skills, extensive expert contacts, and implementation of the project scheduling. These skills of yours have made a significant contribution to the progress of my research as well. I am very grateful to you for always being financially supporting the progress on my research work, which freed up my time and resources to promote the actual research work itself during the period of my busy medical studies. Mika, your expertise as a hospital physicist and your practical knowledge in PET/CT imaging guided me through the deep learning process of the PET/CT imaging including essential phenomena of nuclear medicine and device technology. I'm gratitude for your professional contacts with the equipment supplier experts and other research groups. These contacts had significant benefit in overcoming the technical challenges during the validation process of the DG method. I thank you also for your patience and co-

work for helping me through challenges in publication processes and especially for finalizing this doctoral thesis manuscript. Thank you both for trusting me, and your patience with the delay in completing my doctoral thesis.

My best thanks also go to Prof. Pekka Hänninen for his guidance work in my PhD supervisory group. I want to acknowledge both Associate Professor Mikko Hakulinen and Associate Professor Antti Sohlberg for the professional and smooth pre-examination of this thesis. Thank you for your valuable time and effort you put to review of the thesis manuscript in the intended time schedule. Your comments and feedback were essential to improve the quality of the manuscript.

I would like to express my gratitude to my co-authors and collaborators. This doctoral dissertation would have been impossible to perform without your extensive and supportive expertise and ambitious attitude towards scientific work. My deepest gratitude to MSc Nicholas Durand-Schaefer for your validation work of the dual gating procedure with NEMA phantom study. I felt always friendly and helpful cooperation with you during the quantitative validation of the dual gating method. Your presence and effort made collaboration with consultants of the PET/CT scanner fluent and powerful. You had valuable connections with the technical specialists of the equipment supplier. I also thank you for the friendship that I was able to share with you and Raluca during your stay in Turku. Thank you very much radiochemist Hannu Sipilä, without your intelligence and knowledge of the technical equipments, this study would not have been possible. Your astonishing capability to reconstruct the phantoms using the available technical components was overwhelming. You got to work on the phantoms physical proportions and physiological phenomena that are known about heart function. Whatever change or improvement I asked for, you were able to implement it, and sometimes even better than I had planned. The most humble thanks to you for your help, contribution and very good cooperation in the development and implementation of the cardiac phantoms. Thank you also for your understanding and helpful attitude towards the busy schedule and precise requirements of our research project. You were truly our ”Gyro Gearloose”! I’m grateful to hospital physicist docent Tommi Noponen for your time and enthusiasm to support my research and sharing your knowledge of medical physics with me. Without your invaluable input, the publications of my doctoral dissertation would still not be complete. I’m grateful for you being always approachable and ready to address the research challenges that lie ahead. As a physicist you are always interested in a medical perspective also. For my understanding our collaboration has taken us both forward in our careers and I wish that our cooperation will continue as fruitful in the future as it has been so far. My sincerest thanks to Associate Professor Riku Klén for your invaluable knowledge and skills in mathematics, modelling and information technology relating to PET and CT imaging. Your input made possible to improve the dual gating algorithm and to perform offline analyzes of the research

data and results. Warm thanks to specialist Erika Hoppela for your work in CAD patients recruitment and acting as the person in charge of the CAD patients PET/CT imaging. Sincerest thanks to the docent and chief medical officer of Southwest Finland Hospital District Mikko Pietilä for your special expertise in coronary catheterization. Your catheterization skills allowed us to explore if PET imaging is capable to detect and visualize the artificial and hot coronary plaques from the coronaries of the minipigs. I still remember your warm attitude for me when I was a rookie in clinical cardiology and you kindly and calmly instructed me to focus clinically relevant issues related to the well-being of the hospitalized cardiac patient. I thank specialist Jan Kiss for your surgical expertise and skills that made possible the PET imaging of anesthetized minipigs. I thank my clinical colleague specialist Jussi Pärkkä and hospital physicist docent Virva Saunavaara for your knowledge and your assistance in performing and analyzing the cardiac MR study. I would like to thank Prof. Antti Saraste for your time and effort in inspecting and supervising my licentiate work that was related to this PhD study. I thank you both Prof. Antti Saraste and docent Sami Kajander for your valuable pioneering and research work in clinical PET and CT imaging of heart. Your work and role model has helped me to understand the clinical significance of CAD in nuclear medicine, radiology and cardiology.

I want to acknowledge all my fellow co-workers in Turku PET Centre, especially in ‘CarMet’ and ‘Plaque Project’ groups. My special thanks goes to PhD Jarkko Johansson. Your presence and practical tips, especially for Matlab programming, helped me over and over again trying to understand the secrets of instructional language and optimization of Matlab codes. Pondering and resolving things together was a thousand times more instructive than banging my head on the “wall of Matlab” alone. I’m gratitude to you Jarkko for your kindness and friendship both at work and in leisure time. I want to thank “IT-group” members Jouni, Rami, Marko, Vesa, Timo, Sauli and Harri for your support and time for the challenges I faced in programming and networking. My special thanks goes to the all of the Turku PET Centre radiographers, technologists and laboratory staff. I appreciate it you were there working extra hours after your busy clinical work day with our study group to perform our phantom, minipig and patient studies. It was not always straightforward with many technical apparatus but you were always patience and helpful to resolve the issues we faced. I sincerely try to remember all of you who were there for us, my warm thanks to: Minna, Tarja, Marjo, Hannele, Anne-Mari, Sanna, Heidi, Pauliina, Pirkko, Johanna, Eija and Tuula. To those whom I have forgotten, I also give my gratitude for your time and your skills that you put the studies of this PhD thesis.

During my clinical career, I have been supported by my colleagues who, by their example and support, have encouraged me to complete this PhD thesis alongside my daily work. I warmly thank especially you Prof. Jukka Kemppainen, clinical area

manager docent Maria Saarenhovi, and other specialist colleagues Jussi, Maija, Marko, Teemu, and Petri for your support to my research work.

During my research years, in addition to knowledge, I have made many new friends to my delight. In particular I wish to thank Jarkko, Gaber, Henkka, Nikke, Anu, Iina, Pauliina, Tiina, Kati, Jarmo, Jouni and Marco for their friendship and all the fun. I thank my fellow medical students Mikael, Kristian, Helena, Kaisa, Lauri, Johannes, Leif, Sanna, Jussi and Elina for your support and the common leisure fun that helped me cope with the research work alongside the medical studies. I want to thank also you Lassi, you got me out of my researcher's cave from time to time for both entertainment and the gym. I realize and admit now, those common entertainments were very necessary for me at that time.

On top of all, I want to express my sincere gratitude to my parents Raija and Reino and to my sister Susanna. You have always supported me all the way you were able to and encouraged me to keep going even then when there was no light in end of the tunnel. I value for your unselfish attitude to me and your way to express your love to me. By your example, you have taught me irrefutability, respect of others and that each is a blacksmith of his own happiness. Laura, my dear wife, without your presence and love, I honestly can say that this PhD thesis would not be completed now, and perhaps would never be completed. I thank you for your unconditional love and support that have kept me in sane and have given me the strength to finish this PhD thesis.

This work has been financially supported by the Finnish Foundation for Cardiovascular Research, State Research Funding ('EVO-financing'), Emil and Blida Maunula Funding, and the Turku University Foundation. This work is also partly supported by the Finnish Centre of Excellence in Molecular Imaging in Cardiovascular and Metabolic Research, supported by the Academy of Finland, the University of Turku, Turku University Hospital and Åbo Akademi University.

Turku, October 2021
Tommi Kokki

References

Agatston, A. S., Janowitz, W. R., Hildner, F. J., Zusmer, N. R., Viamonte, M., & Detrano, R. (1990). Quantification of coronary artery calcium using ultrafast computed tomography. *Journal of the American College of Cardiology*, *15*(4), 827–832. http://www.ncbi.nlm.nih.gov/pubmed/2407762

Akamatsu, G., Ishikawa, K., Mitsumoto, K., Taniguchi, T., Ohya, N., Baba, S., Abe, K., & Sasaki, M. (2012). Improvement in PET/CT image quality with a combination of point-spread function and time-of-flight in relation to reconstruction parameters. *Journal of Nuclear Medicine : Official Publication, Society of Nuclear Medicine*, *53*(11), 1716–1722. https://doi.org/10.2967/jnumed.112.103861

Alessio, A. M., Kinahan, P. E., & Lewellen, T. K. (2006). Modeling and incorporation of system response functions in 3-D whole body PET. *IEEE Transactions on Medical Imaging*, *25*(7), 828–837. http://www.ncbi.nlm.nih.gov/pubmed/16827484

Alexanderson, E., Slomka, P., Cheng, V., Meave, a, Saldana, Y., Garciarojas, L., & Berman, D. (2008). Fusion of positron emission tomography and coronary computed tomographic angiography identifies fluorine 18 fluorodeoxyglucose uptake in the left main coronary artery soft plaque. *Journal of Nuclear Cardiology*, *15*(6), 841–843. https://doi.org/10.1016/j.nuclcard.2008.06.014

Anderson, K. M., Odell, P. M., Wilson, P. W., & Kannel, W. B. (1991). Cardiovascular disease risk profiles. *American Heart Journal*, *121*(1 Pt 2), 293–298. http://www.ncbi.nlm.nih.gov/pubmed/1985385

Assmann, G., Cullen, P., & Schulte, H. (2002). Simple scoring scheme for calculating the risk of acute coronary events based on the 10-year follow-up of the prospective cardiovascular Münster (PROCAM) study. *Circulation*, *105*(3), 310–315. http://www.ncbi.nlm.nih.gov/pubmed/11804985

Bellina, C. R., Parodi, O., Camici, P., Salvadori, P. A., Taddei, L., Fusani, L., Guzzardi, R., Klassen, G. A., L'Abbate, A. L., & Donato, L. (1990). Simultaneous in vitro and in vivo validation of nitrogen-13-ammonia for the assessment of regional myocardial blood flow. *Journal of Nuclear Medicine : Official Publication, Society of Nuclear Medicine*, *31*(8), 1335–1343. http://www.ncbi.nlm.nih.gov/pubmed/2384801

Bengel, F M, Ziegler, S. I., Avril, N., Weber, W., Laubenbacher, C., & Schwaiger, M. (1997). Whole-body positron emission tomography in clinical oncology: comparison between attenuation-corrected and uncorrected images. *European Journal of Nuclear Medicine*, *24*(9), 1091–1098. http://www.ncbi.nlm.nih.gov/pubmed/9283100

Bengel, Frank M, Higuchi, T., Javadi, M. S., & Lautamäki, R. (2009). Cardiac positron emission tomography. *Journal of the American College of Cardiology*, *54*(1), 1–15. https://doi.org/10.1016/j.jacc.2009.02.065

Blume, M., Martinez-Möller, A., Keil, A., Navab, N., & Rafecas, M. (2010). Joint reconstruction of image and motion in gated positron emission tomography. *IEEE Transactions on Medical Imaging*, *29*(11), 1892–1906. https://doi.org/10.1109/TMI.2010.2053212

Blume, M., Navab, N., & Rafecas, M. (2012). Joint image and motion reconstruction for PET using a B-spline motion model. *Physics in Medicine and Biology*, *57*(24), 8249–8270. https://doi.org/10.1088/0031-9155/57/24/8249

Boellaard, R., Krak, N. C., Hoekstra, O. S., & Lammertsma, A. A. (2004). Effects of noise, image resolution, and ROI definition on the accuracy of standard uptake values: a simulation study.

Journal of Nuclear Medicine : Official Publication, Society of Nuclear Medicine, *45*(9), 1519–1527. http://www.ncbi.nlm.nih.gov/pubmed/15347719

Boucher, L., Rodrigue, S., Lecomte, R., & Bénard, F. (2004). Respiratory gating for 3-dimensional PET of the thorax: feasibility and initial results. *Journal of Nuclear Medicine : Official Publication, Society of Nuclear Medicine*, *45*(2), 214–219. http://www.ncbi.nlm.nih.gov/pubmed/14960638

Bowry, A. D. K., Lewey, J., Dugani, S. B., & Choudhry, N. K. (2015). The Burden of Cardiovascular Disease in Low- and Middle-Income Countries: Epidemiology and Management. *The Canadian Journal of Cardiology*, *31*(9), 1151–1159. https://doi.org/10.1016/j.cjca.2015.06.028

Brendle, C. B., Schmidt, H., Fleischer, S., Braeuning, U. H., Pfannenberg, C. A., & Schwenzer, N. F. (2013). Simultaneously Acquired MR/PET Images Compared with Sequential MR/PET and PET/CT: Alignment Quality. *Radiology*, *268*(1), 190–199. https://doi.org/10.1148/radiol.13121838

Brezinski, M. E., Tearney, G. J., Bouma, B. E., Izatt, J. A., Hee, M. R., Swanson, E. A., Southern, J. F., & Fujimoto, J. G. (1996). Optical coherence tomography for optical biopsy. Properties and demonstration of vascular pathology. *Circulation*, *93*(6), 1206–1213. http://www.ncbi.nlm.nih.gov/pubmed/8653843

Brown, C., Dempsey, M.-F., Gillen, G., & Elliott, A. T. (2010). Investigation of 18F-FDG 3D mode PET image quality versus acquisition time. *Nuclear Medicine Communications*, *31*(3), 254–259. https://doi.org/10.1097/MNM.0b013e3283355c5d

Budinger, T. F. (1983). Time-of-flight positron emission tomography: status relative to conventional PET. *Journal of Nuclear Medicine : Official Publication, Society of Nuclear Medicine*, *24*(1), 73–78. http://www.ncbi.nlm.nih.gov/pubmed/6336778

Büther, F., Dawood, M., Stegger, L., Wübbeling, F., Schäfers, M., Schober, O., & Schäfers, K. P. (2009). List mode-driven cardiac and respiratory gating in PET. *Journal of Nuclear Medicine : Official Publication, Society of Nuclear Medicine*, *50*(5), 674–681. https://doi.org/10.2967/jnumed.108.059204

Büther, F., Ernst, I., Dawood, M., Kraxner, P., Schäfers, M., Schober, O., & Schäfers, K. P. (2010). Detection of respiratory tumour motion using intrinsic list mode-driven gating in positron emission tomography. *European Journal of Nuclear Medicine and Molecular Imaging*, *37*(12), 2315–2327. https://doi.org/10.1007/s00259-010-1533-y

Catana, C. (2015). Motion correction options in PET/MRI. *Seminars in Nuclear Medicine*, *45*(3), 212–223. https://doi.org/10.1053/j.semnuclmed.2015.01.001

Cheruvu, P. K., Finn, A. V, Gardner, C., Caplan, J., Goldstein, J., Stone, G. W., Virmani, R., & Muller, J. E. (2007). Frequency and distribution of thin-cap fibroatheroma and ruptured plaques in human coronary arteries: a pathologic study. *Journal of the American College of Cardiology*, *50*(10), 940–949. https://doi.org/10.1016/j.jacc.2007.04.086

Cook, R. a H., Carnes, G., Lee, T.-Y., & Wells, R. G. (2007). Respiration-averaged CT for attenuation correction in canine cardiac PET/CT. *Journal of Nuclear Medicine : Official Publication, Society of Nuclear Medicine*, *48*(5), 811–818. https://doi.org/10.2967/jnumed.106.034199

Danias, P. G., Stuber, M., Botnar, R. M., Kissinger, K. V, Edelman, R. R., & Manning, W. J. (1999). Relationship between motion of coronary arteries and diaphragm during free breathing: lessons from real-time MR imaging. *AJR. American Journal of Roentgenology*, *172*(4), 1061–1065. https://doi.org/10.2214/ajr.172.4.10587147

Daou, D. (2008). Respiratory motion handling is mandatory to accomplish the high-resolution PET destiny. *European Journal of Nuclear Medicine and Molecular Imaging*, *35*(11), 1961–1970. https://doi.org/10.1007/s00259-008-0931-x

Dawood, M., Buther, F., Jiang, X., & Schafers, K. P. (2008). Respiratory motion correction in 3-D PET data with advanced optical flow algorithms. *IEEE Transactions on Medical Imaging*, *27*(8), 1164–1175. https://doi.org/10.1109/TMI.2008.918321

Dawood, M., Büther, F., Lang, N., Schober, O., & Schäfers, K. P. (2007). Respiratory gating in positron emission tomography: A quantitative comparison of different gating schemes. *Medical Physics*, *34*(7), 3067–3076. https://doi.org/10.1118/1.2748104

Dawood, M., Büther, F., Stegger, L., Jiang, X., Schober, O., Schäfers, M., & Schäfers, K. P. (2009). Optimal number of respiratory gates in positron emission tomography: A cardiac patient study. *Medical Physics*, *36*(5), 1775–1784. https://doi.org/10.1118/1.3112422

Dawood, M., Gigengack, F., Jiang, X., & Schafers, K. P. (2013). A mass conservation-based optical flow method for cardiac motion correction in 3D-PET. *Medical Physics*, *40*(1), 012505. https://doi.org/10.1118/1.4770276

Dawood, M., Lang, N., Jiang, X., & Schäfers, K. P. (2006). Lung motion correction on respiratory gated 3-D PET/CT images. *IEEE Transactions on Medical Imaging*, *25*(4), 476–485. https://doi.org/10.1109/TMI.2006.870892

De Bondt, P., Claessens, T., Rys, B., De Winter, O., Vandenberghe, S., Segers, P., Verdonck, P., & Dierckx, R. A. (2005). Accuracy of 4 different algorithms for the analysis of tomographic radionuclide ventriculography using a physical, dynamic 4-chamber cardiac phantom. *Journal of Nuclear Medicine : Official Publication, Society of Nuclear Medicine*, *46*(1), 165–171. http://www.ncbi.nlm.nih.gov/pubmed/15632048

De Bondt, P., Nichols, K., Vandenberghe, S., Segers, P., De Winter, O., Van de Wiele, C., Verdonck, P., Shazad, A., Shoyeb, A. H., & De Sutter, J. (2003). Validation of gated blood-pool SPECT cardiac measurements tested using a biventricular dynamic physical phantom. *Journal of Nuclear Medicine : Official Publication, Society of Nuclear Medicine*, *44*(6), 967–972. http://www.ncbi.nlm.nih.gov/pubmed/12791827

de Groot, M., Meeuwis, A. P. W., Kok, P. J. M., Corstens, F. H. M., & Oyen, W. J. G. (2005). Influence of blood glucose level, age and fasting period on non-pathological FDG uptake in heart and gut. *European Journal of Nuclear Medicine and Molecular Imaging*, *32*(1), 98–101. https://doi.org/10.1007/s00259-004-1670-2

Delso, G., Martinez-Möller, A., Bundschuh, R. A., Nekolla, S. G., Ziegler, S. I., & Schwaiger, M. (2011). Preliminary study of the detectability of coronary plaque with PET. *Physics in Medicine and Biology*, *56*(7), 2145–2160. https://doi.org/10.1088/0031-9155/56/7/016

Dodge, J. T., Brown, B. G., Bolson, E. L., & Dodge, H. T. (1992). Lumen diameter of normal human coronary arteries. Influence of age, sex, anatomic variation, and left ventricular hypertrophy or dilation. *Circulation*, *86*(1), 232–246. https://doi.org/10.1161/01.CIR.86.1.232

Dunphy, M. P. S., Freiman, A., Larson, S. M., & Strauss, H. W. (2005). *Association of Vascular 18 F-FDG Uptake with Vascular Calcification*. *46*(8), 1278–1284.

Durand-Schaefer, N. (2008). *Developement of a new imaging technique in positron emission tomography: the dual gating*. KTH Royal Institute of Technology.

Dweck, M. R., Chow, M. W. L., Joshi, N. V, Williams, M. C., Jones, C., Fletcher, A. M., Richardson, H., White, A., McKillop, G., van Beek, E. J. R., Boon, N. a, Rudd, J. H. F., & Newby, D. E. (2012). Coronary arterial 18F-sodium fluoride uptake: a novel marker of plaque biology. *Journal of the American College of Cardiology*, *59*(17), 1539–1548. https://doi.org/10.1016/j.jacc.2011.12.037

Ehara, S., Kobayashi, Y., Yoshiyama, M., Shimada, K., Shimada, Y., Fukuda, D., Nakamura, Y., Yamashita, H., Yamagishi, H., Takeuchi, K., Naruko, T., Haze, K., Becker, A. E., Yoshikawa, J., & Ueda, M. (2004). Spotty calcification typifies the culprit plaque in patients with acute myocardial infarction: an intravascular ultrasound study. *Circulation*, *110*(22), 3424–3429. https://doi.org/10.1161/01.CIR.0000148131.41425.E9

Ehman, R. L., McNamara, M. T., Pallack, M., Hricak, H., & Higgins, C. B. (1984). Magnetic resonance imaging with respiratory gating: techniques and advantages. *AJR. American Journal of Roentgenology*, *143*(6), 1175–1182. https://doi.org/10.2214/ajr.143.6.1175

El Fakhri, G., Surti, S., Trott, C. M., Scheuermann, J., & Karp, J. S. (2011). Improvement in lesion detection with whole-body oncologic time-of-flight PET. *Journal of Nuclear Medicine : Official Publication, Society of Nuclear Medicine*, *52*(3), 347–353. https://doi.org/10.2967/jnumed.110.080382

Erdi, Y. E., Nehmeh, S. A., Pan, T., Pevsner, A., Rosenzweig, K. E., Mageras, G., Yorke, E. D., Schoder, H., Hsiao, W., Squire, O. D., Vernon, P., Ashman, J. B., Mostafavi, H., Larson, S. M., & Humm, J. L. (2004). The CT motion quantitation of lung lesions and its impact on PET-measured

SUVs. *Journal of Nuclear Medicine : Official Publication, Society of Nuclear Medicine*, *45*(8), 1287–1292. http://www.ncbi.nlm.nih.gov/pubmed/15299050

Even-Sapir, E., Metser, U., Mishani, E., Lievshitz, G., Lerman, H., & Leibovitch, I. (2006). The detection of bone metastases in patients with high-risk prostate cancer: 99mTc-MDP Planar bone scintigraphy, single- and multi-field-of-view SPECT, 18F-fluoride PET, and 18F-fluoride PET/CT. *Journal of Nuclear Medicine : Official Publication, Society of Nuclear Medicine*, *47*(2), 287–297. http://www.ncbi.nlm.nih.gov/pubmed/16455635

Falk, E., Shah, P. K., & Fuster, V. (1995). Coronary plaque disruption. *Circulation*, *92*(3), 657–671. http://www.ncbi.nlm.nih.gov/pubmed/7634481

Feinberg, D. a, & Johnson, G. (1995). A methodology for co-registering abdominal MR images over multiple breath-holds. *Magnetic Resonance in Medicine : Official Journal of the Society of Magnetic Resonance in Medicine / Society of Magnetic Resonance in Medicine*, *34*(5), 770–774. http://www.ncbi.nlm.nih.gov/pubmed/8544699

Feng, T., Wang, J., Fung, G., & Tsui, B. (2016). Non-rigid dual respiratory and cardiac motion correction methods after, during, and before image reconstruction for 4D cardiac PET. *Physics in Medicine and Biology*, *61*(1), 151–168. https://doi.org/10.1088/0031-9155/61/1/151

Fieseler, M., Kugel, H., Gigengack, F., Kösters, T., Büther, F., Quick, H. H., Faber, C., Jiang, X., & Schäfers, K. P. (2013). A dynamic thorax phantom for the assessment of cardiac and respiratory motion correction in PET/MRI: A preliminary evaluation. *Nuclear Instruments and Methods in Physics Research Section A: Accelerators, Spectrometers, Detectors and Associated Equipment*, *702*, 59–63. https://doi.org/10.1016/j.nima.2012.09.039

Fin, L., Daouk, J., Morvan, J., Bailly, P., El Esper, I., Saidi, L., & Meyer, M.-E. (2008). Initial clinical results for breath-hold CT-based processing of respiratory-gated PET acquisitions. *European Journal of Nuclear Medicine and Molecular Imaging*, *35*(11), 1971–1980. https://doi.org/10.1007/s00259-008-0858-2

Fox, J. J., & Strauss, H. W. (2009). One step closer to imaging vulnerable plaque in the coronary arteries. *Journal of Nuclear Medicine : Official Publication, Society of Nuclear Medicine*, *50*(4), 497–500. https://doi.org/10.2967/jnumed.108.056325

Freiberg, J., Hove, J. D., Kofoed, K. F., Fritz-Hansen, T., Holm, S., Larsson, H. B., & Kelbaek, H. (2004). Absolute quantitation of left ventricular wall and cavity parameters using ECG-gated PET. *Journal of Nuclear Cardiology : Official Publication of the American Society of Nuclear Cardiology*, *11*(1), 38–46. https://doi.org/10.1016/j.nuclcard.2003.09.009

Frese, T., Rouze, N. C., Bouman, C. A., Sauer, K., & Hutchins, G. D. (2003). Quantitative comparison of FBP, EM, and Bayesian reconstruction algorithms for the IndyPET scanner. *IEEE Transactions on Medical Imaging*, *22*(2), 258–276. https://doi.org/10.1109/TMI.2002.808353

Fuster, V., Badimon, L., Badimon, J. J., & Chesebro, J. H. (1992a). The pathogenesis of coronary artery disease and the acute coronary syndromes (1). *The New England Journal of Medicine*, *326*(4), 242–250. https://doi.org/10.1056/NEJM199201233260406

Fuster, V., Badimon, L., Badimon, J. J., & Chesebro, J. H. (1992b). The pathogenesis of coronary artery disease and the acute coronary syndromes (2). *The New England Journal of Medicine*, *326*(5), 310–318. https://doi.org/10.1056/NEJM199201303260506

Germano, G., Berman, D. S., & Slomka, P. (2016). Technical Aspects of Cardiac PET Imaging and Recent Advances. *Cardiology Clinics*, *34*(1), 13–23. https://doi.org/10.1016/j.ccl.2015.07.015

Geworski, L., Knoop, B. O., de Cabrejas, M. L., Knapp, W. H., & Munz, D. L. (2000). Recovery correction for quantitation in emission tomography: a feasibility study. *European Journal of Nuclear Medicine*, *27*(2), 161–169. http://www.ncbi.nlm.nih.gov/pubmed/10755721

Goerres, G. W., Kamel, E., Heidelberg, T.-N. H., Schwitter, M. R., Burger, C., & von Schulthess, G. K. (2002). PET-CT image co-registration in the thorax: influence of respiration. *European Journal of Nuclear Medicine and Molecular Imaging*, *29*(3), 351–360. http://www.ncbi.nlm.nih.gov/pubmed/12002710

Gould, K. L., Pan, T., Loghin, C., Johnson, N. P., Guha, A., & Sdringola, S. (2007). Frequent diagnostic errors in cardiac PET/CT due to misregistration of CT attenuation and emission PET images: a definitive analysis of causes, consequences, and corrections. *Journal of Nuclear Medicine : Official Publication, Society of Nuclear Medicine*, *48*(7), 1112–1121. https://doi.org/10.2967/jnumed.107.039792

Gribbin, H. R. (1983). Using body surface movements to study breathing. *Journal of Medical Engineering & Technology*, *7*(5), 217–223. http://www.ncbi.nlm.nih.gov/pubmed/6226796

Grimnes, S., & Martinsen, Ø. G. (2006). Bioimpedance. In M. Akay (Ed.), *Biomedical Engineering*. John Wiley & Sons, Inc. https://doi.org/10.1002/9780471740360

Hamirani, Y. S., Larijani, V., Isma'eel, H., Pagali, S. R., Bach, P., Karlsberg, R. P., & Budoff, M. J. (2010). Association of plaque in the carotid and coronary arteries, using MDCT angiography. *Atherosclerosis*, *211*(1), 141–145. https://doi.org/10.1016/j.atherosclerosis.2010.01.020

Henningsson, M., & Botnar, R. (2013). Advanced Respiratory Motion Compensation for Coronary MR Angiography. *Sensors*, *13*(6), 6882–6899. https://doi.org/10.3390/s130606882

Hickeson, M., Yun, M., Matthies, A., Zhuang, H., Adam, L.-E., Lacorte, L., & Alavi, A. (2002). Use of a corrected standardized uptake value based on the lesion size on CT permits accurate characterization of lung nodules on FDG-PET. *European Journal of Nuclear Medicine and Molecular Imaging*, *29*(12), 1639–1647. https://doi.org/10.1007/s00259-002-0924-0

Hoffman, E. J., Huang, S. C., & Phelps, M. E. (1979). Quantitation in positron emission computed tomography: 1. Effect of object size. *Journal of Computer Assisted Tomography*, *3*(3), 299–308. http://www.ncbi.nlm.nih.gov/pubmed/438372

Hoffman, E. J., Phelps, M. E., Wisenberg, G., Schelbert, H. R., & Kuhl, D. E. (1979). Electrocardiographic gating in positron emission computed tomography. *Journal of Computer Assisted Tomography*, *3*(6), 733–739. http://www.ncbi.nlm.nih.gov/pubmed/315969

Hoffmann, U., Moselewski, F., Nieman, K., Jang, I.-K., Ferencik, M., Rahman, A. M., Cury, R. C., Abbara, S., Joneidi-Jafari, H., Achenbach, S., & Brady, T. J. (2006). Noninvasive assessment of plaque morphology and composition in culprit and stable lesions in acute coronary syndrome and stable lesions in stable angina by multidetector computed tomography. *Journal of the American College of Cardiology*, *47*(8), 1655–1662. https://doi.org/10.1016/j.jacc.2006.01.041

Houtveen, J. H., Groot, P. F. C., & de Geus, E. J. C. (2006). Validation of the thoracic impedance derived respiratory signal using multilevel analysis. *International Journal of Psychophysiology : Official Journal of the International Organization of Psychophysiology*, *59*(2), 97–106. https://doi.org/10.1016/j.ijpsycho.2005.02.003

Hove, J. D., Gambhir, S. S., Kofoed, K. F., Kelbaek, H., Schelbert, H. R., & Phelps, M. E. (1998). Dual spillover problem in the myocardial septum with nitrogen-13-ammonia flow quantitation. *Journal of Nuclear Medicine : Official Publication, Society of Nuclear Medicine*, *39*(4), 591–598. http://www.ncbi.nlm.nih.gov/pubmed/9544662

Hsu, B. (2013). PET tracers and techniques for measuring myocardial blood flow in patients with coronary artery disease. *Journal of Biomedical Research*, *27*(6), 452–459. https://doi.org/10.7555/JBR.27.20130136

Huang, H., Virmani, R., Younis, H., Burke, A. P., Kamm, R. D., & Lee, R. T. (2001). The impact of calcification on the biomechanical stability of atherosclerotic plaques. *Circulation*, *103*(8), 1051–1056. http://www.ncbi.nlm.nih.gov/pubmed/11222465

Hui, T., Yusen, G., Haojun, Y., Pergcheng, H., Yiqiu, Z., Wujian, M., & Hongcheng, S. (2020). Total-Body PET/CT: Current Applications and Future Perspectives. *AJR. American Journal of Roentgenology*, *215*(2), 325–337. https://doi.org/10.2214/AJR.19.22705

Hutchins, G. D., Caraher, J. M., & Raylman, R. R. (1992). A region of interest strategy for minimizing resolution distortions in quantitative myocardial PET studies. *Journal of Nuclear Medicine : Official Publication, Society of Nuclear Medicine*, *33*(6), 1243–1250. http://www.ncbi.nlm.nih.gov/pubmed/1597746

Ishida, M., Schuster, A., Takase, S., Morton, G., Chiribiri, A., Bigalke, B., Schaeffter, T., Sakuma, H., & Nagel, E. (2011). Impact of an abdominal belt on breathing patterns and scan efficiency in whole-heart coronary magnetic resonance angiography: comparison between the UK and Japan. *Journal of Cardiovascular Magnetic Resonance : Official Journal of the Society for Cardiovascular Magnetic Resonance*, *13*(1), 71. https://doi.org/10.1186/1532-429X-13-71

Jafari Tadi, M., Koivisto, T., Pänkäälä, M., & Paasio, A. (2014). Accelerometer-Based Method for Extracting Respiratory and Cardiac Gating Information for Dual Gating during Nuclear Medicine Imaging. *International Journal of Biomedical Imaging*, *2014*, 690124. https://doi.org/10.1155/2014/690124

Jakoby, B. W., Bercier, Y., Conti, M., Casey, M. E., Bendriem, B., & Townsend, D. W. (2011). Physical and clinical performance of the mCT time-of-flight PET/CT scanner. *Physics in Medicine and Biology*, *56*(8), 2375–2389. https://doi.org/10.1088/0031-9155/56/8/004

Jaskowiak, C. J., Bianco, J. A., Perlman, S. B., & Fine, J. P. (2005). Influence of reconstruction iterations on 18F-FDG PET/CT standardized uptake values. *Journal of Nuclear Medicine : Official Publication, Society of Nuclear Medicine*, *46*(3), 424–428. http://www.ncbi.nlm.nih.gov/pubmed/15750154

Joly, L., Djaballah, W., Koehl, G., Mandry, D., Dolivet, G., Marie, P.-Y., & Benetos, A. (2009). Aortic inflammation, as assessed by hybrid FDG-PET/CT imaging, is associated with enhanced aortic stiffness in addition to concurrent calcification. *European Journal of Nuclear Medicine and Molecular Imaging*, *36*(6), 979–985. https://doi.org/10.1007/s00259-008-1047-z

Kadrmas, D. J., Casey, M. E., Black, N. F., Hamill, J. J., Panin, V. Y., & Conti, M. (2009). Experimental comparison of lesion detectability for four fully-3D PET reconstruction schemes. *IEEE Transactions on Medical Imaging*, *28*(4), 523–534. https://doi.org/10.1109/TMI.2008.2006520

Kadrmas, D. J., Casey, M. E., Conti, M., Jakoby, B. W., Lois, C., & Townsend, D. W. (2009). Impact of time-of-flight on PET tumor detection. *Journal of Nuclear Medicine : Official Publication, Society of Nuclear Medicine*, *50*(8), 1315–1323. https://doi.org/10.2967/jnumed.109.063016

Kaim, A. H., Weber, B., Kurrer, M. O., Gottschalk, J., Von Schulthess, G. K., & Buck, A. (2002). Autoradiographic quantification of 18F-FDG uptake in experimental soft-tissue abscesses in rats. *Radiology*, *223*(2), 446–451. https://doi.org/10.1148/radiol.2232010914

Kajander, S., Joutsiniemi, E., Saraste, M., Pietilä, M., Ukkonen, H., Saraste, a, Sipilä, H. T., Teräs, M., Mäki, M., Airaksinen, J., Hartiala, J., & Knuuti, J. (2010). Cardiac positron emission tomography/computed tomography imaging accurately detects anatomically and functionally significant coronary artery disease. *Circulation*, *122*(6), 603–613. https://doi.org/10.1161/CIRCULATIONAHA.109.915009

Kalender, W. A., Rienmüller, R., Seissler, W., Behr, J., Welke, M., & Fichte, H. (1990). Measurement of pulmonary parenchymal attenuation: use of spirometric gating with quantitative CT. *Radiology*, *175*(1), 265–268. https://doi.org/10.1148/radiology.175.1.2315492

Kaufmann, P. A., & Camici, P. G. (2005). Myocardial blood flow measurement by PET: technical aspects and clinical applications. *Journal of Nuclear Medicine : Official Publication, Society of Nuclear Medicine*, *46*(1), 75–88. http://www.ncbi.nlm.nih.gov/pubmed/15632037

Kesner, A. L., Schleyer, P. J., Büther, F., Walter, M. A., Schäfers, K. P., & Koo, P. J. (2014). On transcending the impasse of respiratory motion correction applications in routine clinical imaging – a consideration of a fully automated data driven motion control framework. *EJNMMI Physics*, *1*(1), 8. https://doi.org/10.1186/2197-7364-1-8

Kessler, R. M., Ellis, J. R., & Eden, M. (1984). Analysis of emission tomographic scan data: limitations imposed by resolution and background. *Journal of Computer Assisted Tomography*, *8*(3), 514–522. http://www.ncbi.nlm.nih.gov/pubmed/6609942

Kety, S. S. (1951). The theory and applications of the exchange of inert gas at the lungs and tissues. *Pharmacological Reviews*, *3*(1), 1–41. http://www.ncbi.nlm.nih.gov/pubmed/14833874

Keyes, J. W. (1995). SUV: standard uptake or silly useless value? *Journal of Nuclear Medicine : Official Publication, Society of Nuclear Medicine*, *36*(10), 1836–1839. http://www.ncbi.nlm.nih.gov/pubmed/7562051

Khorsand, A., Graf, S., Frank, H., Kletter, K., Sochor, H., Maurer, G., Schuster, E., Globits, S., Dudczak, R., & Porenta, G. (2003). Model-based analysis of electrocardiography-gated cardiac (18)F-FDG PET images to assess left ventricular geometry and contractile function. *Journal of Nuclear Medicine : Official Publication, Society of Nuclear Medicine*, *44*(11), 1741–1746. http://www.ncbi.nlm.nih.gov/pubmed/14602854

Kinahan, P. E., & Fletcher, J. W. (2010). Positron emission tomography-computed tomography standardized uptake values in clinical practice and assessing response to therapy. *Seminars in Ultrasound, CT, and MR*, *31*(6), 496–505. https://doi.org/10.1053/j.sult.2010.10.001

Kinahan, P. E., Hasegawa, B. H., & Beyer, T. (2003). X-ray-based attenuation correction for positron emission tomography/computed tomography scanners. *Seminars in Nuclear Medicine*, *33*(3), 166–179. https://doi.org/10.1053/snuc.2003.127307

Klein, G. J., & Huesman, R. H. (2002). Four-dimensional processing of deformable cardiac PET data. *Medical Image Analysis*, *6*(1), 29–46. http://www.ncbi.nlm.nih.gov/pubmed/11836133

Klein, G., Reutter, B., Ho, M., Reed, J., & Huesman, R. (1998). Real-Time System for Respiratory-Cardiac Gating in Positron Tomography. *IEEE Transactions on Nuclear Science*, *45*(4), 2139–2143.

Klén, R., Teuho, J., Noponen, T., Thielemans, K., Hoppela, E., Lehtonen, E., Sipila, H. T., Teräs, M., & Knuuti, J. (2020). Estimation of optimal number of gates in dual gated 18F-FDG cardiac PET. *Scientific Reports*, *10*(1). https://doi.org/10.1038/s41598-020-75613-5

Klén R, Noponen T, Koikkalainen J, Lötjönen J, Thielemans K, Hoppela E, Sipilä HT, Teräs M, & Knuuti J. (2016). Evaluation of motion-correction methods for dual-gatedcardiac positron emission tomography/computed tomographyimaging. *Nucl Med Commun*, *Sep;37*(9), 956–968. https://doi.org/10.1097/MNM.0000000000000539.

Knight, S. B., Delbeke, D., Stewart, J. R., & Sandler, M. P. (1996). Evaluation of pulmonary lesions with FDG-PET. Comparison of findings in patients with and without a history of prior malignancy. *Chest*, *109*(4), 982–988. http://www.ncbi.nlm.nih.gov/pubmed/8635381

Koivumäki, T, Vauhkonen, M., Kuikka, J. T., & Hakulinen, M. a. (2012). Bioimpedance-based measurement method for simultaneous acquisition of respiratory and cardiac gating signals. *Physiological Measurement*, *33*(8), 1323–1334. https://doi.org/10.1088/0967-3334/33/8/1323

Koivumäki, Tuomas, Nekolla, S. G., Fürst, S., Loher, S., Vauhkonen, M., Schwaiger, M., & Hakulinen, M. A. (2014). An integrated bioimpedance--ECG gating technique for respiratory and cardiac motion compensation in cardiac PET. *Physics in Medicine and Biology*, *59*(21), 6373–6385. https://doi.org/10.1088/0031-9155/59/21/6373

Koivumäki, Tuomas, Teuho, J., Teräs, M., Vauhkonen, M., & Hakulinen, M. A. (2015). A novel respiratory gating method for oncologic positron emission tomography based on bioimpedance approach. *Annals of Nuclear Medicine*, *29*(4), 351–358. https://doi.org/10.1007/s12149-015-0953-y

Koivumäki, Tuomas, Vauhkonen, M., Kuikka, J. T., & Hakulinen, M. a. (2011). Optimizing bioimpedance measurement configuration for dual-gated nuclear medicine imaging: a sensitivity study. *Medical & Biological Engineering & Computing*, *49*(7), 783–791. https://doi.org/10.1007/s11517-011-0787-2

Kolbitsch, C., Radhouene, N., Fenchel, M., Schuh, A., Mallia, A., Marsden, P., & Schaeffter, T. (2018). Joint cardiac and respiratory motion estimation for motion-corrected cardiac PET-MR. *Physics in Medicine and Biology*, *64*(1). https://doi.org/10.1088/1361-6560/aaf246

Konno, K., & Mead, J. (1967). Measurement of the separate volume changes of rib cage and abdomen during breathing. *Journal of Applied Physiology*, *22*(3), 407–422.

Krak, N. C., Boellaard, R., Hoekstra, O. S., Twisk, J. W. R., Hoekstra, C. J., & Lammertsma, A. A. (2005). Effects of ROI definition and reconstruction method on quantitative outcome and applicability in a response monitoring trial. *European Journal of Nuclear Medicine and Molecular Imaging*, *32*(3), 294–301. https://doi.org/10.1007/s00259-004-1566-1

Lamare, F., Le Maitre, A., Dawood, M., Schäfers, K. P., Fernandez, P., Rimoldi, O. E., & Visvikis, D. (2014). Evaluation of respiratory and cardiac motion correction schemes in dual gated PET/CT cardiac imaging. *Medical Physics*, *41*(7), 072504. https://doi.org/10.1118/1.4881099

Lassen, M. L., Beyer, T., Berger, A., Beitzke, D., Rasul, S., Büther, F., Hacker, M., & Cal-Gonzales, J. (2020). Data-driven, projection-based respiratory motion compensation of PET data for cardiac PET/CT and PET/MR imaging. *Journal of Nuclear Cardiology*, *27*(6), 2216–2230. https://doi.org/10.1007/s12350-019-01613-2

Lassen, M. L., Kwiecinski, J., Cadet, S., Dey, D., Wang, C., Dweck, M. R., Bergman, D. S., Germano, G., Newby, D. E., & Slomka, P. J. (2019). Data-Driven Gross Patient Motion Detection and Compensation: Implications for Coronary 18F-NaF PET Imaging. *Journal of Nuclear Medicine*, *60*(6), 830–836. https://doi.org/https://doi.org/10.2967/jnumed.118.217877

Lassen, M. L., Kwiecinski, J., Dey, D., Cadet, S., Germano, G., Berman, D. S., Adamson, P. D., Moss, A. J., Dweck, M. R., Newby, D. E., & Slomka, P. J. (2019). Triple-gated motion and blood pool clearance corrections improve reproducibility of coronary 18F-NaF PET. *European Journal of Nuclear Medicine and Molecular Imaging*, *46*(12), 2610–2620. https://doi.org/10.1007/s00259-019-04437-x

Lassen, M. L., Kwiecinski, J., & Slomka, P. J. (2019). Gating Approaches in Cardiac PET Imaging. *PET Clinics*, *14*(2), 271–279. https://doi.org/10.1016/j.cpet.2018.12.008

Le Meunier, L., Maass-Moreno, R., Carrasquillo, J. A., Dieckmann, W., & Bacharach, S. L. (2006). PET/CT imaging: effect of respiratory motion on apparent myocardial uptake. *Journal of Nuclear Cardiology : Official Publication of the American Society of Nuclear Cardiology*, *13*(6), 821–830. https://doi.org/10.1016/j.nuclcard.2006.09.003

Li, X. A., Stepaniak, C., & Gore, E. (2006). Technical and dosimetric aspects of respiratory gating using a pressure-sensor motion monitoring system. *Medical Physics*, *33*(1), 145–154. http://www.ncbi.nlm.nih.gov/pubmed/16485421

Lim, S. P., Mc Ardle, B. A., Beanlands, R. S., & Hessian, R. C. (2014). Myocardial viability: it is still alive. *Seminars in Nuclear Medicine*, *44*(5), 358–374. https://doi.org/10.1053/j.semnuclmed.2014.07.003

Liu, C., Ii, L. A. P., Alessio, A. M., & Kinahan, P. E. (2009). The impact of respiratory motion on tumor quantification and delineation in static PET/CT imaging Chi. *Physics in Medicine and Biology*, *54*(24), 7345–7362. https://doi.org/10.1088/0031-9155/54/24/007.The

Liu, Y. L., Riederer, S. J., Rossman, P. J., Grimm, R. C., Debbins, J. P., & Ehman, R. L. (1993). A monitoring, feedback, and triggering system for reproducible breath-hold MR imaging. *Magnetic Resonance in Medicine*, *30*(4), 507–511. http://www.ncbi.nlm.nih.gov/pubmed/8255201

Livieratos, L, Stegger, L., Bloomfield, P. M., Schafers, K., Bailey, D. L., & Camici, P. G. (2005). Rigid-body transformation of list-mode projection data for respiratory motion correction in cardiac PET. *Physics in Medicine and Biology*, *50*(14), 3313–3322. https://doi.org/10.1088/0031-9155/50/14/008

Livieratos, Lefteris, Rajappan, K., Stegger, L., Schafers, K., Bailey, D. L., & Camici, P. G. (2006). Respiratory gating of cardiac PET data in list-mode acquisition. *European Journal of Nuclear Medicine and Molecular Imaging*, *33*(5), 584–588. https://doi.org/10.1007/s00259-005-0031-0

Lodge, M. A., Chaudhry, M. A., & Wahl, R. L. (2012). Noise considerations for PET quantification using maximum and peak standardized uptake value. *Journal of Nuclear Medicine : Official Publication, Society of Nuclear Medicine*, *53*(7), 1041–1047. https://doi.org/10.2967/jnumed.111.101733

Lois, C., Jakoby, B. W., Long, M. J., Hubner, K. F., Barker, D. W., Casey, M. E., Conti, M., Panin, V. Y., Kadrmas, D. J., & Townsend, D. W. (2010). An assessment of the impact of incorporating time-of-flight information into clinical PET/CT imaging. *Journal of Nuclear Medicine : Official Publication, Society of Nuclear Medicine*, *51*(2), 237–245. https://doi.org/10.2967/jnumed.109.068098

Lowe, V. J., Hoffman, J. M., DeLong, D. M., Patz, E. F., & Coleman, R. E. (1994). Semiquantitative and visual analysis of FDG-PET images in pulmonary abnormalities. *Journal of Nuclear Medicine : Official Publication, Society of Nuclear Medicine*, *35*(11), 1771–1776. http://www.ncbi.nlm.nih.gov/pubmed/7965154

Lucignani, G. (2009). Respiratory and cardiac motion correction with 4D PET imaging: shooting at moving targets. *European Journal of Nuclear Medicine and Molecular Imaging*, *36*(2), 315–319. https://doi.org/10.1007/s00259-008-1017-5

Martinez-Möller, A., Souvatzoglou, M., Navab, N., Schwaiger, M., & Nekolla, S. G. (2007). Artifacts from misaligned CT in cardiac perfusion PET/CT studies: frequency, effects, and potential solutions. *Journal of Nuclear Medicine : Official Publication, Society of Nuclear Medicine*, *48*(2), 188–193. http://www.ncbi.nlm.nih.gov/pubmed/17268013

Martinez-Möller, A., Zikic, D., Botnar, R. M., Bundschuh, R. a, Howe, W., Ziegler, S. I., Navab, N., Schwaiger, M., & Nekolla, S. G. (2007). Dual cardiac-respiratory gated PET: implementation and results from a feasibility study. *European Journal of Nuclear Medicine and Molecular Imaging*, *34*(9), 1447–1454. https://doi.org/10.1007/s00259-007-0374-9

Meirelles, G. S. P., Erdi, Y. E., Nehmeh, S. A., Squire, O. D., Larson, S. M., Humm, J. L., & Schöder, H. (2007). Deep-inspiration breath-hold PET/CT: clinical findings with a new technique for detection and characterization of thoracic lesions. *Journal of Nuclear Medicine : Official Publication, Society of Nuclear Medicine*, *48*(5), 712–719. https://doi.org/10.2967/jnumed.106.038034

Morel, D. R., Forster, A., Suter, P. M., & Suter, M. (1983). Noninvasive ventilatory monitoring with bellows pneumographs in supine subjects Noninvasive ventilatory monitoring pneumographs in supine subjects with bellows. *J Appl Physiol*, *55*, 598–606.

Motoyama, S., Kondo, T., Sarai, M., Sugiura, A., Harigaya, H., Sato, T., Inoue, K., Okumura, M., Ishii, J., Anno, H., Virmani, R., Ozaki, Y., Hishida, H., & Narula, J. (2007). Multislice computed tomographic characteristics of coronary lesions in acute coronary syndromes. *Journal of the American College of Cardiology*, *50*(4), 319–326. https://doi.org/10.1016/j.jacc.2007.03.044

Naghavi, M., Libby, P., Falk, E., Casscells, S. W., Litovsky, S., Rumberger, J., Badimon, J. J., Stefanadis, C., Moreno, P., Pasterkamp, G., Fayad, Z., Stone, P. H., Waxman, S., Raggi, P., Madjid, M., Zarrabi, A., Burke, A., Yuan, C., Fitzgerald, P. J., … Willerson, J. T. (2003a). From Vulnerable Plaque to Vulnerable Patient: a call for new definitions and risk assessment strategies: Part I. *Circulation*, *108*(14), 1664–1672. https://doi.org/10.1161/01.CIR.0000087480.94275.97

Naghavi, M., Libby, P., Falk, E., Casscells, S. W., Litovsky, S., Rumberger, J., Badimon, J. J., Stefanadis, C., Moreno, P., Pasterkamp, G., Fayad, Z., Stone, P. H., Waxman, S., Raggi, P., Madjid, M., Zarrabi, A., Burke, A., Yuan, C., Fitzgerald, P. J., … Willerson, J. T. (2003b). From vulnerable plaque to vulnerable patient: a call for new definitions and risk assessment strategies: Part II. *Circulation*, *108*(15), 1772–1778. https://doi.org/10.1161/01.CIR.0000087481.55887.C9

Narula, J., Garg, P., Achenbach, S., Motoyama, S., Virmani, R., & Strauss, H. W. (2008). Arithmetic of vulnerable plaques for noninvasive imaging. *Nature Clinical Practice. Cardiovascular Medicine*, *5 Suppl 2*(august), S2-10. https://doi.org/10.1038/ncpcardio1247

Nehmeh, S. A., Erdi, Y. E., Ling, C. C., Rosenzweig, K. E., Squire, O. D., Braban, L. E., Ford, E., Sidhu, K., Mageras, G. S., Larson, S. M., & Humm, J. L. (2002). Effect of respiratory gating on reducing lung motion artifacts in PET imaging of lung cancer. *Medical Physics*, *29*(3), 366. https://doi.org/10.1118/1.1448824

Nehmeh, S. A., Erdi, Y. E., Pan, T., Pevsner, A., Rosenzweig, K. E., Yorke, E., Mageras, G. S., Schoder, H., Vernon, P., Squire, O., Mostafavi, H., Larson, S. M., & Humm, J. L. (2004). Four-dimensional (4D) PET/CT imaging of the thorax. *Medical Physics*, *31*(12), 3179. https://doi.org/10.1118/1.1809778

Nehmeh, S. A., Erdi, Y. E., Pan, T., Yorke, E., Mageras, G. S., Rosenzweig, K. E., Schoder, H., Mostafavi, H., Squire, O., Pevsner, A., Larson, S. M., & Humm, J. L. (2004). Quantitation of respiratory motion during 4D-PET/CT acquisition. *Medical Physics*, *31*(6), 1333–1338. https://doi.org/10.1118/1.1739671

Nehmeh, Sadek A, & Erdi, Y. E. (2008). Respiratory motion in positron emission tomography/computed tomography: a review. *Seminars in Nuclear Medicine*, *38*(3), 167–176. https://doi.org/10.1053/j.semnuclmed.2008.01.002

Nehmeh, Sadek A, Erdi, Y. E., Ling, C. C., Rosenzweig, K. E., Schoder, H., Larson, S. M., Macapinlac, H. a, Squire, O. D., & Humm, J. L. (2002). Effect of respiratory gating on quantifying PET images of lung cancer. *Journal of Nuclear Medicine : Official Publication, Society of Nuclear Medicine*, *43*(7), 876–881. http://www.ncbi.nlm.nih.gov/pubmed/12097456

Nehmeh, Sadek A, Erdi, Y. E., Meirelles, G. S. P., Squire, O., Larson, S. M., Humm, J. L., & Schöder, H. (2007). Deep-inspiration breath-hold PET/CT of the thorax. *Journal of Nuclear Medicine : Official Publication, Society of Nuclear Medicine*, *48*(1), 22–26. http://www.ncbi.nlm.nih.gov/pubmed/17204695

Nørgaard, B. L., Leipsic, J., Gaur, S., Seneviratne, S., Ko, B. S., Ito, H., Jensen, J. M., Mauri, L., De Bruyne, B., Bezerra, H., Osawa, K., Marwan, M., Naber, C., Erglis, A., Park, S.-J., Christiansen, E. H., Kaltoft, A., Lassen, J. F., Bøtker, H. E., & Achenbach, S. (2014). Diagnostic performance of noninvasive fractional flow reserve derived from coronary computed tomography angiography in suspected coronary artery disease: the NXT trial (Analysis of Coronary Blood Flow Using CT Angiography: Next Steps). *Journal of the American College of Cardiology*, *63*(12), 1145–1155. https://doi.org/10.1016/j.jacc.2013.11.043

Nuyts, H., Maes, A., Vrolix, M., Schiepers, C., Schelbert, H., Kuhle, W., Bormans, G., Poppe, G., Buxton, D., Suetens, P., De Geest, H., & Mortelmans, L. (1996). Three-dimensional correction for spillover and recovery of myocardial PET images. *Journal of Nuclear Medicine : Official Publication, Society of Nuclear Medicine*, *37*(5), 767–774. http://www.ncbi.nlm.nih.gov/pubmed/8965143

Ohtsuki, K., Hayase, M., Akashi, K., Kopiwoda, S., Strauss, H. W., & Study, A. A. (2001). *Detection of Monocyte Chemoattractant Protein-1 Receptor*.

Pan, T., Lee, T.-Y., Rietzel, E., & Chen, G. T. Y. (2004). 4D-CT imaging of a volume influenced by respiratory motion on multi-slice CT. *Medical Physics*, *31*(2), 333. https://doi.org/10.1118/1.1639993

Pan, T., Mawlawi, O., Luo, D., Liu, H. H., Chi, P. M., Mar, M. V., Gladish, G., Truong, M., Erasmus, J., Liao, Z., & Macapinlac, H. a. (2006). Attenuation correction of PET cardiac data with low-dose average CT in PET/CT. *Medical Physics*, *33*(10), 3931. https://doi.org/10.1118/1.2349843

Panin, V. Y., Kehren, F., Michel, C., & Casey, M. (2006). Fully 3-D PET reconstruction with system matrix derived from point source measurements. *IEEE Transactions on Medical Imaging*, *25*(7), 907–921. http://www.ncbi.nlm.nih.gov/pubmed/16827491

Park, S.-J., Ionascu, D., Killoran, J., Mamede, M., Gerbaudo, V. H., Chin, L., & Berbeco, R. (2008). Evaluation of the combined effects of target size, respiratory motion and background activity on 3D and 4D PET/CT images. *Physics in Medicine and Biology*, *53*(13), 3661–3679. https://doi.org/10.1088/0031-9155/53/13/018

Petibon, Y., El Fakhri, G., Nezafat, R., Johnson, N., Brady, T., & Ouyang, J. (2014). Towards coronary plaque imaging using simultaneous PET-MR: a simulation study. *Physics in Medicine and Biology*, *59*(5), 1203–1222. https://doi.org/10.1088/0031-9155/59/5/1203

Petibon, Y., Ouyang, J., Zhu, X., Huang, C., Reese, T. G., Chun, S. Y., Li, Q., & El Fakhri, G. (2013). Cardiac motion compensation and resolution modeling in simultaneous PET-MR: a cardiac lesion detection study. *Physics in Medicine and Biology*, *58*(7), 2085–2102. https://doi.org/10.1088/0031-9155/58/7/2085

Phelps, M. E. (2006). *PET Physics, Instrumentation and Scanners* (M. E. Phelps (ed.)). Springer Science+Business Media, LLC.

Pichler, B. J., Wehrl, H. F., & Judenhofer, M. S. (2008). Latest advances in molecular imaging instrumentation. *Journal of Nuclear Medicine : Official Publication, Society of Nuclear Medicine*, *49 Suppl 2*, 5S-23S. https://doi.org/10.2967/jnumed.108.045880

Porenta, G., Kuhle, W., Sinha, S., Krivokapich, J., Czernin, J., Gambhir, S. S., Phelps, M. E., & Schelbert, H. R. (1995). Parameter estimation of cardiac geometry by ECG-gated PET imaging: validation using magnetic resonance imaging and echocardiography. *Journal of Nuclear Medicine : Official Publication, Society of Nuclear Medicine*, *36*(6), 1123–1129. http://www.ncbi.nlm.nih.gov/pubmed/7769438

Pruessmann, K. P., Weiger, M., Scheidegger, M. B., & Boesiger, P. (1999). SENSE: sensitivity encoding for fast MRI. *Magnetic Resonance in Medicine*, *42*(5), 952–962. http://www.ncbi.nlm.nih.gov/pubmed/10542355

Qayyum, A. A., & Kastrup, J. (2015). Measuring myocardial perfusion: the role of PET, MRI and CT. *Clinical Radiology*, *70*(6), 576–584. https://doi.org/10.1016/j.crad.2014.12.017

Quick, H. H. (2014). Integrated PET/MR. *Journal of Magnetic Resonance Imaging : JMRI*, *39*(2), 243–258. https://doi.org/10.1002/jmri.24523

Rajaram, M., Tahari, A. K., Lee, A. H., Lodge, M. A., Tsui, B., Nekolla, S., Wahl, R. L., Bengel, F. M., & Bravo, P. E. (2013). Cardiac PET/CT misregistration causes significant changes in estimated myocardial blood flow. *Journal of Nuclear Medicine : Official Publication, Society of Nuclear Medicine*, *54*(1), 50–54. https://doi.org/10.2967/jnumed.112.108183

Randle, P. J., Garland, P. B., Hales, C. N., & Newsholme, E. A. (1963). The glucose fatty-acid cycle. Its role in insulin sensitivity and the metabolic disturbances of diabetes mellitus. *Lancet (London, England)*, *1*(7285), 785–789. http://www.ncbi.nlm.nih.gov/pubmed/13990765

Ratib, O., & Nkoulou, R. (2014). Potential Applications of PET/MR Imaging in Cardiology. *Journal of Nuclear Medicine : Official Publication, Society of Nuclear Medicine*, *55*(Supplement 2), 40S-46S. https://doi.org/10.2967/jnumed.113.129262

Renker, M., Schoepf, U. J., Wang, R., Meinel, F. G., Rier, J. D., Bayer, R. R., Möllmann, H., Hamm, C. W., Steinberg, D. H., & Baumann, S. (2014). Comparison of diagnostic value of a novel noninvasive coronary computed tomography angiography method versus standard coronary angiography for assessing fractional flow reserve. *The American Journal of Cardiology*, *114*(9), 1303–1308. https://doi.org/10.1016/j.amjcard.2014.07.064

Richardson, P. D., Davies, M. J., & Born, G. V. (1989). Influence of plaque configuration and stress distribution on fissuring of coronary atherosclerotic plaques. *Lancet (London, England)*, *2*(8669), 941–944. http://www.ncbi.nlm.nih.gov/pubmed/2571862

Rioufol, G., Gilard, M., Finet, G., Ginon, I., Boschat, J., & André-Fouët, X. (2004). Evolution of spontaneous atherosclerotic plaque rupture with medical therapy: long-term follow-up with intravascular ultrasound. *Circulation*, *110*(18), 2875–2880. https://doi.org/10.1161/01.CIR.0000146337.05073.22

Rogers, I. S., & Tawakol, A. (2011). Imaging of coronary inflammation with FDG-PET: feasibility and clinical hurdles. *Current Cardiology Reports*, *13*(2), 138–144. https://doi.org/10.1007/s11886-011-0168-3

Rogers, I. S., Truong, Q. A., Joshi, S. B., & Hoffmann, U. (2010). Cardiac Computed Tomography. In V. Dilsizian & P. G. M. (Eds.), *Cardiac CT PET & MR* (2nd ed., pp. 73–74). Wiley-Blackwell.

Rogers, W. J., Shapiro, E. P., Weiss, J. L., Buchalter, M. B., Rademakers, F. E., Weisfeldt, M. L., & Zerhouni, E. A. (1991). Quantification of and correction for left ventricular systolic long-axis shortening by magnetic resonance tissue tagging and slice isolation. *Circulation*, *84*(2), 721–731. http://www.ncbi.nlm.nih.gov/pubmed/1860217

Rominger, A., Saam, T., Wolpers, S., Cyran, C. C., Schmidt, M., Foerster, S., Nikolaou, K., Reiser, M. F., Bartenstein, P., & Hacker, M. (2009). 18F-FDG PET/CT identifies patients at risk for future vascular events in an otherwise asymptomatic cohort with neoplastic disease. *Journal of Nuclear Medicine : Official Publication, Society of Nuclear Medicine*, *50*(10), 1611–1620. https://doi.org/10.2967/jnumed.109.065151

Rosenspire, K. C., Schwaiger, M., Mangner, T. J., Hutchins, G. D., Sutorik, A., & Kuhl, D. E. (1990). Metabolic fate of [13N]ammonia in human and canine blood. *Journal of Nuclear Medicine : Official Publication, Society of Nuclear Medicine*, *31*(2), 163–167. http://www.ncbi.nlm.nih.gov/pubmed/2313355

Rousset, O. G., Ma, Y., & Evans, A. C. (1998). Correction for partial volume effects in PET: principle and validation. *Journal of Nuclear Medicine : Official Publication, Society of Nuclear Medicine*, *39*(5), 904–911. http://www.ncbi.nlm.nih.gov/pubmed/9591599

Ruan, D., Fessler, J. A., Balter, J. M., & Sonke, J.-J. (2006). Exploring breathing pattern irregularity with projection-based method. *Medical Physics*, *33*(7), 2491–2499. http://www.ncbi.nlm.nih.gov/pubmed/16898452

Rudd, J.H.F., Warburton, E. A., Fryer, T. D., Jones, H. A., Clark, J. C., Antoun, N., Johnström, P., Davenport, A. P., Kirkpatrick, P. J., Arch, B. N., Pickard, J. D., & Weissberg, P. L. (2002). Imaging Atherosclerotic Plaque Inflammation With [18F]-Fluorodeoxyglucose Positron Emission Tomography. *Circulation*, *105*(23), 2708–2711. https://doi.org/10.1161/01.CIR.0000020548.60110.76

Rudd, James H F, Myers, K. S., Bansilal, S., Machac, J., Woodward, M., Fuster, V., Farkouh, M. E., & Fayad, Z. A. (2009). Relationships among regional arterial inflammation, calcification, risk factors, and biomarkers: a prospective fluorodeoxyglucose positron-emission tomography/computed tomography imaging study. *Circulation. Cardiovascular Imaging*, *2*(2), 107–115. https://doi.org/10.1161/CIRCIMAGING.108.811752

Santelli, C., Nezafat, R., Goddu, B., Manning, W. J., Smink, J., Kozerke, S., & Peters, D. C. (2011). Respiratory bellows revisited for motion compensation: preliminary experience for cardiovascular MR. *Magnetic Resonance in Medicine : Official Journal of the Society of Magnetic Resonance in Medicine / Society of Magnetic Resonance in Medicine*, *65*(4), 1097–1102. https://doi.org/10.1002/mrm.22687

Saranathan, M., Ho, V. B., Hood, M. N., Foo, T. K., & Hardy, C. J. (2001). Adaptive vessel tracking: automated computation of vessel trajectories for improved efficiency in 2D coronary MR angiography. *Journal of Magnetic Resonance Imaging : JMRI*, *14*(4), 368–373. http://www.ncbi.nlm.nih.gov/pubmed/11599060

Schaart, D. R. (2021). Physics and technology of time-of-flight PET detectors. *Physics in Medicine and Biology*, *66*(9). https://doi.org/10.1088/1361-6560/abee56

Schäfers, K P, Dawood, M., Lang, N., Büther, F., Schäfers, M., & Schober, O. (2005). Motion correction in PET/CT. *Nuklearmedizin*, *44*, S46-50. http://www.ncbi.nlm.nih.gov/pubmed/16395979

Schäfers, Klaus P, & Stegger, L. (2008). Combined imaging of molecular function and morphology with PET/CT and SPECT/CT: image fusion and motion correction. *Basic Research in Cardiology*, *103*(2), 191–199. https://doi.org/10.1007/s00395-008-0717-0

Schmitt, D., Karuta, B., Carrier, C., & Lecomte, R. (1988). Fast point spread function computation from aperture functions in high-resolution positron emission tomography. *IEEE Transactions on Medical Imaging*, *7*(1), 2–12. https://doi.org/10.1109/42.3923

Seppä, V.-P., Viik, J., & Hyttinen, J. (2010). Assessment of pulmonary flow using impedance pneumography. *IEEE Transactions on Bio-Medical Engineering*, *57*(9), 2277–2285. https://doi.org/10.1109/TBME.2010.2051668

Shechter, G., Resar, J. R., & McVeigh, E. R. (2006). Displacement and velocity of the coronary arteries: cardiac and respiratory motion. *IEEE Transactions on Medical Imaging*, *25*(3), 369–375. https://doi.org/10.1109/TMI.2005.862752

Sipila, H. T., Teras, M., Kokki, T., & Knuuti, J. (2007). A moving heart phantom for dual gated cardiac PET/CT studies. *2007 IEEE Nuclear Science Symposium Conference Record*, *5*. https://doi.org/10.1109/NSSMIC.2007.4436844

Slomka, P. J., Pan, T., & Germano, G. (2016). Imaging moving heart structures with PET. *Journal of Nuclear Cardiology*, *23*(3), 486–490. https://doi.org/10.1007/s12350-015-0094-7

Soret, M, Riddell, C., Hapdey, S., & Buvat, I. (2002). Biases affecting the measurements of tumor-to-background activity ratio in PET. *IEEE Transactions on Nuclear Science*, *49*(5), 2112–2118.

Soret, Marine, Bacharach, S. L., & Buvat, I. (2007). Partial-volume effect in PET tumor imaging. *Journal of Nuclear Medicine : Official Publication, Society of Nuclear Medicine*, *48*(6), 932–945. https://doi.org/10.2967/jnumed.106.035774

Strauss, H. W., & Narula, J. (2007). Atheroma roulette. *Journal of Nuclear Cardiology : Official Publication of the American Society of Nuclear Cardiology*, *14*(3), 293–297. https://doi.org/10.1016/j.nuclcard.2007.04.008

Surti, S., & Karp, J. S. (2021). Update on latest advances in time-of-flight PET. *Physica Medica*, *80*, 251–258. https://doi.org/10.1016/j.ejmp.2020.10.031

Tawakol, a, Migrino, R., Hoffmann, U., Abbara, S., Houser, S., Gewirtz, H., Muller, J., Brady, T., & Fischman, a. (2005). Noninvasive in vivo measurement of vascular inflammation with F-18 fluorodeoxyglucose positron emission tomography. *Journal of Nuclear Cardiology*, *12*(3), 294–301. https://doi.org/10.1016/j.nuclcard.2005.03.002

Tawakol, A., Migrino, R. Q., Bashian, G. G., Bedri, S., Vermylen, D., Cury, R. C., Yates, D., LaMuraglia, G. M., Furie, K., Houser, S., Gewirtz, H., Muller, J. E., Brady, T. J., & Fischman, A. J. (2006). In vivo 18F-fluorodeoxyglucose positron emission tomography imaging provides a noninvasive measure of carotid plaque inflammation in patients. *Journal of the American College of Cardiology*, *48*(9), 1818–1824. https://doi.org/10.1016/j.jacc.2006.05.076

Ter-Pogossian, M. M., Bergmann, S. R., & Sobel, B. E. (1982). Influence of cardiac and respiratory motion on tomographic reconstructions of the heart: implications for quantitative nuclear cardiology. *Journal of Computer Assisted Tomography*, *6*(6), 1148–1155. http://www.ncbi.nlm.nih.gov/pubmed/6983534

Teräs, M., Tolvanen, T., Johansson, J. J., Williams, J. J., & Knuuti, J. (2007). Performance of the new generation of whole-body PET/CT scanners: Discovery STE and Discovery VCT. *European Journal of Nuclear Medicine and Molecular Imaging*, *34*(10), 1683–1692. https://doi.org/10.1007/s00259-007-0493-3

Toia, P., La Grutta, L., & Sollami, G. (2020). Technical development in cardiac CT: current standards and future improvements—a narrative review. *Cardiovasc Diagn Ther.*, *10*(6), 2018–2035. https://doi.org/10.21037/cdt-20-527

Tomiyama, T., Ishihara, K., Suda, M., Kanaya, K., Sakurai, M., Takahashi, N., Takano, H., Nitta, K., Hakozaki, K., & Kumita, S. (2015). Impact of time-of-flight on qualitative and quantitative analyses of myocardial perfusion PET studies using (13)N-ammonia. *Journal of Nuclear Cardiology : Official Publication of the American Society of Nuclear Cardiology*, *22*(5), 998–1007. https://doi.org/10.1007/s12350-014-0037-8

Tsimikas, S., Palinski, W., Halpern, S. E., Yeung, D. W., Curtiss, L. K., & Witztum, J. L. (1999). Radiolabeled MDA2, an oxidation-specific, monoclonal antibody, identifies native atherosclerotic lesions in vivo. *Journal of Nuclear Cardiology : Official Publication of the American Society of Nuclear Cardiology*, *6*(1 Pt 1), 41–53. http://www.ncbi.nlm.nih.gov/pubmed/10070840

Uribe, S., Muthurangu, V., Boubertakh, R., Schaeffter, T., Razavi, R., Hill, D. L. G., & Hansen, M. S. (2007). Whole-heart cine MRI using real-time respiratory self-gating. *Magnetic Resonance in Medicine*, *57*(3), 606–613. https://doi.org/10.1002/mrm.21156

Vallabhajosula, S., & Fuster, V. (1997). Atherosclerosis: imaging techniques and the evolving role of nuclear medicine. *Journal of Nuclear Medicine : Official Publication, Society of Nuclear Medicine*, *38*(11), 1788–1796. http://www.ncbi.nlm.nih.gov/pubmed/9374357

Vandenberghe, S., Mikhaylova, E., D'Hoe, E., Mollet, P., & Karp, J. S. (2016). Recent developments in time-of-flight PET. *European Journal of Nuclear Medicine and Molecular Imaging*, *3*(1). https://doi.org/10.1186/s40658-016-0138-3

Vandenberghe, Stefaan, Moskal, P., & Karp, J. S. (2020). State of the art in total body PET. *EJNMMI Physics*, *7*(35). https://doi.org/10.1186/s40658-020-00290-2

Vedam, S. S., Kini, V. R., Keall, P. J., Ramakrishnan, V., Mostafavi, H., & Mohan, R. (2003). Quantifying the predictability of diaphragm motion during respiration with a noninvasive external marker. *Medical Physics*, *30*(4), 505–513. http://www.ncbi.nlm.nih.gov/pubmed/12722802

Virmani, R., Burke, A. P., Farb, A., & Kolodgie, F. D. (2006). Pathology of the vulnerable plaque. *Journal of the American College of Cardiology*, *47*(8 Suppl), C13-8. https://doi.org/10.1016/j.jacc.2005.10.065

Visser, J. J. N., Sokole, E. B., Verberne, H. J., Habraken, J. B. A., van de Stadt, H. J. F., Jaspers, J. E. N., Shehata, M., Heeman, P. M., & van Eck-Smit, B. L. F. (2004). A realistic 3-D gated cardiac phantom for quality control of gated myocardial perfusion SPET: the Amsterdam gated (AGATE) cardiac phantom. *European Journal of Nuclear Medicine and Molecular Imaging*, *31*(2), 222–228. https://doi.org/10.1007/s00259-003-1352-5

Visvikis, D., Costa, D. C., Croasdale, I., Lonn, A. H. R., Bomanji, J., Gacinovic, S., & Ell, P. J. (2003). CT-based attenuation correction in the calculation of semi-quantitative indices of [18F]FDG uptake in PET. *European Journal of Nuclear Medicine and Molecular Imaging*, *30*(3), 344–353. https://doi.org/10.1007/s00259-002-1070-4

Vontobel, J., Liga, R., Possner, M., Clerc, O. F., Mikulicic, F., Veit-Haibach, P., Ter Voert, E. E. G. W., Fuchs, T. A., Stehli, J., Pazhenkottil, A. P., Benz, D. C., Gräni, C., Gaemperli, O., Herzog, B., Buechel, R. R., & Kaufmann, P. A. (2015). MR-based attenuation correction for cardiac FDG PET on a hybrid PET/MRI scanner: comparison with standard CT attenuation correction. *European Journal of Nuclear Medicine and Molecular Imaging*, *42*(10), 1574–1580. https://doi.org/10.1007/s00259-015-3089-3

Wadhwani, R., & Longini, R. L. (1973). Analysis of quiet spontaneous breathing as measured by spirometer and electrical impedance plethysmography. *Computers and Biomedical Research, an International Journal*, *6*(1), 74–89. http://www.ncbi.nlm.nih.gov/pubmed/4695392

Wang, J. C., Normand, S.-L. T., Mauri, L., & Kuntz, R. E. (2004). Coronary artery spatial distribution of acute myocardial infarction occlusions. *Circulation*, *110*(3), 278–284. https://doi.org/10.1161/01.CIR.0000135468.67850.F4

Wang, T., Palucci, D., Law, K., Yanagawa, B., Yam, J., & Butany, J. (2012). Atherosclerosis: pathogenesis and pathology. *Diagnostic Histopathology*, *18*(11), 461–467. https://doi.org/10.1016/j.mpdhp.2012.09.004

Wang, Y, Riederer, S. J., & Ehman, R. L. (1995). Respiratory motion of the heart: kinematics and the implications for the spatial resolution in coronary imaging. *Magnetic Resonance in Medicine : Official Journal of the Society of Magnetic Resonance in Medicine / Society of Magnetic Resonance in Medicine*, *33*(5), 713–719. http://www.ncbi.nlm.nih.gov/pubmed/7596276

Wang, Yi, Vidan, E., & Bergman, G. W. (1999). Cardiac Imaging Cardiac Motion of Coronary Arteries : Variability in the Rest. *Radiology*, *213*(28), 751–758.

Wick, C. a, Su, J.-J., McClellan, J. H., Brand, O., Bhatti, P. T., Buice, A. L., Stillman, A. E., Tang, X., & Tridandapani, S. (2012). A system for seismocardiography-based identification of quiescent heart phases: implications for cardiac imaging. *IEEE Transactions on Information Technology in Biomedicine : A Publication of the IEEE Engineering in Medicine and Biology Society*, *16*(5), 869–877. https://doi.org/10.1109/TITB.2012.2198071

Wijns, W., Kolh, P., Danchin, N., Di Mario, C., Falk, V., Folliguet, T., Garg, S., Huber, K., James, S., Knuuti, J., Lopez-Sendon, J., Marco, J., Menicanti, L., Ostojic, M., Piepoli, M. F., Pirlet, C., Pomar, J. L., Reifart, N., Ribichini, F. L., … Taggart, D. (2010). Guidelines on myocardial revascularization. *European Heart Journal*, *31*(20), 2501–2555. https://doi.org/10.1093/eurheartj/ehq277

Williams, G., & Kolodny, G. M. (2008). Suppression of myocardial 18F-FDG uptake by preparing patients with a high-fat, low-carbohydrate diet. *AJR. American Journal of Roentgenology*, *190*(2), W151-6. https://doi.org/10.2214/AJR.07.2409

Wollenweber, T., & Bengel, F. M. (2014). Cardiac molecular imaging. *Seminars in Nuclear Medicine*, *44*(5), 386–397. https://doi.org/10.1053/j.semnuclmed.2014.05.002

Wykrzykowska, J., Lehman, S., Williams, G., Parker, J. A., Palmer, M. R., Varkey, S., Kolodny, G., & Laham, R. (2009). Imaging of inflamed and vulnerable plaque in coronary arteries with 18F-FDG PET/CT in patients with suppression of myocardial uptake using a low-carbohydrate, high-fat preparation. *Journal of Nuclear Medicine : Official Publication, Society of Nuclear Medicine*, *50*(4), 563–568. https://doi.org/10.2967/jnumed.108.055616

Yamada, S., Kubota, K., Kubota, R., Ido, T., & Tamahashi, N. (1995). High accumulation of fluorine-18-fluorodeoxyglucose in turpentine-induced inflammatory tissue. *Journal of Nuclear Medicine : Official Publication, Society of Nuclear Medicine*, *36*(7), 1301–1306. http://www.ncbi.nlm.nih.gov/pubmed/7790960

Yang, Y., Rendig, S., Siegel, S., Newport, D. F., & Cherry, S. R. (2005). Cardiac PET imaging in mice with simultaneous cardiac and respiratory gating. *Physics in Medicine and Biology*, *50*(13), 2979–2989. https://doi.org/10.1088/0031-9155/50/13/001

Zhang, T., Keller, H., O'Brien, M. J., Mackie, T. R., & Paliwal, B. (2003). Application of the spirometer in respiratory gated radiotherapy. *Medical Physics*, *30*(12), 3165–3171. https://doi.org/10.1118/1.1625439

Zubal, I. G., Bizais, Y., Bennett, G. W., & Brill, A. B. (1984). Dual gated nuclear cardiac images. *IEEE Transactions on Nuclear Science*, *31*(1), 566–569.

Zubal, I. G., Harrell, C. R., Smith, E. O., Rattner, Z., Gindi, G., & Hoffer, P. B. (1994). Computerized three-dimensional segmented human anatomy. *Medical Physics*, *21*(2), 299–302. http://www.ncbi.nlm.nih.gov/pubmed/8177164

Cardiovascular diseases (CVD) are still the most common cause of death in Finland. A rupture of a coronary artery plaque can lead to sudden death in an asymptomatic young person. Early individual identification in individuals at increased risk of vulnerable coronary plaque rupture could reduce premature mortality. At one time it could diminish unneccessary human suffering and improve Finnish society's ability to function by decreasing the number of work years lost prematurely. The aim of this dissertation was to investigate whether it is possible to detect these vulnerable coronary plaques applying a dual gated cardiac motion correction approach to a positron emission tomography (PET) imaging of heart. This dissertation showed that the dual gated cardiac PET method improves detection of small cardiac structures, such as coronary vessel wall pathology. Further studies of the role of PET imaging are needed for early detection of an asymptomatic CVD patient at risk of the plaque rupture.

TURUN
YLIOPISTO
UNIVERSITY
OF TURKU

Painosalama, Turku, Finland 2021

ISBN 978-951-29-8628-6 (PRINT)
ISBN 978-951-29-8629-3 (PDF)
ISSN 0355-9483 (Print)
ISSN 2343-3213 (Online)